Quantum communication using phonons

Towards a quantum network using high frequency mechanical oscillators

Fiaschi, N.

DOI
10.4233/uuid:db47aff4-192e-4557-ada9-22e8b7e5be07

Publication date
2023

Document Version
Final published version

Citation (APA)
Fiaschi, N. (2023). *Quantum communication using phonons: Towards a quantum network using high frequency mechanical oscillators*. [Dissertation (TU Delft), Delft University of Technology]. https://doi.org/10.4233/uuid:db47aff4-192e-4557-ada9-22e8b7e5be07

QUANTUM COMMUNICATION USING PHONONS

TOWARDS A QUANTUM NETWORK USING HIGH FREQUENCY MECHANICAL OSCILLATORS

QUANTUM COMMUNICATION USING PHONONS

TOWARDS A QUANTUM NETWORK USING HIGH FREQUENCY MECHANICAL OSCILLATORS

Dissertation

for the purpose of obtaining the degree of doctor
at Delft University of Technology,
by the authority of the Rector Magnificus Prof. dr. ir. T.H.J.J. van der Hagen,
chair of the Board for Doctorates,
to be defended publicly on
05/10/2023

by

Niccolò FIASCHI

Master of Science in Physics,
University of Florence, Italy,
born in Florence, Italy.

This dissertation has been approved by the promotors.

Composition of the doctoral committee:

Rector Magnificus,	voorzitter
Prof. dr. S. Gröblacher,	Technische Universiteit Delft, promotor
Prof. dr. E. Verhagen,	TU Eindhoven / AMOLF, copromotor
Independent members:	
Prof. dr. Y. Chu,	ETH Zurich
Prof. dr. A. Fiore,	TU Eindhoven
Prof. dr. M. Gurioli,	University of Florence
Prof. dr. U. Staufer,	Technische Universiteit Delft
Prof. dr. S. Otte,	Technische Universiteit Delft, reserve member

Printed by: *****

Front & Back: Artistic depiction of quantum connections using phonons, conceived by Niccolò Fiaschi and the AI Dall·E.

Casimir PhD Series, Delft-Leiden 2023-09

ISBN 000-00-0000-000-0

An electronic version of this dissertation is available at
http://repository.tudelft.nl/.

CONTENTS

SUMMARY

Quantum communication refers to the field of science that studies the ability to connect separated quantum devices via coherent channels, i.e. via buses that maintain coherently the information encoded. The importance of the task is on multiple levels: from secure communications to scaling quantum computers. The first one can be of fundamental importance in moments like government elections, or banks transaction, but even to secure the right of privacy of individuals. The latter could open the way to, for example, faster and more precise solutions to problems in chemistry (for drug development), or material science (more environmentally friendly solar cells). At this moment, quantum communication and computing are in a similar stage as of the early computers: the machines are with very little connectivity and require large spaces and specialists to be operated. In a few years, we can expect these systems to be interconnected more and more, scaled, and made easier to use. In this thesis, we present work done to create quantum channels using high frequency mechanical oscillators.

In chapter 1 we present recent progress in the field of quantum communication done with several types of systems, both in the long and short distance. We also introduce how high frequency mechanical oscillators could play an important role in this research area. We discuss the current challenges and limitations and possible future developments.

In chapter 2 we perform a optomechanical quantum teleportation. In this work, we teleport a polarization encoded telecom photon onto a quantum memory, made by two single mode mechanical oscillators in a dual-rail configuration. This work is a step towards entanglement swapping (also referred to as ’teleportation of entangled state’) and represents a proof of principle towards quantum repeaters (using the scheme proposed by Duan, Lukin, Cirac, and Zoller - DLCZ scheme).

In chapter 3 we report the first experiment done with the multimode mechanical devices. These devices are formed by a single mode optomechanical cavity coupled to a single-mode mechanical waveguide (ended with a phononic mirror). We show that the non-classical information created in the optomechanical cavity can be guided on-chip in the mechanical waveguide, using as witness the cross-correlation between the scattered photons. However, the non-uniform spacing between the mechanical modes severely lowers the maximum value of the non-classical correlation measured. This was greatly improved with the new design of the device. With this design, we are able to entangle two traveling phonons in the mechanical waveguide, shown in chapter 4. In this way, we show that the traveling phonons can be used to distribute quantum entanglement on-chip, a first step towards connecting quantum devices on a short scale.

In chapter 5, we measure in time the frequency jitter of two spectrally close mechanical modes of the same device. We demonstrate that the frequency diffusion of the modes is not correlated in time, and so the coherence length of the traveling information will ultimately be limited by the jitter. This result shows the importance of performing a detailed study on the surface defects.

Lastly, in chapter 6 we summarize the findings of these experiments and we discuss the future developments of the field.

SAMENVATTING

Kwantumcommunicatie verwijst naar het wetenschapsgebied dat het vermogen bestudeert om gescheiden kwantumapparaten met elkaar te verbinden via coherente kanalen, d.w.z. via bussen die de gecodeerde informatie coherent vasthouden. Het belang van de taak ligt op meerdere niveaus: van veilige communicatie tot het schalen van kwantumcomputers. Het eerste kan van fundamenteel belang zijn bij bijvoorbeeld regeringsverkiezingen of banktransacties, maar zelfs om het recht op privacy van individuen te waarborgen. Het tweede kan de weg openen naar bijvoorbeeld snellere en preciezere oplossingen voor problemen in de chemie (voor de ontwikkeling van geneesmiddelen) of de materiaalkunde (milieuvriendelijkere zonnecellen). Op dit moment bevinden quantumcommunicatie en -computing zich in een vergelijkbaar stadium als de vroege computers: de machines hebben zeer weinig connectiviteit en vereisen grote ruimtes en specialisten om bediend te worden. Over een paar jaar kunnen we verwachten dat deze systemen steeds meer met elkaar verbonden zullen zijn, geschaald zullen worden en gemakkelijker te gebruiken zullen zijn. In dit proefschrift presenteren wij het werk dat is verricht om kwantumkanalen te creëren met behulp van hoogfrequente mechanische oscillatoren.

In hoofdstuk 1 presenteren we recente vooruitgang op het gebied van kwantumcommunicatie met verschillende soorten systemen, zowel op de lange als op de korte afstand. We introduceren ook hoe hoogfrequente mechanische oscillatoren een belangrijke rol zouden kunnen spelen in dit onderzoeksgebied. Wij bespreken de huidige uitdagingen en beperkingen en mogelijke toekomstige ontwikkelingen.

In hoofdstuk 2 voeren we een optomechanische kwantumteleportatie uit. In dit werk teleporteren we een polarisatie-gecodeerd telecomfoton naar een kwantumgeheugen, gemaakt door twee single mode mechanische oscillatoren in een dual-rail configuratie. Dit werk is een stap in de richting van entanglement-swapping (ook wel 'teleportatie van verstrengelde toestanden' genoemd) en vormt een principebewijs voor kwantumrepeaters (met behulp van een DLCZ-schema).

In hoofdstuk 3 rapporteren we het eerste experiment met multimode mechanische apparaten. Deze apparaten worden gevormd door een optomechanische holte met één modus, gekoppeld aan een mechanische golfgeleider met één modus (beëindigd met een fonische spiegel). Wij tonen aan dat de niet-klassieke informatie in de optomechanische holte on-chip kan worden geleid in de mechanische golfgeleider, met als getuige de kruiselingse correlatie tussen de verstrooide fotonen. De niet-uniforme afstand tussen de mechanische modi verlaagt echter sterk de maximumwaarde van de gemeten niet-klassieke correlatie. Dit is sterk verbeterd met het nieuwe ontwerp van het apparaat. Met dit ontwerp zijn we in staat twee reizende fononen in de mechanische golfgeleider te verstrengelen, zoals te zien is in hoofdstuk 4. Op deze manier laten we zien dat de reizende fononen kunnen worden gebruikt om kwantumverstrengeling on-chip te verspreiden, een eerste stap naar het verbinden van kwantumapparaten op korte schaal.

In hoofdstuk 5 meten we in de tijd de frequentiejitter van twee spectraal dicht bij elkaar liggende mechanische modi van hetzelfde apparaat. We tonen aan dat de frequentieverspreiding van de modi niet gecorreleerd is in de tijd, en dus zal de coherentielengte van de reizende informatie uiteindelijk beperkt worden door de jitter. Dit resultaat toont het belang aan van een gedetailleerde studie van de oppervlaktedefecten.

In de conclusie 6 vatten we de bevindingen van deze experimenten samen en bespreken we de toekomstige ontwikkelingen op dit gebied.

1

INTRODUCTION

In recent years high frequency phonons (with frequency $\nu \approx 5\,\mathrm{GHz}$*) have proven to be a resourceful platform for quantum information processes. From being used as quantum buses between heterogeneous systems [1, 2], to intermediary for transduction from microwave to optical photons [3–5] and as quantum memories that could be used in a DLCZ scheme of quantum repeaters [6]. These applications are possible thanks to the several interesting properties of phonons: a much slower group velocity compared to light, a much smaller wavelength compared to microwaves, a long lifetime and a strong coupling to several types of systems. Here we will discuss recent results in the field of quantum information using phonons, their limitations, and the possible future developments in the field.*

1.1. QUANTUM COMMUNICATION

THE field of quantum information has been receiving a growing interest in the past years. A way of visualizing it, even though imperfect, can be through the number of papers published and the citations of some fundamental papers on the subject per year. We report in Fig. 1.1a the number of papers per year with the word "quantum communic*" (in orange) and "quantum comput*" (in blue) in the title or the abstract, and in Fig. 1.1b the citation of the three major work of the recent Nobel prize for physics (2022). Both graphs show how the work in the area is steadily increasing. From the first graph, we can extract a rate of doubling from the mid '90 to 2022 every ≈3.5 years, 5 times faster compared to the general field of physics [7].

But what is quantum communication? In broad terms it is the ability to link multiple quantum systems while maintaining the coherence of the information exchanged. The separate quantum systems are in nodes, connected via the quantum channels. The information to be exchanged are traveling qubits used to generate entanglement between the remote nodes. The communication can be done for long or short distances: the first one is meant to create a so-called quantum network, for example between neighboring cities, while the second can be used to connect modular quantum computers in the same dilution refrigerator (so on a wafer/chip scale) or between different laboratories. It is to be noted that for some systems a direct transmission of the qubit is possible (like in gate-defined quantum dots [8]). However, most systems rely on an intermediary flying qubit to transmit the information (photons generally, or phonons). We will focus on the latter architecture. We will now discuss recent advancements in both long and short range communication and their challenges. In the whole thesis, we will focus mainly on the discrete variable architecture, despite some of the work and concepts could also be used with continuous variables.

LONG DISTANCE COMMUNICATION

The term "long distance communication" is generally used for distances $\gtrsim$km between the sender and receiver of the information. The long term goal is to connect neighboring cities in a quantum network, similar to the classical network.

In long distance communication, it is useful to use traveling photons at telecom wavelength as carriers. Photons have a very high group velocity (in free space and optical fibers), can have extremely low propagation losses (as low as 0.15 dB/km in commercially available fibers), and could already use the infrastructures and technologies developed for classical communication. Despite the low loss, direct communication rates between nodes scale exponentially with the distance between the nodes, and the no-cloning theorem prevents the use of any amplifiers (as done instead in classical communication). For this reason, it will be required to divide the distance between the nodes into shorter segments, each with an absorption well below the propagation length of the flying qubit used. This quantum repeaters architecture allows having high rates between the nodes for distances $\gtrsim$100 km [9, 10]. The so-called DLCZ scheme, from the names of the creators (Duan, Lukin, Cirac and Zoller), is one of the most important architectures and is of fundamental importance to realize the quantum network [11]. A scheme of this is shown in Fig. 1.2a. Several types of systems have been used to demonstrate milestones in the field: with atomic ensemble (see [12] or [13, 14]), single atoms [15], solid

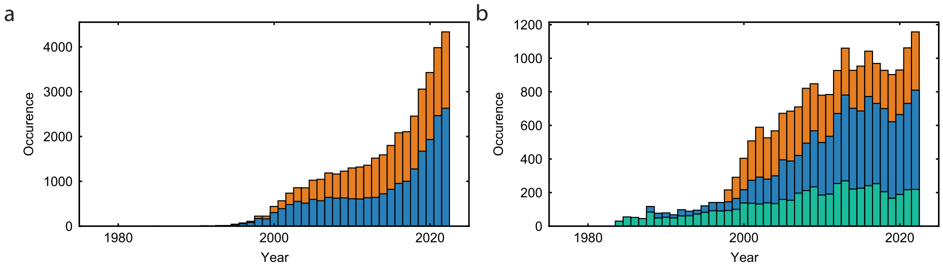

Figure 1.1: **Papers and citation in quantum.** a) Histogram of the number of papers per year that have the title or in the abstract "quantum communic*"(in orange) and "quantum comput*" (in blue), as from web of science. b) Histogram of the number of citations per year for "Proposed Experiment to Test Local Hidden-Variable Theories" from Clauser et al. [22] (in green),"Experimental Test of Bell's Inequalities Using Time-Varying Analyzers" from Aspect et al. [23] (in blue) and "Experimental quantum teleportation" from Bouwmeester et al. [24] (in orange), as from Google scholar. These are some of the works done by Clauser, Aspect and Zeilinger that make them Nobel Prize laureates in 2022. The metrics shown here, even if far from being perfect, show the impressive growth in interest in the past years in quantum information.

state defects with spins [16–18], single trapped ion [19], quantum dots [20] and down-converted photons [21]. The distances between the nodes in these works range from lab scale (few meters), to several km using optical fibers up to hundreds with a satellite link. The key challenge is to find a system that is scalable, with long coherence time (or with a quantum memory easy to interface), with high retrieval efficiency, with real-time feed-forwards operations and ideally native to telecom wavelength.

SHORT DISTANCE COMMUNICATION

We use the term "short distance communication" referring to the transmission of information on wafer/chip scale or lab scale. In this case, the goal is to have an easier scaling of quantum computers or to interconnect heterogeneous quantum systems.

The short scale communication is pursued to address the difficulties to scale quantum computers, which is mostly due to from technical reasons. The two quantum systems on chip which are mature for computation (superconducting qubits and quantum dots) have a challenging scaling, despite their relatively small footprint. One possible solution to address this is to create a modular quantum computer. The computer will be formed by a matrix of nodes in which several computational qubits will be closely packed together, and by some (on-chip) quantum channel to connect the nodes. Work in this direction has been done for both superconducting qubits [25–28] and quantum dots (see for example [29]). We represent in a schematic way the described short distance communication in Fig. 1.2b (left).

In most cases, as described before, modular quantum computers are made of homogeneous systems. However, we report also another challenge, which has received more and more attention in the community in recent years: to connect heterogeneous systems in the same chip for integrated quantum devices. Hybrid quantum systems are a fascinating new line of research. The idea is to use the best of each system connected to try to outperform the single components. Most likely, it will be advantageous to interface different types of qubits instead of using a single type. This connectivity should allow using the desired properties of the single systems. Some exciting future works in this direction could be on interfacing a spin memory to a superconducting qubit to allow an extremely long storage time of the computation results [30]. We represent this in an illustrative way in Fig. 1.2b (right). The challenge here is to design a bus that can be interfaced with several types of systems, that has a slow group velocity (to also create delay lines) and that is scalable.

In this thesis, we propose in chapter 3 and 4 a possible candidate for both long and short distance quantum communication, that could interface homogeneous and heterogeneous systems.

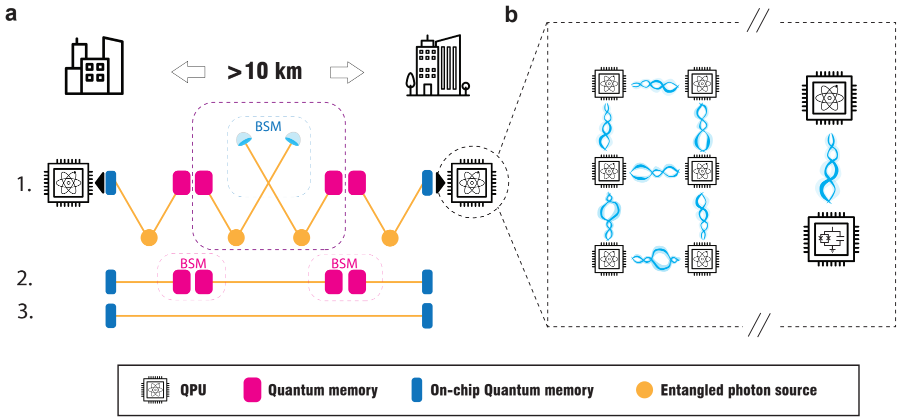

Figure 1.2: **Quantum communication.** a) Schematic of a possible scheme for quantum repeaters (DLCZ scheme). The communication within two nodes (further than 10 km, so for example, in two different cities) is done by diving the total distance in segments. Each segment (encircled in the dashed purple rectangle) has two sources of entangled photons and two quantum memories and a Bell state measurement station (BSM). This segment can be repeated multiple times to divide the total distance into segments as small as needed. Since the protocol relies on probabilistic emission of the photons the quantum memory is fundamental to synchronize the attempts and store the generated entangled state. In this simplified scheme, it's performed 1. a BSM on the repeater(s) to entangle the quantum memories of the repeaters, 2. an entanglement swapping on the memories so that 3. the two end nodes are entangled. b) Representation of modular quantum computers (left) and connection between two heterogeneous systems on chip (right). In this cases, the quantum channel is for short distance communication (on-chip, for example). The blue lines are a representation of entanglement between the nodes.

1.1.1. PHONONS IN QUANTUM COMMUNICATION

Within all systems, phononic ones have some peculiar characteristic which makes them a promising candidate for solving some of the challenges in quantum communication describe before. They have a much slower group velocity compared to light (on the order of 1×10^3 m/s, so 7-8 order of magnitudes smaller than the speed of light), a much smaller wavelength compared to microwaves (on the order of μm, while for microwaves is mm), a long lifetime compared to most systems (up to seconds) and a strong coupling to several types of devices (up to 10 MHz in the case of superconducting qubits). We believe that phonons can be an extremely useful resource to connect heterogeneous and homogeneous systems (both for long distance communication and locally on chip). We want to stress that in the case of phonons, the short distance communication is only for chip scale since waveguide systems like coax cables or optical fibers are not available.

We will now discuss recent results using phonons for quantum communication and the challenges to overcome.

LONG DISTANCE COMMUNICATION

For long distance communication, phonons have been proven to be a useful tool as quantum memory for DLCZ scheme [6]. The long lifetime, up to second [31], make them very promising candidates for this task. Another advantage is that the optical resonance can be designed to match in frequency the one of the other systems (for example, down converted light from NV centers), making them easy to integrate and connect via the photonic link. Some possible future works in this direction could be entanglement swapping, and entanglement between a color center (NV or SnV in diamond) and a mechanical registry. Another possible future experiment could be the teleportation of a quantum state into a device as the one presented in chapter 3 and 4. Teleportation into a mechanical registry is shown in chapter 2, where we use a pair of single mode mechanical oscillators as memory. Instead, using a multi-mode device allows us to perform the same experiment with a single device making the fabrication requirements less stringent.

Phonons are also used as mediators of the interaction between superconducting qubits and photons, for frequency conversion [3–5]. In this case, the mechanical oscillator serves as an intermediate step from the GHz photons of superconducting qubits to THz optical photons (used for long distance communication). This step serves to take advantage of the relatively high electromechanical and optomechanical cooperativities that give an efficient conversion without the strong pumps needed in the direct electro-optical case [32, 33]. Despite some systems have very little added noise [34], the conversion efficiencies are still far from unity limiting the rates at which experiments can be performed. Apart from the challenges of noise and efficiency, the transducer also needs to have high enough bandwidth and come with an easy integration on-chip. A possible future work in this direction could be the entanglement between two superconducting qubits in two separate dilution refrigerators. This will be a big step towards the quantum network between quantum computers.

SHORT DISTANCE COMMUNICATION

For the short range communication, we can divide the phononic systems into 3 groups: Bulk acoustic waves (BAW), Surface Acoustic Waves (SAW) and 1D acoustic waves (that we will often refer to as Nanobeam, since are the most used platform at the moment). In Fig. 1.3a, b, c, a cartoon image of each is presented.

BAWs are generally generated via a piezo dome. The phonon propagation is confined between the dome, which acts as a focusing mirror, and the other face of the chip. The (0,0)-Laguerre-Gaussian mode is generally used. Since the mechanical wavelength is much shorter than the size of most chip, these systems are also called High-Overtone Bulk Acoustic Resonator (hBAR). The most interesting feature is that the lifetime of this mode can be several hundreds of microseconds [40]. Thanks to the piezo actuation,

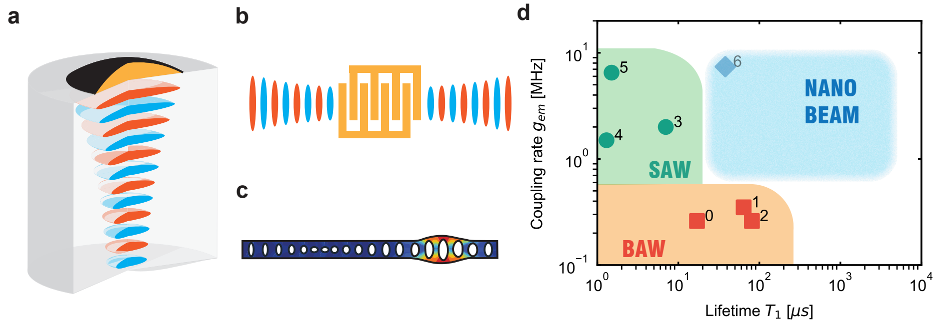

Figure 1.3: **Cartoon picture of several types of mechanical systems.** a) The 3D type Bulk Acoustic Wave (BAW) with the piezoelectric dome on top. b) The 2D type Surface Acoustic Wave (SAW) and the InderDigitated Transducer (IDT) to create it. c) The 1D type Nanobeam developed in the work presented in this thesis in chapter 3 and 4. d) Plot of the coupling rate between a superconducting qubit and a mechanical line (Fabry-Pérot cavity for phonons) in the function of the lifetime of the phonons for: BAW (0, 1, 2, for [35–37]), SAW (3, 4, 5, for [1, 38, 44], and a case with nanobeam (6, for [5]). Note that for 4 the coupling rate is not reported so we extract it from the lifetime of the qubit when fully coupled. Note also that in the SAW case, some works have shown a higher coupling rate (between 20 MHz and 40 MHz, but have no phononic cavity (so no phononic lifetime can be inferred) [39]. Finally, note that for 6, the phonons are confined so in this case we can only use this datapoint as a reference for the expected coupling with this geometry. This last coupling rate, together with the lifetime reported in chapter 3, show that the nanobeam have the capability of having both high rates of coupling and extremely long lifetime making them suitable candidates for communication between quantum circuits on-chip. The coloured areas are only to schematically group the systems and show the possible range of parameters achievable.

connecting superconducting circuit to this system is possible both in a direct way [35] and in a flip chip architecture [36, 41]. However the coupling between the system is relatively low (~ 100 kHz), and, given the massive size (diameter of the dome ~ 100 µm, thickness of the chip ~ 1 mm), this system is also quite difficult to scale. An interesting prospect is to use them to couple the two sides of the chip. In this case, the flipped chip is used for connecting other systems to form a stack of planar circuits interconnected in the third dimension via the hBARs.

SAWs are waves propagating on the surface of a bulk material. The penetration depth is of the order of the wavelength and are generally actuated via InterDigitated Transducers (IDTs). IDTs are simply metallic strips alternatively connected to two electrodes and with a spacing of the order of the mechanical wavelength. The number of strips and length determine the impedance and the bandwidth of the transducer. IDTs can be done with asymmetric strips to generate the wave in a single direction [42] and curved to create focused waves [43]. Since they also have an electrical actuation and an impedance easy to design, it is possible to integrate them with superconducting circuits [39, 44]. Despite the easy connectivity, they still have the severe limitation of a short lifetime ($T_1 \approx 1\,\mu s$) which limits the applications of this type of system. Moreover, SAWs still have quite a large footprint having a transversal size of ~ 100 µm, making the scaling challenging.

The last type of system is the nanobeam, described in detail in chapter 3 and 4. In this case, the phononic excitation is strongly confined in the transversal direction since

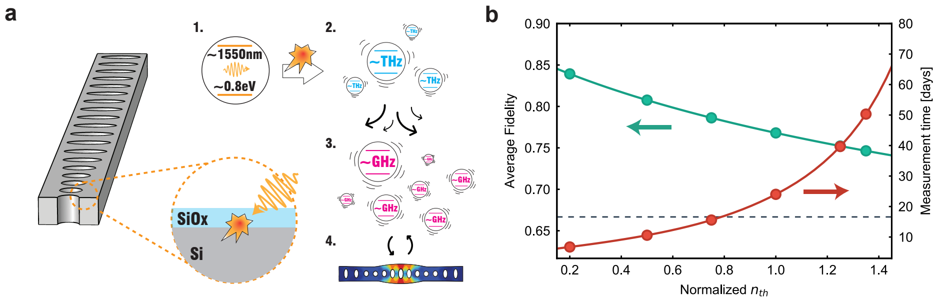

Figure 1.4: **Thermal population in silicon nanodevices.** a) 3D rendering of a silicon nanobeam (cut in the middle of the optomechanical cavity). The zoom is a cartoon image of the absorption process of a photon (yellow arrow) happening in the Si/SiOx interface region caused by point defects. The diagram shows a cartoon picture of the process: 1. absorption of the telecom photon, 2. phonon-assisted relaxation that generates a shower of high energy phonons in the THz frequencies, 3. decay via multi-phonon interaction in a bath of GHz phonons. This thermal bath is responsible to increase the thermal population of the mechanical mode of the nanobeam (4.). b) Teleportation fidelity and total integration time for the teleportation experiment, shown in chapter 2, in the function of the normalized thermal occupation of the mechanical modes (with unity value for the one measured in the paper). In this simulation, all the other parameters are left constant (including the scattering probabilities) to show how the integration time depends heavily on the n_{th}. The horizontal dashed line is the classical limit of the fidelity.

the beam dimensions are 500 nm x 250 nm. This allows the system to be scalable. A remarkable property is the (engineerable) lifetime that can be extended up to several milliseconds, as shown in chapter 3. Since the group velocity is ~ 1 µm/ns, the theoretical traveling length of the phonons could be as high as several meters, allowing lossless connectivity on-chip. In recent years it has been developed a way to electrically actuate the excitation in the waveguide [3–5]. In all these works the goal was to transduce microwave to optical signal, but using this type of device with a long mechanical waveguide should be a feasible implementation. By doing so we could excite a phononic packet in the waveguide deterministically, as done in the other systems presented before, and with an extremely low thermal population. In Fig. 1.3d, we show the coupling rates of BAW, SAW and nanobeam systems in function of their lifetime. The nanobeams are the only system with both a high coupling rate and a long lifetime, making them a perfect candidate to interconnect superconducting circuit on chip.

DEFECTS IN SILICON

In the previous section, we described how phonons, thanks to their unique set of properties, are a promising platform for quantum communication. Their versatility and capabilities have been shown in several groundbreaking works over the years. We want now to discuss briefly defects in silicon since they are thought to be the cause of the two major challenges in the type of devices described in the thesis: optical absorption, which gives a thermal population in the mechanical mode, and mechanical spectral diffusion (frequency jitter), that causes dephasing. Solving these two challenges (or mitigating them) will unlock many experiments and applications, making the use of phonons in quantum communication even more attractive. Despite being a very technical challenges, the process of solving it could also help in understanding the nature of defects in silicon (and in amorphous materials and at surfaces). Since other systems are facing analogous challenges, e.g. superconducting circuits [45, 46], this knowledge could also be applied to other fields of physics.

In all chapters, the manipulation of the state was performed using optomechanical interactions. These interactions are probabilistic and require strong optical pumps. To increase the probability of scattering it is needed to increase the pump power. However, the residual absorption of photons in the device leads to an increase in the thermal population of the mechanical mode. The optical absorption should be caused by point defects, most likely formed by the dangling bonds in the Si/SiOx interface [47]. This interface has states with energies in the bandgap of silicon [48]. Silicon Oxide grows naturally on silicon if exposed to air [49]. The sample stays in air for $\gtrsim$20 min between the final strip of oxide with a HydroFluoric (HF) acid dip and being in the vacuum of the dilution refrigerator, a time sufficient to form a few nm of oxide on the surface. It is also seen that the longer the mounting time, the worse the average absorption of the devices. In Fig. 1.4a we show a cartoon picture of the model developed in the years [31, 50]. Because of the absorption, all the experiments done with optomechanical techniques have rates limited by the thermal population. A possible solution can be to use 2D structure, that should have better thermal anchoring to the substrate [51] or change the way the phononic excitation is created and measured (as proposed in the section before). In Fig. 1.4b, we show the effect of the thermal occupation on the teleportation fidelity and integration time (see chapter 2 for more). As visible, the integration time increase dramatically even with a small increase in the thermal occupancy.

The mechanical jitter, instead, is thought to be caused by another type of defect located near the surface of the device (in the silicon and also in the SiOx). In this case, the defect is formed by some atoms that have two arrangements in space with nearly degenerate energies. This can be modeled as Tunneling Systems (TS) [52] or Two Level Systems (TLS) [6, 31, 50]. These fluctuating TLSs have a mechanical dipole that couples to the strain field of the mechanical mode. The resonant TLSs, i.e. with energies close to the one of the mechanical mode of interest, are believed to cause the slow shift of the resonant frequency of the mechanical mode (time scale of hours) and the mechanical jitter (time scale sub-ms) [6, 31]. Since they should be created by damage in the silicon while dry etching [53], these defects are hard to eliminate. While previous work studied in detail the coherence properties of single mode mechanical memory, in this thesis in chapter 3 and 4 we present devices with several mechanical modes closely spaced (average frequency spacing ~10 MHz). We found that the frequency jitter between adjacent modes is completely uncorrelated. We report these results in chapter 5, where we prove this with fast scans of the spectrum and with time traces of the mechanical frequencies. We use a measured time trace to simulate the population in the optomechanical cavity, as done in chapter 3, to show how this jitter could affect the coherent storage and transport of information across the chip. In Fig. 1.5a we show the frequency shift in time of the mechanical modes measured (mode A in orange and mode B in blue, see chapter 5 for more). We use this data to simulate the mechanical population in time in the cavity. The dashed black rectangle highlights the data used for the simulation. We use two modes spaced on average by 10 MHz, and we report the result of the simulation in Fig. 1.5b in

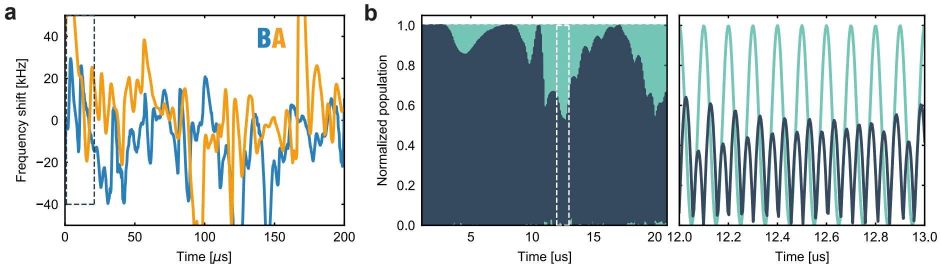

Figure 1.5: **Frequency diffusion in silicon nanodevices** a) Frequency shift of the mechanical mode A (in orange) and B (in blue), as measured from chapter 5. b) Simulation of the population rephasing in the optomechanical cavity in the ideal case (green, with zero jittering) and with the measured jitter (dark grey). In the left plot is clear that the maximum population in the cavity have values smaller than unity for several time ranges. From the plot on the right, which is a zoom of the area highlighted by the white rectangle in the plot on the left, is visible the bouncing pattern with a period of 100 ns (the spacing between the mechanical modes is 10 MHz). The code used is identical to the one used in chapter 3. We use a cubic spline of the jitter data to have enough time resolution to plot the bouncing pattern.

dark grey. We also plot, for comparison, the ideal case with zero jittering (in green). It is visible from the graph that the jittering reduces the coherent population that rephases in the optomechanical cavity at certain times. For some time the population rephase to unity, and so at that time the retrieving efficiency of information is not affected by the jittering. However, since it's needed to average on several repetitions and in each the population pattern will be different, the jitter will result in a lower coherent population that can be retrieved. This effect will be even bigger with more modes. The white dashed rectangle is the area plotted in Fig. 1.5b on the right plot, which is a zoom to see the fast timescale behavior. We want to stress that, since these TLSs are saturable (for example with strong optical power or high temperature of the device (>100 mK)), it might be possible to drive them with an external RF field to decouple them from the mechanical mode. In this way, the coherence time of the devices will be expected to increase substantially.

1.2. QUANTUM ACOUSTICS

Another exciting direction of research for the system presented in chapter 3 and 4, is to perform equivalent experiments of quantum optics using phonons. For this reason, we generally referred to this field as quantum acoustic.

In recent works it has been shown a waveguide [1], a Beam Splitter [38] and a phase shifter [54] for SAWs, making them a mature technology for the coherent manipulation of phonons on chip. Moreover, a beam splitter has been proven for BAWs [55], showing how also this system can be a candidate for this type of experiment. However, the strong confinement of the nanobeam and the long lifetime make them a more suitable candidate. In chapter 3 and 4, we have reported a waveguide for single phonons. To complete the toolbox, it's needed to design and measure a beam splitter and a phase shifter. Note that for the latter a possible design has been simulated [56]. Some possible experiments could be a Hambury-Brown-Twiss interferometry [57], with the phonons interfering via the phononic beam splitter. Another possibility could be to do boson sampling using phonons [58, 59]. In the phononic case the sources, linear transformation and detectors are all on-chip making the system more compact and scalable.

REFERENCES

[1] A. Bienfait, K. J. Satzinger, Y. P. Zhong, H.-S. Chang, M.-H. Chou, C. R. Conner, E. Dumur, J. Grebel, G. A. Peairs, R. G. Povey, and A. N. Cleland, Phonon-mediated quantum state transfer and remote qubit entanglement, Science **364**, 368 (2019).

[2] A. Zivari, R. Stockill, N. Fiaschi, and S. Gröblacher, Non-classical mechanical states guided in a phononic waveguide, Nature Phys. **18**, 789 (2022).

[3] M. Mirhosseini, A. Sipahigil, M. Kalaee, and O. Painter, Superconducting qubit to optical photon transduction, Nature **588**, 599 (2020).

[4] W. Jiang, F. M. Mayor, S. Malik, V. Laer, T. P. Mckenna, R. N. Patel, J. D. Witmer, and A. H. Safavi-Naeini, Optically heralded microwave photons, arXiv:2210.10739v1 .

[5] M. J. Weaver, P. Duivestein, A. C. Bernasconi, S. Scharmer, M. Lemang, T. C. Van Thiel, F. Hijazi, B. Hensen, S. Gröblacher, and R. Stockill, An integrated microwave-to-optics interface for scalable quantum computing, (2022), arXiv:2210.15702v1 .

[6] A. Wallucks, I. Marinković, B. Hensen, R. Stockill, and S. Gröblacher, A quantum memory at telecom wavelengths, Nat. Phys. **16**, 772 (2020).

[7] R. Sinatra, P. Deville, M. Szell, D. Wang, and A.-L. Barabási, A century of physics, NATURE PHYSICS | **11** (2015).

[8] R. P. G. McNeil, M. Kataoka, C. J. B. Ford, C. H. W. Barnes, D. Anderson, G. A. C. Jones, I. Farrer, and D. A. Ritchie, On-demand single-electron transfer between distant quantum dots, Nature **477**, 439 (2011).

[9] H. J. Briegel, W. Dür, J. I. Cirac, and P. Zoller, Quantum repeaters: The role of imperfect local operations in quantum communication, Physical Review Letters **81**, 5932 (1998).

[10] C. Simon, Towards a global quantum network, Nature Photon. **11**, 678 (2017).

[11] L. M. Duan, M. D. Lukin, J. I. Cirac, and P. Zoller, Long-distance quantum communication with atomic ensembles and linear optics., Nature **414**, 413 (2001).

[12] N. Sangouard, C. Simon, H. de Riedmatten, and N. Gisin, Quantum repeaters based on atomic ensembles and linear optics, Rev. Mod. Phys. **83**, 33 (2011).

[13] B. Julsgaard, A. Kozhekin, and E. S. Polzik, Experimental long-lived entanglement of two macroscopic objects, Nature **413**, 400 (2001).

[14] Y. Yu, F. Ma, X. Y. Luo, B. Jing, P. F. Sun, R. Z. Fang, C. W. Yang, H. Liu, M. Y. Zheng, X. P. Xie, W. J. Zhang, L. X. You, Z. Wang, T. Y. Chen, Q. Zhang, X. H. Bao, and J. W. Pan, Entanglement of two quantum memories via fibres over dozens of kilometres, Nature **578**, 240 (2020), arXiv:1903.11284 .

[15] J. Hofmann, M. Krug, N. Ortegel, L. Gérard, M. Weber, W. Rosenfeld, and H. Weinfurter, Heralded entanglement between widely separated atoms, Science **336**, 72 (2012).

[16] E. Togan, Y. Chu, A. S. Trifonov, L. Jiang, J. Maze, L. Childress, M. V. Dutt, A. S. Sørensen, P. R. Hemmer, A. S. Zibrov, and M. D. Lukin, Quantum entanglement between an optical photon and a solid-state spin qubit, Nature **466**, 730 (2010).

[17] B. Hensen, H. Bernien, A. E. Dréau, A. Reiserer, N. Kalb, M. S. Blok, J. Ruitenberg, R. F. L. Vermeulen, R. N. Schouten, C. Abellán, W. Amaya, V. Pruneri, M. W. Mitchell, M. Markham, D. J. Twitchen, D. Elkouss, S. Wehner, T. H. Taminiau, and R. Hanson, Loophole-free Bell inequality violation using electron spins separated by 1.3 kilometres, Nature **526**, 682 (2015).

[18] M. Pompili, S. L. Hermans, S. Baier, H. K. Beukers, P. C. Humphreys, R. N. Schouten, R. F. Vermeulen, M. J. Tiggelman, L. dos Santos Martins, B. Dirkse, S. Wehner, and R. Hanson, Realization of a multinode quantum network of remote solid-state qubits, Science **372**, 259 (2021), arXiv:2102.04471 .

[19] D. L. Moehring, P. Maunz, S. Olmschenk, K. C. Younge, D. N. Matsukevich, L.-M. Duan, and C. Monroe, Entanglement of single-atom quantum bits at a distance, Nature **449**, 68 (2007).

[20] A. Delteil, Z. Sun, W. B. Gao, E. Togan, S. Faelt, and A. Imamolu, Generation of heralded entanglement between distant hole spins, Nature Physics 2016 12:3 **12**, 218 (2015), arXiv:1507.00465 .

[21] J. Yin, Y. Cao, Y. H. Li, S. K. Liao, L. Zhang, J. G. Ren, W. Q. Cai, W. Y. Liu, B. Li, H. Dai, G. B. Li, Q. M. Lu, Y. H. Gong, Y. Xu, S. L. Li, F. Z. Li, Y. Y. Yin, Z. Q. Jiang, M. Li, J. J. Jia, G. Ren, D. He, Y. L. Zhou, X. X. Zhang, N. Wang, X. Chang, Z. C. Zhu, N. L. Liu, Y. A. Chen, C. Y. Lu, R. Shu, C. Z. Peng, J. Y. Wang, and J. W. Pan, Satellite-based entanglement distribution over 1200 kilometers, Science **356**, 1140 (2017), arXiv:1707.01339 .

[22] J. F. Clauser, M. A. Horne, A. Shimony, and R. A. Holt, Proposed experiment to test local hidden-variable theories, Phys. Rev. Lett. **23**, 880 (1969).

[23] A. Aspect, J. Dalibard, and G. Roger, Experimental test of bell's inequalities using time-varying analyzers, Phys. Rev. Lett. **49**, 1804 (1982).

[24] D. Bouwmeester, J.-W. Pan, K. Mattle, M. Eibl, H. Weinfurter, and A. Zeilinger, Experimental quantum teleportation, Nature **390**, 575 (1997).

[25] J. Majer, J. M. Chow, J. M. Gambetta, J. Koch, B. R. Johnson, J. A. Schreier, L. Frunzio, D. I. Schuster, A. A. Houck, A. Wallraff, A. Blais, M. H. Devoret, S. M. Girvin, and R. J. Schoelkopf, Coupling superconducting qubits via a cavity bus, Nature **449**, 443 (2007), arXiv:0709.2135 .

[26] R. Barends, J. Kelly, A. Megrant, D. Sank, E. Jeffrey, Y. Chen, Y. Yin, B. Chiaro, J. Mutus, C. Neill, P. O'Malley, P. Roushan, J. Wenner, T. C. White, A. N. Cleland, and J. M. Martinis, Coherent josephson qubit suitable for scalable quantum integrated circuits, Phys. Rev. Lett. **111**, 080502 (2013).

[27] P. Magnard, S. Storz, P. Kurpiers, J. Schär, F. Marxer, J. Lütolf, J.-C. Besse, M. Gabureac, K. Reuer, A. Akin, B. Royer, A. Blais, and A. Wallraff, Microwave quantum link between superconducting circuits housed in spatially separated cryogenic systems, Phys. Rev. Lett. **125**, 260502 (2020).

[28] J. Niu, L. Zhang, Y. Liu, J. Qiu, W. Huang, J. Huang, H. Jia, J. Liu, Z. Tao, W. Wei, Y. Zhou, W. Zou, Y. Chen, X. Deng, X. Deng, C. Hu, L. Hu, J. Li, D. Tan, Y. Xu, F. Yan, T. Yan, S. Liu, Y. Zhong, A. N. Cleland, and D. Yu, Low-loss interconnects for modular superconducting quantum processors, Nature Electronics 10.1038/s41928-023-00925-z (2023).

[29] L. M. K. Vandersypen, H. Bluhm, J. S. Clarke, A. S. Dzurak, R. Ishihara, A. Morello, D. J. Reilly, L. R. Schreiber, and M. Veldhorst, Interfacing spin qubits in quantum dots and donors—hot, dense, and coherent, npj Quantum Inf. **3**, 1 (2017).

[30] M. H. Abobeih, J. Cramer, M. A. Bakker, N. Kalb, M. Markham, D. J. Twitchen, and T. H. Taminiau, One-second coherence for a single electron spin coupled to a multi-qubit nuclear-spin environment, Nature Communications 2018 9:1 **9**, 1 (2018), arXiv:1801.01196 .

[31] G. S. MacCabe, H. Ren, J. Luo, J. D. Cohen, H. Zhou, A. Sipahigil, M. Mirhosseini, and O. Painter, Nano-acoustic resonator with ultralong phonon lifetime, Science **370**, 840 (2020).

[32] T. Bagci, A. Simonsen, S. Schmid, L. G. Villanueva, E. Zeuthen, J. Appel, J. Taylor, A. Sørensen, K. Usami, A. Schliesser, and E. Polzik, Optical detection of radio waves through a nanomechanical transducer., Nature **507**, 81 (2014).

[33] R. Stockill, M. Forsch, F. Hijazi, G. Beaudoin, K. Pantzas, I. Sagnes, R. Braive, and S. Gröblacher, Ultra-low-noise microwave to optics conversion in gallium phosphide, Nature Communications **13**, 10.1038/s41467-022-34338-x (2022), arXiv:2107.04433 .

[34] R. D. Delaney, M. D. Urmey, S. Mittal, B. M. Brubaker, J. M. Kindem, P. S. Burns, C. A. Regal, and K. W. Lehnert, Superconducting-qubit readout via low-backaction electro-optic transduction, Nature **606**, 489–493 (2022).

[35] Y. Chu, P. Kharel, W. H. Renninger, L. D. Burkhart, L. Frunzio, P. T. Rakich, and R. J. Schoelkopf, Quantum acoustics with superconducting qubits, Science **358**, 199 (2017).

[36] Y. Chu, P. Kharel, T. Yoon, L. Frunzio, P. T. Rakich, and R. J. Schoelkopf, Creation and control of multi-phonon fock states in a bulk acoustic-wave resonator, Nature **563**, 666 (2018).

[37] U. von Lüpke, Y. Yang, M. Bild, L. Michaud, M. Fadel, and Y. Chu, Parity measurement in the strong dispersive regime of circuit quantum acoustodynamics, Nature Physics 2022 18:7 **18**, 794 (2022), arXiv:2110.00263 .

[38] H. Qiao, E. Dumur, G. Andersson, H. Yan, M.-H. Chou, J. Grebel, C. R. Conner, Y. J. Joshi, J. M. Miller, R. G. Povey, X. Wu, and A. N. Cleland, Developing a platform for linear mechanical quantum computing (2023), arXiv:2302.07791 [quant-ph] .

[39] M. V. Gustafsson, T. Aref, A. F. Kockum, M. K. Ekström, G. Johansson, and P. Delsing, Propagating phonons coupled to an artificial atom, Science **346**, 207 (2014).

[40] V. J. Gokhale, B. P. Downey, D. S. Katzer, N. Nepal, A. C. Lang, R. M. Stroud, and D. J. Meyer, Epitaxial bulk acoustic wave resonators as highly coherent multi-phonon sources for quantum acoustodynamics, Nature Communications **11**, 1 (2020), arXiv:2003.11097 .

[41] M. Bild, M. Fadel, Y. Yang, U. von Lüpke, P. Martin, A. Bruno, and Y. Chu, Schrödinger cat states of a 16-microgram mechanical oscillator (2022), arXiv:2211.00449 [quant-ph] .

[42] É . Dumur, K. J. Satzinger, G. A. Peairs, M.-H. Chou, A. Bienfait, H.-S. Chang, C. R. Conner, J. Grebel, R. G. Povey, Y. P. Zhong, and A. N. Cleland, Unidirectional distributed acoustic reflection transducers for quantum applications, Applied Physics Letters **114**, 223501 (2019).

[43] M. E. Msall and P. V. Santos, Focusing Surface-Acoustic-Wave Microcavities on GaAs, PHYSICAL REVIEW APPLIED **13**, 14037 (2020).

[44] É. Dumur, K. J. Satzinger, G. A. Peairs, M.-H. Chou, A. Bienfait, H.-S. Chang, C. R. Conner, J. Grebel, R. G. Povey, Y. P. Zhong, and A. N. Cleland, Quantum communication with itinerant surface acoustic wave phonons, npj Quantum Inf. **7**, 173 (2021).

[45] G. J. Grabovskij, T. Peichl, J. Lisenfeld, G. Weiss, and A. V. Ustinov, Strain tuning of individual atomic tunneling systems detected by a superconducting qubit, Science **338**, 232 (2012), https://www.science.org/doi/pdf/10.1126/science.1226487 .

[46] A. P. Place, L. V. Rodgers, P. Mundada, B. M. Smitham, M. Fitzpatrick, Z. Leng, A. Premkumar, J. Bryon, A. Vrajitoarea, S. Sussman, G. Cheng, T. Madhavan, H. K. Babla, X. H. Le, Y. Gang, B. Jäck, A. Gyenis, N. Yao, R. J. Cava, N. P. de Leon, and A. A. Houck, New material platform for superconducting transmon qubits with coherence times exceeding 0.3 milliseconds, Nature Communications 2021 12:1 **12**, 1 (2021).

[47] A. Stesmans, Passivation of Pb0 and Pb1 interface defects in thermal (100) Si/SiO2 with molecular hydrogen, Applied Physics Letters **68**, 2076 (1996).

[48] Y. Yamashita, K. Namba, Y. Nakato, Y. Nishioka, and H. Kobayashi, Spectroscopic observation of interface states of ultrathin silicon oxide, Journal of Applied Physics **79**, 7051 (1996).

[49] M. Morita, T. Ohmi, E. Hasegawa, M. Kawakami, and M. Ohwada, Growth of native oxide on a silicon surface, Journal of Applied Physics **68**, 1272 (1990).

[50] S. M. Meenehan, J. D. Cohen, S. Gröblacher, J. T. Hill, A. H. Safavi-Naeini, M. Aspelmeyer, and O. Painter, Silicon optomechanical crystal resonator at millikelvin temperatures, Phys. Rev. A **90**, 011803 (2014).

[51] H. Ren, M. H. Matheny, G. S. MacCabe, J. Luo, H. Pfeifer, M. Mirhosseini, and O. Painter, Two-dimensional optomechanical crystal cavity with high quantum cooperativity, Nature Communications 2020 11:1 **11**, 1 (2020), arXiv:1910.02873 .

[52] W. A. Phillips, Two-level states in glasses, Reports on Progress in Physics **50**, 1657 (1987).

[53] Y. H. Lee, G. S. Oehrlein, and C. Ransom, Rie-induced damage and contamination in silicon, Radiation Effects and Defects in Solids **111-112**, 221 (1989).

[54] L. Shao, D. Zhu, M. Colangelo, D. Lee, N. Sinclair, Y. Hu, P. T. Rakich, K. Lai, K. K. Berggren, and M. Lončar, Electrical control of surface acoustic waves, Nature Electronics **5**, 348 (2022), arXiv:2101.01626 .

[55] U. von Lüpke, I. C. Rodrigues, Y. Yang, M. Fadel, and Y. Chu, Engineering phonon-phonon interactions in multimode circuit quantum acousto-dynamics (2023), arXiv:2303.00730 [quant-ph] .

[56] J. C. Taylor, E. Chatterjee, W. F. Kindel, D. Soh, and M. Eichenfield, Reconfigurable quantum phononic circuits via piezo-acoustomechanical interactions, npj Quantum Information **8**, 1 (2022), arXiv:2106.05406 .

[57] S. Hong, R. Riedinger, I. Marinković, A. Wallucks, S. G. Hofer, R. A. Norte, M. Aspelmeyer, and S. Gröblacher, Hanbury Brown and Twiss interferometry of single phonons from an optomechanical resonator, Science **358**, 203 (2017).

[58] J. B. Spring, B. J. Metcalf, P. C. Humphreys, W. S. Kolthammer, X. M. Jin, M. Barbieri, A. Datta, N. Thomas-Peter, N. K. Langford, D. Kundys, J. C. Gates, B. J. Smith, P. G. Smith, and I. A. Walmsley, Boson sampling on a photonic chip, Science **339**, 798 (2013), arXiv:1212.2622 .

[59] H. S. Zhong, H. Wang, Y. H. Deng, M. C. Chen, L. C. Peng, Y. H. Luo, J. Qin, D. Wu, X. Ding, Y. Hu, P. Hu, X. Y. Yang, W. J. Zhang, H. Li, Y. Li, X. Jiang, L. Gan, G. Yang, L. You, Z. Wang, L. Li, N. L. Liu, C. Y. Lu, and J. W. Pan, Quantum computational advantage using photons, Science **370**, 1460 (2020), arXiv:2012.01625 .

2

OPTOMECHANICAL QUANTUM TELEPORTATION

Niccolò FIASCHI*, Bas HENSEN*, Andreas WALLUCKS, Rodrigo BENEVIDES, Jie LI, Thiago P. Mayer ALEGRE, Simon GRÖBLACHER

The faithful transfer of an unknown input state onto a remote quantum system, known as quantum teleportation [1], is a key component in long distance quantum communication protocols [2] and distributed quantum computing [3, 4]. In recent years, high frequency nano-optomechanical systems [5] have gained more and more attention as nodes in a future quantum network [6], since they operate on-chip at low-loss optical telecom wavelengths and have long mechanical lifetimes. Recent demonstrations include entanglement between two resonators [7], a quantum memory [8] and microwave to optics transduction [9–11]. Here we demonstrate quantum teleportation of a polarization-encoded optical input state onto the joint state of a pair of nanomechanical resonators,allowing for the first time to store and retrieve an arbitrary qubit state onto a dual-rail encoded optomechanical quantum memory. This work demonstrates the full functionality of a single quantum repeater node, and presents a key milestone towards applications of optomechanical systems as quantum network nodes.

Parts of this chapter have been published in Niccolò Fiaschi*, Bas Hensen*, Andreas Wallucks, Rodrigo Benevides, Jie Li, Thiago P. Mayer Alegre and Simon Gröblacher, *Optomechanical quantum teleportation*, Nat. Photon. 15, 817–821 (2021).
* indicates equal contribution

2.1. INTRODUCTION

HIGH frequency nano-optomechanical systems [5], besides their appeal for probing fundamental quantum physics [12], also hold great promise as nodes in a future quantum network: first, their optical characteristics can be designed to match the particular application, including operation at low-loss telecom wavelengths and matching resonances with other systems (e.g. atomic transitions). Second, the mechanical modes can be designed to coherently store quantum information for more than ten microseconds [8], unparralelled for systems natively operating at telecom wavelength. Third, the mechanical mode offers a direct interface to other quantum systems operating in the gigahertz frequency regime [9–11], such as superconducting qubits, or spin quantum systems.

Quantum teleportation [1] of an unknown input state from an outside source onto a quantum node is considered one of the key components of long distance quantum communication protocols [2, 13]. It has been demonstrated with pure photonic quantum systems [14–17] as well as atomic [18] and solid-state spin systems [19] linked by photonic channels. While quantum teleportation involving the vibrational modes of a diamond has previously been demonstrated [20], the extremely short lifetimes of the system required the mechanical state to be measured before the teleportation protocol was completed. This reverse time-ordering, as well as the operation in the visible wavelength regime, makes the protocol unsuitable for long distance quantum communication.

Here we demonstrate for the first time quantum teleportation of an arbitrary input state onto a long-lived optomechanical quantum memory. In particular, we teleport a polarization encoded photonic qubit at telecom wavelength onto a dual-rail encoded optomechanical quantum memory. The memory is composed of two mechanical resonators, where the quantum information is stored in the single-excitation subspace of the two resonators. The teleportation we perform implements all components of first-level entanglement swapping [2, 21]. Together with the remote generation of a single-excitation [7], or DLCZ-type [22] entanglement, which has been shown individually before, this current experiment demonstrates the combined requirements for a fully functional quantum repeater node [21]. Besides the impact this has on quantum technologies, it also opens the way to create single-phonon arbitrary qubit states of massive, mechanical oscillators, which can be used for testing quantum physics itself and potential decoherence mechanisms leading to quantum-to-classical transition [23, 24].

2.2. METHODS

OUR optomechanical register consists of two silicon photonic crystal nanobeams, A and B, on two separate chips [7]. Both the nanobeams support a co-localized optical and mechanical mode with resonance frequencies in the optical telecom C-band around 1550 nm and the microwave C-band around 5 GHz, respectively. The optical and mechanical modes are coupled through the radiation pressure force and photoelastic effect with a single photon coupling rate $g_0/2\pi \approx 900\,\text{kHz}$. The chips are placed 20 cm apart from each other inside a dilution refrigerator, and the nanobeam resonators are cryogenically cooled close to their quantum ground state of motion. Optical control pulses of 40 ns length that are either blue or red detuned by one mechanical frequency

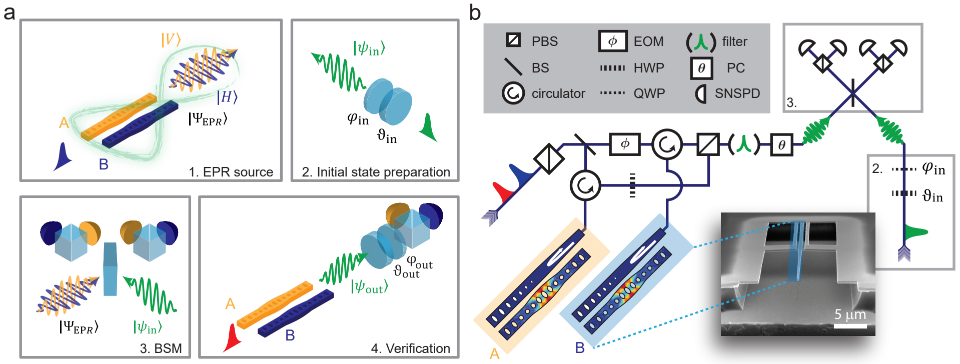

Figure 2.1: **Teleportation protocol and experimental setup.** a) Schematic representation of the key steps of the teleportation protocol and its verification. 1. Realization of an Einstein-Podolsky-Rosen (EPR) source: the Stokes scattering of a pair of nanobeams results in an entangled state between the photon polarization state and the phonon population state in the nanobeams. 2. An arbitrary input state is encoded in the polarization basis of a weak coherent state. 3. A Bell-state measurement (BSM) of the polarization teleports the input state onto the joint mechanical memory state. 4. A short anti-Stokes pulse maps the teleported state $|\psi_{\text{out}}\rangle$ back onto the photon polarization for verification. b) Schematic diagram of the experimental setup. Each nanobeam is placed in one of the arms of a phase-stabilized interferometer, where the polarization in one arm is rotated from horizontal to vertical using a half-wave plate (HWP), before recombining the paths on a polarizing beamsplitter (PBS). The control pulses are filtered out with a narrow linewidth Fabry-Pérot filter. The electro-optic-modulator (EOM) and Pockels cell (PC) allow fast selection of the readout basis in the verification step. Also shown are the half- and quarter-wave plate (QWP) used for the input state preparation, and BSM beamsplitter (BS), PBSs and superconducting nanowire single-photon detectors (SNSPD). (inset) Electron micrograph of one of the optomechanical devices used.

Ω_m from the optical resonance give rise to linearized optomechanical interactions, addressing the Stokes and anti-Stokes transitions of the system, respectively [12, 25].

Our teleportation protocol is based on the proposal described in Ref. [26, 27], which is schematically shown in Fig. 2.1a, while a sketch of the experimental setup can be seen in Fig. 2.1b. Each optomechanical device is placed in one of the arms of an actively phase-stabilized fiber interferometer, see Supplementary Information (SI) section 2.5 for more details. The paths are recombined on a fiber-polarizing beamsplitter such that the photons from the devices are cross polarized. A single blue detuned pulse is injected into the interferometer exciting each nanobeam with the same probability p_b, and the which-path information of the Stokes scattered light is encoded in the polarization state of the optical mode. Light from device A is vertically, while light from device B is horizontally polarized. The joint state of the two mechanical resonators AB and the optical field "o" after recombining, can be described as

$$|\Psi_{\text{EPR}}\rangle \propto |0\rangle_{\text{o}}|00\rangle_{\text{AB}} + \sqrt{p_{\text{b}}}\Big(|H\rangle_{\text{o}}|01\rangle_{\text{AB}} + e^{i\phi}|V\rangle_{\text{o}}|10\rangle_{\text{AB}}\Big) + \mathcal{O}(p_{\text{b}}) \tag{2.1}$$

where $|0\rangle, |1\rangle$ denote the number states containing 0 and 1 excitation, respectively, ϕ can be set by controlling the relative phase of the light coming from each nanobeam using an EOM in arm A of the interferometer, and $p_b \ll 1$ is the Stokes scattering probability set by the blue detuned control pulse energy. Conditioned on the presence of a Stokes-scattered photon, Eq. (2.1) is the Einstein-Podolsky-Rosen (EPR)-state that forms our basic resource for teleportation (as shown in Fig. 2.1a, top left).

After passing a narrow-band (~40 MHz) Fabry-Pérot optical cavity filter to reject the excitation pulse light, the optical part of our EPR-state wave-packet is sent to a (potentially remote) Bell-state measurement apparatus. The arbitrary input qubit state, $\left|\psi_{\text{in}}\right\rangle$, to be teleported is encoded into the polarization of a weak coherent state obtained from a heavily attenuated independent laser (Fig. 2.1a, top right)

$$\left|\psi_{\text{in}}\right\rangle \propto |0\rangle + \alpha\left(\cos\frac{\theta_{\text{in}}}{2}|H\rangle + e^{i\phi_{\text{in}}}\sin\frac{\theta_{\text{in}}}{2}|V\rangle\right) + \mathcal{O}(|\alpha|^2) \tag{2.2}$$

where $|\alpha|$ is the coherent state amplitude, and input angles θ_{in}, ϕ_{in} can be chosen by setting the appropriate angles ϑ_{in}, φ_{in} on the waveplates shown in Fig. 2.1b.

We then implement a polarization based Bell-state measurement (BSM) by combining $\left|\psi_{\text{in}}\right\rangle$ with the optical part of $|\Psi_{\text{EPR}}\rangle$ on a 50/50 beamsplitter (Fig. 2.1a, bottom left) and further analyzing the output polarization using polarizing beamsplitters and single-photon detectors. From Eq. (2.1) and (2.2) we can see that both the conditional EPR state and the photonic state to be teleported are close to the single excitation ideal case, and, by operating in the suitable regime $\sqrt{p_{\text{b}}} \ll |\alpha| \ll 1$, we can beat the classical threshold despite the higher order terms that reduce the teleportation fidelity (see Ref. [26] and SI section 2.5). In this limit a coincidence between polarizations H and V in the BSM projects the state of the mechanical resonators onto

$$\left|\psi_{\text{out}}\right\rangle_{\text{AB}} = \cos\frac{\theta_{\text{in}}}{2}|10\rangle_{\text{AB}} \pm e^{i\phi_{\text{in}}}\sin\frac{\theta_{\text{in}}}{2}|01\rangle_{\text{AB}} \tag{2.3}$$

where the + (−) corresponds to cases where the coincidence occurred on the same (different) output port of the BSM beamsplitter. This event corresponds to the input state $\left|\psi_{\text{in}}\right\rangle$ being teleported onto the single-excitation subspace of the two mechanical resonators. We note that, as also stated in [26], the teleported mechanical state has the probability amplitudes of the two eigenstates exchanged (bit flip) and has a possible π-phase difference (phase flip) compared to the conditional EPR state of Eq (2.1). We take this into account in post-processing.

Finally, we can verify that the teleportation was successful by mapping the joint state of the mechanical resonators back onto an optical polarization state using a red detuned pulse (Fig. 2.1a, bottom right). We can choose an arbitrary measurement basis for the polarization analysis setup by pulsing the EOM in arm A to adjust the relative phase ϕ_{out} between the H and V components, and setting the rotation of a Pockels cell (PC) pulsed at its half-wave-voltage to adjust θ_{out}, the relative amplitude between the H and V components. Conditioned on a successful teleportation event, the fidelity of the teleported state can be measured from the number of readout events with the polarization equal to the one in the input, divided by the total number of readout events (see SI section 2.5 for more).

For the above protocol to work, the nanobeams must meet very stringent criteria. In particular, the emitted photons from each device must be completely indistinguishable in all degrees of freedom but their polarization, which in principle requires the

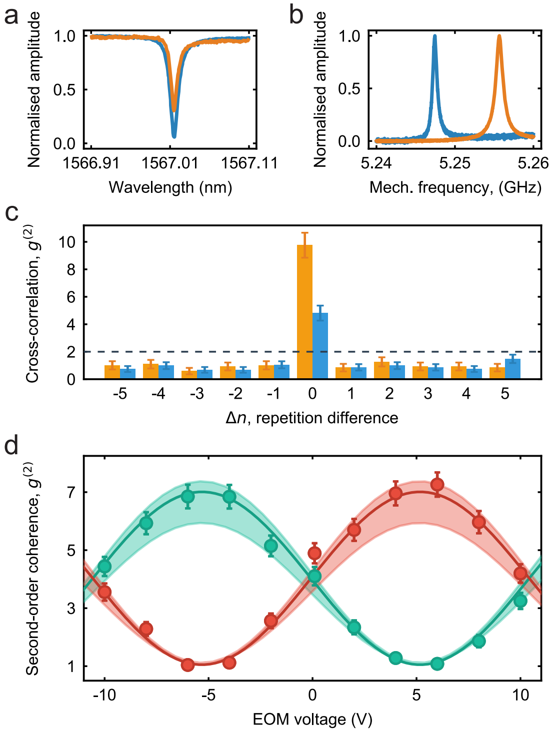

Figure 2.2: **EPR source characterization.** a) Characterization of the optical resonances of device A (blue) and device B (orange) measured in reflection. The devices have a small mismatch of about 0.01 GHz. b) Mechanical spectra of the devices using optomechanical induced transparency (OMIT, see SI section 2.5 for more), device A in blue and device B in orange. The difference in the mechanical frequencies shown here, equal to 8 MHz, is compensated by using a serrodyne-technique to frequency shift the light going to device A to ensure the emitted photons are fully indistinguishable. c) For the same repetition $\Delta n = 0$, the Stokes and anti-Stokes fields of each devices show strong cross-correlations $g^{(2)}_{\mathrm{cc}}$, violating the bound for classical emitters (dashed line), while for different repetitions the detections are fully uncorrelated. Data in blue for device A and in orange for device B. d) Characterization of the entangled states produced by the EPR source: Second-order coherence $g^{(2)}_{i,j}$, in green for $i \neq j$ and in red for $i = j$, with $i, j \in \{D, A\}$ the detected polarization state of the Stokes and anti-Stokes photons respectively (D for diagonal, A for anti-diagonal, see main text), as a function of the phase shift induced in one arm of the interferometer by applying a pulsed voltage to the EOM. The solid line is a sinusoidal fit to guide the eyes. Shaded regions are expected values from simulation, see main text for details. All error bars are one standard deviation.

nanobeams to have identical mechanical and optical resonance frequencies. In order to realize these requirements, we fabricate two chips with around 160 devices each and map their optical resonances, which results in about 40 matching pairs between the two chips in a single fabrication run (see SI section 2.5).

A key challenge in the demonstration of quantum teleportation in our system is the rates at which we can detect threefold coincidences: the first two-photon coincidence to herald a teleportation event in the BSM and a subsequent readout photon to verify its success. While higher optical pulse energies result in higher scattering rates, and therefore higher coincidence rates for the teleportation protocol, they also increase the thermal population of the mechanical systems due to optical absorption heating [28] and lead to a reduced fidelity of the teleported state and its readout [26]. We characterize the thermal population of the mechanical modes as a function of the optical pulse energy using sideband asymmetry [25], and select a few pairs of devices that exhibit the highest scattering rates at a fixed total thermal population. A final selection criteria for the pair is their mechanical lifetime T_1, which should be long enough to store the teleported state until it is retrieved, however not too long, as the repetition rate of the experiment is set by the time required for the mechanical modes to re-thermalize into the ground state (see SI section 2.5 for more details).

2.3. RESULTS

THE characterization of the pair of devices we chose for this work is shown in Fig 2.2. Their resonance wavelengths are $\lambda_{\mathrm{c,A}} = 1567.0154\,\mathrm{nm}$ and $\lambda_{\mathrm{c,B}} = 1567.0153\,\mathrm{nm}$ with a difference in frequency of 0.01 GHz, and with total optical linewidths $\kappa_{\mathrm{A}}/2\pi = 1.47\,\mathrm{GHz}$ and $\kappa_{\mathrm{B}}/2\pi = 1.18\,\mathrm{GHz}$ (intrinsic linewidths $\kappa_{\mathrm{i,A}}/2\pi = 557\,\mathrm{MHz}$ and $\kappa_{\mathrm{i,B}}/2\pi = 264\,\mathrm{MHz}$), see Fig 2.2a. The small residual mismatch in mechanical frequencies $\Omega_{\mathrm{m,A}}/2\pi = 5.2474\,\mathrm{GHz}$ and $\Omega_{\mathrm{m,B}}/2\pi = 5.2555\,\mathrm{GHz}$ of about 8 MHz (Fig 2.2b) can be compensated by frequency shifting the optical excitation pulse in one of the arms, which we realize through serrodyning by driving an EOM with a linear ramp [7]. We measure $T_1^{(A)} = 1.3\,\mu\mathrm{s}$, $T_1^{(B)} = 1.9\,\mu\mathrm{s}$ such that we can operate our experiments with a $20\,\mu\mathrm{s}$ repetition time (see SI section 2.5 for details). We choose to work with scattering probabilities for the Stokes process of 1.2 % (1.3 %) and for the anti-Stokes process of 2.6 % (2.9 %) for device A (B), which correspond to a pulse energy of 22 fJ (18 fJ) and 50 fJ (40 fJ) for device A (B) (see SI sections 2.5 and 2.5 for more details).

We then confirm that the mechanical modes of the nanobeams can individually be prepared close to a single phonon Fock state. In order to accurately predict the $g^{(2)}$ of the mechanical state [25], we measure the cross-correlation between Stokes and anti-Stokes scattered photons: $g^{(2)}_{\mathrm{cc}} = \frac{p_{\mathrm{S}\wedge\mathrm{aS}}(\Delta n)}{p_{\mathrm{S}}\,p_{\mathrm{aS}}}$, with $p_{\mathrm{S}\wedge\mathrm{aS}}(\Delta n)$ the probability to detect both a Stokes (S) and anti-Stokes (aS) scattered photon Δn experimental repetitions apart and p_{S}, p_{aS} the probability to detect individual Stokes and anti-Stokes photons, respectively. The measurement results shown in Fig. 2.2c demonstrate cross-correlation values far above the classical bound of 2 [25] by more than 9 (5) standard deviations for device A (B), proving that we can store our teleported state with little added noise. We also use this measurement to estimate the total thermal population added by the optical pulses. We infer a total thermal excitation of 0.24 ± 0.04 (0.10 ± 0.01) for devices A (B) using a fixed delay between the pulses of 100 ns [29]. Note that the average thermal excitation of the two devices is below $\lesssim 0.24$, the threshold to demonstrate quantum teleportation [26].

Having chosen the most suitable pair of optomechanical devices using the above criteria, we then proceed to characterize their suitability as a conditional EPR source to produce the state $|\Psi_{\mathrm{EPR}}\rangle$ in Eq. (2.1). We test the full conditional EPR source by proving the non separability of the Stokes field with the phononic state in the nanobeams, verifying it with the visibility after readout, similarly to [7]. We first measure the polarization of the optical output state of $|\Psi_{\mathrm{EPR}}\rangle$ in a rotated, diagonal basis. This projects the state of the nanobeams onto

$$|\psi\rangle_{\mathrm{AB}} = \frac{1}{\sqrt{2}}\left(|01\rangle_{\mathrm{AB}} \pm e^{i\phi}|10\rangle_{\mathrm{AB}}\right) \tag{2.4}$$

where the sign ± depends on whether a diagonal $|D\rangle \propto |H\rangle + |V\rangle$ or anti-diagonal $|A\rangle \propto |H\rangle - |V\rangle$ photon was detected. We then map the joint state of the mechanical resonators back onto an optical polarization state, and measure it in the same diagonal basis as a function of ϕ set by the EOM voltage in arm A. This yields the second-order coherence $g^{(2)}_{i,j}(\phi) = \frac{p_{\mathrm{S},i\wedge \mathrm{aS},j}}{p_{\mathrm{S},i}\,p_{\mathrm{aS},j}}$, with $i, j \in \{D, A\}$ the detected polarization state of the Stokes and anti-Stokes photons, respectively. As shown in Fig. 2.2d, the cases where $i = j$ (the same polarization is detected for Stokes and anti-Stokes photons) exhibit opposite correlation compared to the cases where $i \neq j$. We obtain a visibility between Stokes and anti-Stokes pulses of $\mathcal{V} = \frac{g^{(2)}_{i=j} - g^{(2)}_{i\neq j}}{g^{(2)}_{i=j} + g^{(2)}_{i\neq j}} = (74 \pm 3)\,\%$ for the EOM voltage of 6 V, which shows the suitability of the optomechanical system as the EPR source for the teleportation. From this measurement we also calibrate our readout angle ϕ_{out} as a function of the applied EOM voltage. Finally, we compare the measured visibility to a numerical simulation of the entanglement experiment, taking as input only the independently measured thermal occupations and lifetimes of the two nanobeams (see SI section 2.5), detector dark count probability, control pulse leakage and interferometer dephasing. The values expected from simulation are shown as the shaded region in Fig. 2.2d, also taking into account the statistical uncertainties in the measured simulation input parameters (see SI section 2.5 for more details).

Since our scheme is symmetric around a change of π in the phase of the teleported state, we verify our teleportation for input states H, V, $D = (H+V)$ and $L = (H+iV)$, only. To estimate our teleportation fidelity we set our EOM readout phase ϕ_{out} and Pockels cell angle such that the ideal teleported state is mapped to H (V) for cases where the coincidence occurred on the same (different) output port of the BSM beamsplitter. We can then estimate the fidelity of the teleported state as the fraction of correct readout results $F_i = N_{\mathrm{correct,i}}/N_{\mathrm{total,i}}$ with $i \in \{H, V, D, L\}$ (see SI section 2.5). Note that this fidelity estimation includes the fidelity of our readout process, and therefore provides a lower bound to the true teleportation fidelity. After around 100 successful measurement runs for each basis we obtain an average fidelity of $\langle F\rangle = (F_H + F_V + 2(F_D + F_L))/6 = (75.0 \pm 1.7)\,\%$ (see Fig. 2.3), which is significantly above the classical threshold of 2/3 by 4.8 standard deviations. We obtain very similar results even when using the more robust Agresti-Coull interval [30], which is above the threshold by more than four quantiles of a standard normal distribution. The average probability of the measured teleportation event is 4.3×10^{-9} (one event every 1.3 hours).

Using our simulated version of the protocol, which agrees well with the measured fidelities, we can estimate the errors induced by various parts of the protocol. Excluding the readout error from the thermal population added by the red detuned pulse we estimate the teleportation fidelity to be $\langle F\rangle_{\mathrm{sim}} = (77 \pm 1)\,\%$. By replacing the input weak coherent state with a true single photon state, our expected fidelity increases to $(86 \pm 1)\,\%$, with all the other parameters unchanged.

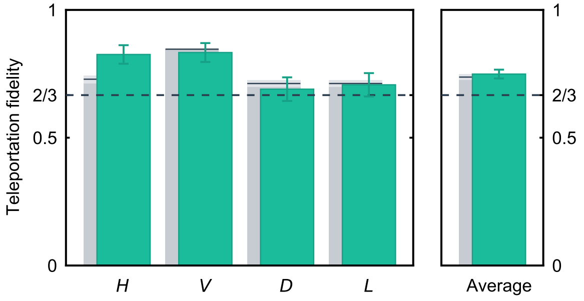

Figure 2.3: **Experimental quantum teleportation.** We measure the fidelity of the teleported state (green bars) for 4 different input basis states: Horizontal (H), Vertical (V), Diagonal (D) and circular left (L). The number of events for each basis, using a 80 ns detection window, are $N_{\text{total}} = 110, 102, 100, 99$ for H, V, D, L, respectively. All error bars are one standard deviation. The dashed line shows the classical limit of 2/3 and the rightmost bar the average $\langle F\rangle = 1/6(F_H + F_V + 2F_D + 2F_L) = (75.0 \pm 1.7)\,\%$. This demonstrates quantum teleportation beating the classical threshold by 4.8 standard deviations. The gray bars are the expected fidelities for each basis from our simulation of the full teleportation protocol, taking only independently measured parameters as input, with the shaded area the statistical confidence interval based on the uncertainty in those parameters and the black line the expected value.

2.4. DISCUSSION

OUR experiment marks the first realization of quantum teleportation of an arbitrary qubit input state onto a dual-rail-encoded long-lived optomechanical quantum memory In contrast to previous experiments, our fully engineered system directly functions as a basic quantum repeater node for a future quantum network with an integrated memory component at telecom wavelengths. Even though the experiment was performed in the lab scale, in our current implementation we already separate the weak coherent state (and the BSM PBS) from the mechanical oscillators by several tens of meters of fiber. A logical further extension to the teleportation protocol will be to demonstrate a full first-level entanglement swapping operation [2, 21], where previously distributed entangled states between distant nanobeams are combined to produce robust dual rail encoded entanglement. In the present form this would require four compatible nanobeam resonators. An attractive alternative would be to use nanobeams with two distinct frequency mechanical modes coupled to a single optical mode, combined with photonic dual rail frequency encoding.

Our experiments also paves the way for transferring arbitrary qubit quantum states onto a mechanical system, which could lead to new tests of fundamental quantum physics [12]. Another exciting possibility for our system is the potential to directly interface with various different quantum systems, such as superconducting microwave circuits, for example [31]. In this context the demonstrated teleportation could function as a quantum state transfer between photonic and microwave qubits. Moreover we show that the system can be easily mode matched to an outside source making it suitable to connect a large variety of optical systems that emit in the near-infrared.

Acknowledgments We would like to thank K. Hammerer and R. Stockill for valuable discussions. This work is supported by the Foundation for Fundamental Research on Matter (FOM) Projectruimte grant (16PR1054), the European Research Council (ERC StG Strong-Q, 676842 and ERC CoG Q-ECHOS, 101001005), and by the Netherlands Organization for Scientific Research (NWO/OCW), as part of the Frontiers of Nanoscience program, as well as through Vidi (680-47-541/994) and Vrij Programma (680-92-18-04) grants. R.B. and T.A. acknowledge funding from the Fundação de Amparo à Pesquisa do Estado de São Paulo (2019/01402-1, 2016/18308-0, 2018/15580-6 and 2018/25339-4) and from the Coordenação de Aperfeiçoamento de Pessoal de Nível Superior (Finance Code 001). B.H. also acknowledges funding from the European Union under a Marie Skłodowska-Curie COFUND fellowship.

Author Contributions: N.F., B.H., A.W., J.L., and S.G. devised and planned the experiment. R.B. and B.H. fabricated the sample and N.F., B.H., R.B. and A.W. built the setup and performed the measurements. B.H. developed the code for the simulations. N.F., B.H., and S.G. analyzed the data and wrote the manuscript with input from all authors. T.P.M.A. and S.G. supervised the project.

Competing Interests: The authors declare no competing interests.

Data Availability: Source data for the plots are available on Zenodo.

Code Availability: The QuTiP code used for the simulations in the Supplementary Information is available on GitHub.

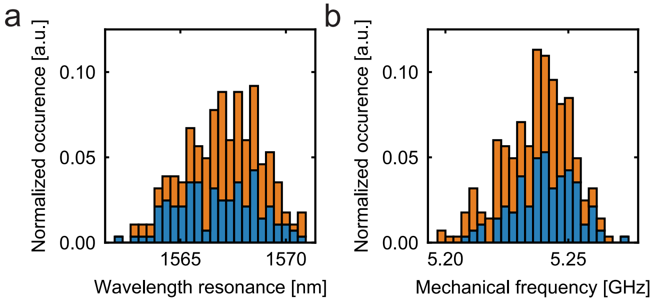

Figure 2.4: a) Histogram of the wavelength of the optical resonances from the two chips used in this experiment. The standard deviation of the distributions are 1.9 nm and 1.7 nm and the distance between the centers of the distributions is 0.5 nm. b) Histogram of the mechanical resonance frequency. In this case, the standard deviation of the distributions are 12 MHz and 14 MHz, respectively, with a distance between the centers of the distributions of 5 MHz. In both figures the chip with device A is in blue, the chip with device B is in orange and they have a total of 121 and 162 working devices respectively.

2.5. SUPPLEMENTARY INFORMATION

DEVICE FABRICATION AND CHARACTERISATION

The nanobeams are fabricated from a silicon-on-onsulator (SOI) wafer with a 250 nm device layer. We pattern our device structure using electron beam lithography, combined with HBr/Ar reactive ion etching. We perform a piranha cleaning step and finally release the device layer with a hydroflouric acid (HF) wet etch. To ensure that the two sets of devices are as identical as possible, we fabricate two lines of devices on the same chip which is then diced into half. The dicing also allows to couple to the devices waveguides with a lensed fiber (as done in [29]).

We proceed to characterize the optical and mechanical resonances of all the devices on the two chips. In order to measure the mechanical resonances, we detect the thermal motion of the nanobeam encoded in the amplitude noise of continuous wave (CW) light reflected from the device, using a fast detector connected to a spectrum analyzer. In Fig. 2.4 it's shown the histogram of the optical (a) and mechanical (b) resonances of the two chips. The total spread of the optical cavity wavelengths is ~1.8 nm, and ~13 MHz for the mechanical center frequencies. The precision of the nanofabrication allows us to match pairs of nanobeams, that have small separation between the optical and mechanical resonances. Out of the approximately 160 devices on each chip we find 40 pairs that have an optical frequency difference of less than the typical linewidth of ~1 GHz. The maximum frequency difference between the mechanical resonances is set by the maximum frequency that we can compensate by using a serrodyne technique (see section 2.5 and main text for more). For the final pair chosen, we also perform a series of OMIT measurements varying the intracavity photon number, as described in [32], from which we then calculate the g_0 of each devices.

MECHANICAL LIFETIME AND OPTICAL HEATING

One of the main source of reduction of the teleportation fidelity is the thermal population of the mechanical mode caused by optical absorption heating (see e.g. [33]). Heating occurs directly, during the optical pulse, which we refer to as *instantaneous heating*. Additionally, as visible from Fig. 2.5a, the thermal population of the mode continues to increase beyond the duration of the optical pulse, which we refer to as *delayed heating*. In our experiment the teleported state is retrieved after 100 ns to minimize delayed heating as much as possible [25, 33]. We intentionally choose a pair with shorter lifetime, such that our experiment allows for a high repetition rate. This is due to the fact that we have to wait for several mechanical lifetimes for the mechanical mode to thermalize back to its ground state. Fixing the delay between Stokes and anti-Stokes pules to 100 ns we show in Fig. 2.6a that two devices with mechanical relaxation times of ≈ 3 μs minimize the required measurement time to violate the non-classical threshold for teleportation.

For our experiment we choose a pair of nanobeams that has the highest scattering probability while still resulting in a thermal occupancy small enough to perform quantum teleportation above the classical threshold. The thermal occupation versus scattering probability for the pair used is shown in Fig. 2.5b. This thermal occupancy reflects the mode heating that occurs during the Stokes optical pulse, the instantaneous heating. To take into account also the effect of the delayed heating, we mimic the real experimental conditions by sending to the devices a red detuned pulse 100 ns before the pulses used to measure the thermal occupation. The first pulse is not for optomechanical interaction, but only for heating, while the second pulse is used to measure the thermal occupancy of the devices. The result can be seen in Fig. 2.5c, where we vary the energy of the pre-heating pulse, and show the corresponding Stokes scattering probability for that pulse energy. The thermal occupation here is given by the total effect of both pre-heating pulse and readout pulses, however the slope allows us to infer the thermal population added by the delayed heating only (see section 2.5 for more details).

With the pulse energy used in this work (22 fJ (18 fJ) and 50 fJ (40 fJ) for device A (B) and for the Stokes and anti-Stokes processes, respectively) we measure a thermal population given by the blue detuned Stokes pulse of 0.053 ± 0.003 (0.036 ± 0.003) and for the red detuned anti-Stokes pulse (including delayed heating from the blue one) 0.135 ± 0.005 (0.066 ± 0.005) for device A (B), respectively.

SIMULATIONS

We numerically simulate the cross-correlation, entanglement and teleportation experiments by keeping track of the total system density matrix throughout the respective protocols. We employ the QuTIP [34, 35] simulation package to describe each subsystem in the Fock-basis up to $N = 3$ excitation. We report that the calculated values differ less than % from the results obtained with higher N and have the advantage of a much shorter calculation time. For the teleportation experiment the total system is described by the state of the mechanical mode of each nanobeam, $\rho_\mathrm{A}, \rho_\mathrm{B}$, the optical mode of the emitted light ρ_H, ρ_V and the optical mode of the input state ρ_H^in, ρ_V^in.

The teleportation model inputs include the input state angles ϑ_in, φ_in, weak coherent state amplitude $|\alpha|$, Stokes scattering probability p_b, anti-Stokes scattering probability p_r and readout angles ϑ_out, ϕ_out. The models for the cross-correlation and entanglement only take a subset of these.

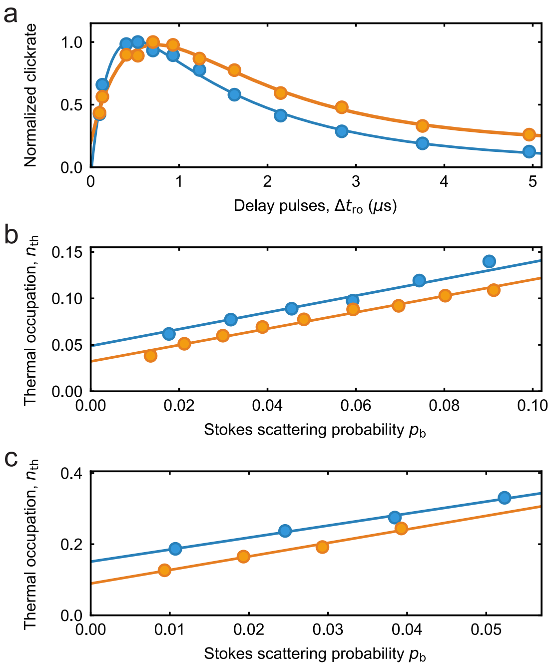

Figure 2.5: a) Normalized clickrates of a red detuned probe pulse delayed by Δt_{ro} from a heating pulse. The pump-probe scheme allows to track the changes in the thermal population (proportional to the clickrates) while sweeping the delay between the pulses [29]. The rise and decay of the thermal population fits well to a double-exponential phenomenological model, from which we obtain the T_1 of the devices (1.3 μs for device A and 1.9 μs for device B). The raise times are 0.2 μs for device A and 0.4 μs for device B. Note that in the teleportation experiment we use a delay between the pulses of 100 ns to limit the thermal heating. b) Thermal occupation n_{th}, estimated from Stokes / anti-Stokes scattering rate asymmetry, as a function of the Stokes scattering rate p_{b}. The thermal occupation is increased due to the instantaneous optical absorption heating that occurs during the optical pulse. Solid line is a linear fit from which we find $n_{\text{th}}^{(A)} = n_0^{(A)} + \zeta_{\text{inst.}}^{(A)} \times p_{\text{b}}^{(A)} = (0.049 \pm 0.004) + (0.91 \pm 0.05) \times p_{\text{b}}^{(A)}$, $n_{\text{th}}^{(B)} = n_0^{(B)} + \zeta_{\text{inst.}}^{(B)} \times p_{\text{b}}^{(B)} = (0.032 \pm 0.002) + (0.88 \pm 0.05) \times p_{\text{b}}^{(B)}$, the uncertainties are from the fit. c) Thermal population due to the combined effect of a heating pulse and the probe pulses. The heating pulse occurs 100 ns prior to the probe pulses. We vary the pulse energy of the heating pulse to assess the contribution of the delayed heating to the total thermal population. Solid line is a linear fit from which we find the slope $\zeta_{\text{delayed}}^{(A)} = 3.4 \pm 0.2$ and $\zeta_{\text{delayed}}^{(B)} = 4.1 \pm 0.2$, the uncertainties are from the fit. The fitted values are used in our simulation to assess optimal optical pulse powers, see SI section 2.5 for details. In all figures the data from device A are in blue and from device B in orange.

We further include a number of imperfections as model inputs:

- The thermal occupation of the mechanical modes, consisting of three parts: First, a steady state thermal occupation of the mechanical mode $n_0^{(A,B)}$, likely caused by heating from the CW leakage from the pulse generation apparatus and heating from the average power sent to the nanobeam that is not efficiently dissipated. Second, the instantaneous heating due to the blue pump pulse. Third, the instantaneous heating due to the red pulse and the effect of the delayed heating from the blue pulse. We model the first two by taking the initial state of the mechanical modes of device A and B as ρ_{A}, ρ_{B} at the beginning of the protocol to be in a thermal state with $n_{\mathrm{th}}^{(\mathrm{A,B})} = n_0^{(\mathrm{A,B})} + \zeta_{\mathrm{inst.}}^{(\mathrm{A,B})} \times p_{\mathrm{b}}^{(\mathrm{A,B})}$, where the $n_0^{(\mathrm{A,B})}$ and $\zeta_{\mathrm{inst.}}^{(\mathrm{A,B})}$ are estimated by the offset and slope of the fit in Fig. 2.5b, respectively. The third part is modeled by coupling the mechanical modes to a thermal bath with $n_{\mathrm{th}}^{(\mathrm{A,B})} = \zeta_{\mathrm{delayed}}^{(\mathrm{A,B})} \times p_{\mathrm{b}}^{(\mathrm{A,B})} + \zeta_{\mathrm{inst.}}^{(\mathrm{A,B})} \times (p_{\mathrm{r}}^{(\mathrm{A,B})} - p_{\mathrm{b}}^{(\mathrm{A,B})})$, where $\zeta_{\mathrm{delayed}}^{(\mathrm{A,B})}$ is estimated by the slope of the fit in Fig. 2.5c. The coupling to the thermal bath is modeled to occur just after the detection of the Stokes-scattered photon and the coupling is implemented by a two-mode-squeezing interaction with an angle $\sqrt{n_{\mathrm{th}}}$ between each mechanical mode and an environmental vacuum mode, and subsequently tracing out the environmental mode. Using the fixed red and blue pulse energies used in the cross-correlation, entanglement and teleportation experiment, we extract the $n_{\mathrm{th}}^{(\mathrm{A,B})}$, used in the simulation shown in Fig. 2.2d and Fig. 2.3, from the measured cross-correlation data (Fig. 2.2c), as it is increased due to the additional average power sent to the device necessary for locking the devices interferometer. The statistical uncertainties of the estimated thermal occupations result in a simulated range of values, shown in the figures as shaded areas.

- The mechanical lifetime of each mechanical mode, modeled as an amplitude damping channel acting on each mechanical mode with loss probability $p_{\mathrm{loss}}^{(\mathrm{A,B})} = e^{-T_1^{(\mathrm{A,B})}/\Delta t_{\mathrm{ro}}}$, where $\Delta t_{\mathrm{ro}} = 100\,\mathrm{ns}$ is the readout delay and $T_1^{(\mathrm{A,B})}$ as found in Fig. 2.5a.

- Detector dark-counts and excitation pulse leakage, resulting in a detector click not originating from either nanobeam or input photon. We take the weighted sum of the density matrix corresponding to a genuine coincidence click from a Stokes scattered photon and input photon, and the density matrix where one of the clicks was produced by a detector dark count or leakage photon. The weights take into account the darkcount and leakage click probability p_{dc}, and the total Stokes photon detection efficiency (device coupling efficiency, detection filter and setup efficiency and single photon detector efficiency), see section 2.5.

- Finite interferometer phase stability, modeled as a dephasing channel with dephasing probability V_{int} on the optical mode H, see Fig. 2.4.

By including optical losses we can also estimate the protocols success probability. We use this simulation to obtain ideal device parameters and power settings to demonstrate teleportation, see Fig. 2.6. Firstly, we determined the optimal T_1 of the devices, a tradeoff between efficiently storing the state and having a higher repetition rate of the experiment. Secondly, we determine the optimal ratio of the weak coherent state (WCS)

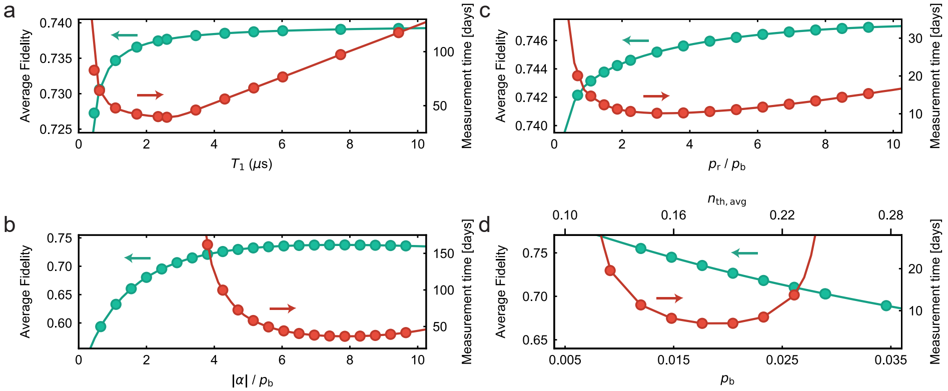

Figure 2.6: Average teleportation fidelity and total measurement time obtained from our simulations. The threshold for the measurement time is the required integration time for the fidelity to be above the threshold of 2/3 by at least 2 standard deviations for each basis. a) Varying the T_1 of the devices we see an optimal point at $T_1 = 3\,\mu$s (for simplicity both devices are assumed to have the same lifetime with a fixed readout delay of 100 ns). b) Varying the ratio between the coherent state amplitude $|\alpha|$ and the Stokes scattering probability p_b, we find an optimal value around 8. c) Varying the ratio between the Stokes and anti-Stokes processes, an optimal point is found for $p_r/p_b = 3$. Here we use the parameters for instantaneous and delayed heating from the asymmetry measurements (Fig. 2.5b,c) and we choose the scattering rates to have a fixed total thermal population due to both pulses. d) Varying the scattering probability p_b, and so the average thermal occupation of the devices $n_{\mathrm{th,aveg}}$. Note a optimal point for $p_b = 0.02$. Also here the parameters for instantaneous and delayed heating from the asymmetry measurements are used. In all four figures the curves are guides to the eye.

amplitude $|\alpha|$ and the scattering probability of the Stokes process p_b, given by the requirement that $|\alpha|$ has to be much larger than p_b for the protocol to work, as well as much smaller than 1 to avoid excessive contribution of the higher order terms of the coherent state. Note that, with a single photon source input, the simulated average fidelity of the teleportation increases to 86 % with the same parameters used in this work. We then calculate the best ratio of scattering probability of the Stokes and anti-Stokes processes, p_r/p_b. Here the optimal point is given by a tradeoff between having a high excitation probability of the devices, given by p_b, and a efficient readout of the mechanical state, given by p_r, while having a constant total thermal occupation. Finally, we sweep the Stokes scattering probability p_b using the optimal settings of the other parameters. This also change the total thermal population, and so the average thermal population of the devices ($n_{\mathrm{th,avg}}$). The optimal point is for p_b high enough to have high rates and with a thermal population low enough to have a average fidelity of the teleported states above the threshold.

OPTICAL SETUP AND EXPERIMENTAL PROCEDURES

A complete schematic of the setup used in the experiment can be found in Fig 2.7. The optical pulses are generated from three separate tunable CW diode lasers, two for the optical control pulses (RED and BLUE lasers), one for the state to be teleported (WCS laser). The lasers are stabilized using a wavelength meter and a frequency beat-lock system (not shown), which allows to have a laser frequency jitter of few MHz. All light sources are filtered with fiber filters of 50 MHz linewidth to reduce the amount of classical laser noise at GHz frequencies. The pulses used in the experiment are generated using two 110 MHz acousto-optic modulators (AOMs) gated via an arbitrary waveform generator (AWG, Agilent 81180A) and are fed into the Mach-Zehnder interferometer through a fiber beamsplitter (BS 1). A variable optical attenuator (VOA) is used to have different pulse powers in the two arms of the interferometer. An electro-optical modulator (EOM) is used for the serrodyne shift (signal from an AWG, Tektronic AFG3152C) and, together with a home-built fiber stretcher, for the phase stabilization of the interferometer (see section 2.5 for more). The pulses are sent to the devices inside the dilution refrigerator via optical circulators, using lensed fibers to couple to the devices' waveguides. The light coming from the devices is recombined on PBS 1 and filtered with two free-space Fabry-Pérot with 40 MHz total linewidth and 17 GHz and 19 GHz free spectral range. The average suppression ratio is 4.0×10^{-11} (104 dB) for the Stokes and 1.5×10^{-11} (108 dB) for the anti-Stokes process, where the difference in suppression arises from higher order modes present in the transmission spectra of the cavities due to a small mode mismatch. Every ~ 6 s the measurements are paused and CW light is injected in the filter cavities to lock them using optical switches (not shown, see [25]). A flip mirror and a free space PBS (PBS 2) are used to align the polarization to the axis of the Pockels cell (PC) using CW light. The signal from the nanobeams, once passed through the PC, is combined in a fiber 50/50 BS with the WCS and then routed to a fiber PBS (PBS 4) with a relative delay in arrival time of 300 ns. An optical switch is used to send optical pulses on a free space setup ($\lambda/2$ and PBS 3) to analyze the polarization in order to align the polarization of the devices and the coherent state. The $\lambda/2$ after the PC is used for the test of the EPR source (Fig. 2.2c) to change the polarization of the photon from the devices from the alignment settings (H, V) to the measurement setting (D, A).

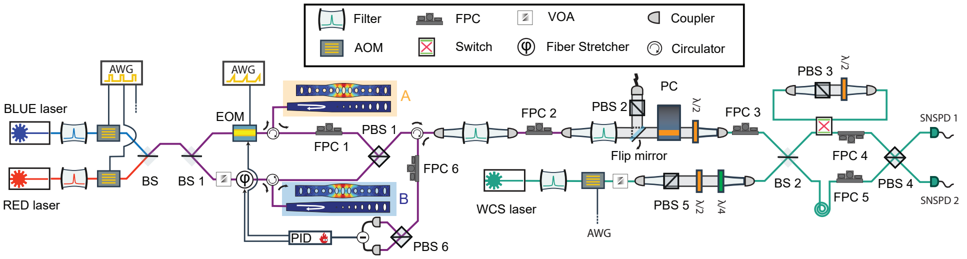

Figure 2.7: Detailed schematics of the setup (see the text for more details). AOM are the acousto-optic modulators, AWG the arbitrary waveform generators, EOM the electrooptic modulator, VOA the variable optical attenuator, BS the 50/50 beamsplitters, PBS the polarization beamsplitters, PC the Pockels cell, FPC the fiber polarization controller, $\lambda/2$ half-wave plate, $\lambda/4$ quarter-wave plate and SNSPD the superconducting nanowire single-photon detectors. WCS is the weak coherent state to be teleported. Note that PBS 2, 3 and 5 are free space PBS while the others are fiber PBS.

We use fiber polarization controllers (FPC) to:

- Maximize the transmission through the various PBSs along the setup (FPC 1 and othera that are not shown).
- Align the polarization to the axis of the PC using a reference PBS (PBS 2 and FPC 2).
- Align the polarization of the light from the device A and from the WCS with respect to a reference free-space PBS (PBS 3 and FPC 3), in both the H and D polarization.
- Align the polarization of the light from the device A and from the WCS with respect to the BSM PBS (PBS 4 and FPC 4, 5).
- Ensure that the relative phase between the devices on which we lock the interferometer is constant during the whole experiment (PBS 6 and FPC 6, see section 2.5 for more).

Note that the polarization of device B is always orthogonal since the paths are recombined on PBS 1. In particular the alignment on the free-space PBS 3 is fundamental to determine the relative phase between the state of the devices and the teleported one, in order to properly map the Poincaré spheres of both states.

To guarantee that the EPR state is the desired maximally entangled state, we assure that the measured scattering rates from the Stokes process of the devices are equal. Since for both devices the collection efficiency of the scattered photons and the thermal populations are similar, matching the measured rates means matching p_{b}. Note that the readout probability will be, in theory, identical for both devices while the scattering rates from the anti-Stokes process are not matched since they are sensitive to the (different) thermal occupancy of the devices. From the results of Fig. 2.6, we also calibrate the clickrates from the WCS to be 6.8 times the clickrates from the Stokes process of the single device.

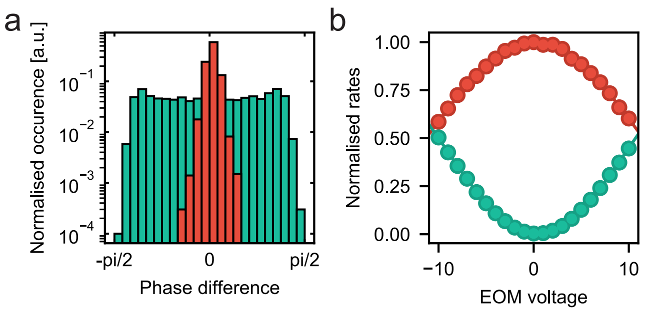

Figure 2.8: a) Occurrence histogram of the difference of the phase in the interferometer unlocked (green) and locked (red) configuration, for each dataset we sample the phase every second for approximately an hour. For the latter case we obtain a FWHM $\approx \pi/40$. b) Normalized count rates from the first order interference of a laser on resonance with the cavities and the detection filters for detector 1 (red) and detector 2 (green). Sweeping the EOM voltage in one of the interferometer arm shows the interference pattern. Due to the limited voltage range only half a period is visible. The interferometer visibility in this case is $V_{\text{int}} \approx 99.3\%$. Error bars are one standard deviation and are too small to be seen.

The total measurement time of the experiment in the main text, Fig. 2.3, was 35 days. To ensure the stability of the setup and to exclude data recorded during a faulty state of the setup, we check the parameters of the setup (the laser locking, the filter detection locking among others) every five seconds and we measure the polarization state and the clickrates from the devices and the WCS every hour. We further align the polarization as described above every 2 days, to keep the deviation in polarization and clickrates to a few % and the decrease in visibility of the interferometer in the fixed EOM voltage by a few % (see section 2.5 for more). We also align the free space optics every two weeks when the efficiency of the setup (measured via the clickrates at a fixed pulse energy) reduces by a few %. The polarization check, which is performed every hour, requires approximately 1/6 of the total measurement time. This time together with the time in which the detection filters are re-locked (1/6, approximately 1 second every 6 seconds), brings to the total effective integration time to 23 days.

The average collection efficiency of the scattering photon from the devices (including the coupling from the fiber to the optical waveguide, equal to 46 % (55 %)) is 11 % (13 %) for line A (B). The detectors dark-counts and residual leakage of the pump pulses are 5.9×10^{-6} (4.9×10^{-6}) for the Stokes process with pulse energy of 22 fJ (18 fJ) and 6.7×10^{-6} (5.6×10^{-6}) for the anti-Stokes process with pulse energy 50 fJ (40 fJ) for device A (B). We use for the simulation the average value, $p_{\text{dc}} = 6 \times 10^{-6}$. Note that the bare dark-counts from the SNSPDs are sub-Hz (0.1 Hz).

PHASE LOCKING

In order to have a well-defined phase relation between the two nanobeams, so to have a stable ϕ in the EPR state (see Eq. 2.1), we need a phase stabilized interferometer, which has a free-spectral range (FSR) of more than 6 GHz. The red detuned locking pulse, delayed by 1 μs in time with respect to the measurement pulse, is reflected by the first cavity, split by a fiber PBS (PBS 6) and measured on a balanced photodiode. A PID program on a RedPitaya [36] is used to actively lock the interferometer during the experiment. The locking feedback has a bandwidth of ~ 3.8 MHz and two output signals, see Fig. 2.7: one is applied to the fiber stretcher that is low-passed by a pre-amplifier (30 kHz), while the other output is applied to the EOM in the arm of device A and its feedback is ultimately limited by the repetition rate of the experiment (100 kHz). In this way, we can compensate the high frequency components of the error signal (mainly given by the vibration picked up by the fiber in the dilution refrigerator induced by the pulsetube unit).

We directly estimate the phase stability from the normalized lock pulse amplitude, shown in Fig. 2.8a, obtaining a full-width at half maximum FWHM $\approx \pi/40$. We can also measure the long term phase stability using the average interferometer visibility during the whole measurement ($V_{\text{int}} \sim 99.3\%$, ultimately also limited by the polarization alignment). A typical measure of the first order interference from the laser light reflected from the devices is plotted in Fig. 2.8b, from which we can estimate a phase stability of $\pi/25$ [37].

Note that the locking light and the signal light have two different paths, so we need to reference the relative phase between the devices in order to fix the EOM calibration done with the test of the EPR source (shown in Fig. 2.2c). To do this we use a FPC (FPC 6) to maximize the interference visibility for a chosen EOM voltage, fixing the phase difference between the devices for every run of the experiment. Polarization drifts changes the point of maximum visibility over time. This because a change in polarisation after the PBS 1 changes the phase at which we lock the interferometer and so changes the relative phase between device A and device B. So, in order to have a small reduction in interferometer visibility for the chosen EOM voltage, the process of alignment is repeated every two days.

TIME EVOLUTION OF THE ENTANGLED STATE

To ensure that the quantum state teleported onto the joint mechanical state of the nanobeams maintains its coherence before the readout, we perform a characterization of the entangled state produced by the EPR source by sweeping the delay between the blue and red detuned pulses with a fixed offset in the EOM voltage, as previously done in [7]. The result is shown in Fig 2.9. We find a coherence time of the entangled state of 500 ns, much longer than the readout delay $\Delta t_{\text{ro}} = 100$ ns. Note that this value is smaller than the measured T_1 of the single devices, which is a combined effect of additional delayed optical heating and dephasing. We compare the measured data to the simulation, as done in Fig 2.2d, including the expected increase in thermal population due the the delayed absorption, using the fitted value of Fig 2.5b. We find that the reduction in coherence time can be explained by the delayed heating for short delays (up to ≈ 500 ns). For longer delay the small discrepancies can be caused by the imperfection in the simple model of the delayed heating.

HONG-OU-MANDEL INTERFERENCE

In order to further verify that the input photons from $|\psi_{\text{in}}\rangle$ and the photons scattered from the nanobeams in $|\Psi_{\text{EPR}}\rangle$ are mode matched, as required for a successful BSM, we perform a Hong-Ou-Mandel (HOM) interference experiment [38]. We report in Fig 2.10 the result for different repetition Δn of the second order correlation of the optical field from the device A and the WCS (in red) and device B and the WCS (in green), for the

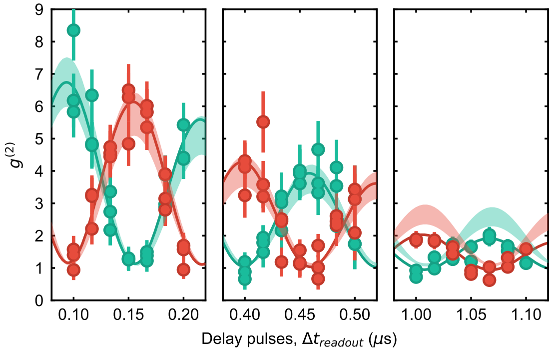

Figure 2.9: Second-order coherence $g^{(2)}_{i,j}$ for $i \neq j$ (green) and $i = j$ (red), with $i, j \in \{D, A\}$ the detected polarization state of the Stokes and anti-Stokes photons respectively (both occurring in the same repetition), as a function of the delay between the blue and red detuned pulses. The phase shift is induced by the difference in mechanical frequency of the two oscillators. We measure a decay time of 500 ns. The shaded regions are the expected values from simulation, including the statistical uncertainties of the input parameters (see the text and section 2.5 for more details). The solid lines are a fit to help guide the eye. All error bars are one standard deviation.

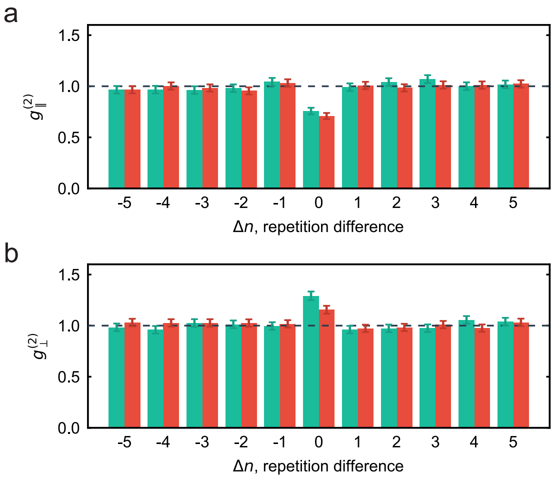

Figure 2.10: Two-photon quantum interference of nanobeam and input state photons. a) Second order correlation of the optical field from device A and the WCS (red) and device B and the WCS (green) for parallel polarization. A clear dip is visible for the same repetition. b) Same as a) for orthogonal polarisation. In this case a peak is visible for the same repetition. From this two dataset we can obtain a visibility of $V_{\text{HOM}} = (38 \pm 3)\,\%$ for device A and $V_{\text{HOM}} = (42 \pm 3)\,\%$ for device B. All error bars are one standard deviation.

case of interfering signals ($g^{(2)}_{\parallel}$) and not interfering signals ($g^{(2)}_{\perp}$). The coincidence rate from the not interfering signals (orthogonal polarization) is used for normalization of the HOM. The measured interference visibility of $V_{\mathrm{HOM}} = \frac{g^{(2)}_{\parallel}}{g^{(2)}_{\parallel}+g^{(2)}_{\perp}}$ is $(38 \pm 3)\,\%$ for device A and $(42 \pm 3)\,\%$ for device B. This results are consistent with HOM interference of ideal indistinguishable photons in a weak thermal and coherent state, for which a visibility of $2/5 = 40\%$ is expected. For different repetitions we find an average of $g^{(2)} = 0.986 \pm 0.01$ (device A) and $g^{(2)} = 1.007 \pm 0.017$ (device B).

TELEPORTATION TRUTH TABLE

We report the truth table used for the post-processing analysis, Tab. 2.1. From Fig. 2.1a (bottom left) we define the BSM detectors as H_{early}, V_{early} and V_{late}, H_{late}, respectively from the leftmost to the rightmost. A successful teleportation event is a double click with opposite polarization. Note that, as visible in Fig. 2.7, this choice of name is given by the fact that in the experiment only two SNSPDs were used so that "early" or "late" refers to the output of the BSM BS (BS 2). For this reason the SNSPD 1 correspond to H_{early}, V_{late} and SNSPD 2 to V_{early}, H_{late}. With the readout pulse, we verify the polarization of the teleported state choosing the appropriate measurement basis for the polarization analysis setup. We then compare the output of the measurement to the truth table to asses if the readout is correct.

Input polarization	**Teleportation event**			
	$H_{\mathrm{early}}, V_{\mathrm{early}}$	$H_{\mathrm{early}}, V_{\mathrm{late}}$	$H_{\mathrm{late}}, V_{\mathrm{early}}$	$H_{\mathrm{late}}, V_{\mathrm{late}}$
H	V	V	V	V
V	H	H	H	H
D	H	V	V	H
L	V	H	H	V

Table 2.1: Truth table used in the post-processing analysis of the data.

2.6. APPENDIX

In this appendix we report some facts and some *a posteriori* consideration on the experiment reported in this chapter. The idea is to give insights on the challenges encountered on the path to acquire the final dataset.

- The major challenge in this experiment is to have high enough click rates and still low enough thermal occupancy to violate the classical threshold. For this reason very high optical Q cavities are necessary. We report, that despite the precision in the nanofabrication, 29 total pairs of chip were made and tested over the course of 5 months to have the final devices. We also report that 7 total cooldown were done in this period of time, each with a different pair of chips to test.

- Despite the quite high number of pairs of devices with optical resonances within one FWHM (thanks to the high number of devices available in one chip and the "birthday paradox" [7]), having both devices with all the important metrics in the desired value range is a challenge. In particular we report that out of the 160 devices per chip we have 40 pairs where the difference in optical frequency is smaller than the typical FWHM (~ 1 GHz). Out of these ones, only 9 pairs have a thermal occupancy from the optical heating small enough to be suitable candidates for the experiment. Only 5 pairs have lifetime higher than 1 μs and a difference in mechanical frequency that is small enough to compensate with the serrodyne (~ 20 MHz).

- After the pairs of nanobeam were found, we spend other 3 months to complete and improve the experimental setup, fully characterize two pairs to choose the best one and then determine the optimize parameters of the experiment to minimize the integration time (with a high enough visibility to pass the classical threshold). With the pair chosen for the experiment we measured 3 datasets over the course of 3 months. The data reported are only from the last dataset.

- In the last dataset we used the free space part (PBS 3 in 2.7) to align both *H* and *D* polarization of device A and WCS, and FPC 6 (from the same figure) to stabilize the relative phase between device A and B. These two part are fundamental since the two Block sphere need to be aligned (device A and B, and WCS).

  A fiber-based PBS only allows to align one axis (*H* for example), a re-alignment using a FPC can change the polarization in the equator (*D A*, *L R*) in a uncontrolled way and even a small piece of fiber can change randomly the polarization. For these reasons, the free space part is necessary to align not only to a single axis (i.e. *H*) but also to a second one (i.e. *D*) to avoid -uncontrolled- polarization differences in the several integration runs of teleportation between the Block sphere of the state to be teleported and one of the nanobeams.

  To lock the interferometer of the devices we use light reflected from the first filter. However, maximizing the interference signal on the detectors after PBS 6 is not enough. Since FPC 6 change the polarization on the equator in a uncontrolled way, it would effectively result in a change in the phase between runs of integration. One could think that the *H* and *V* light from the devices is rotated to, for example, *D* and *A* to interfere in PBS 6 and create the signal to lock the interferometer. But in reality is rotated to a mix of *D*, *L* and *A*, *R* that changes between runs of integration. The change in the phase offset is measurable from the entanglement curves shown in Fig. 2.2. Instead of using the entanglement measure to calibrate for every runs this offset, which will require too much time, we use FPC 6 to maximize the interferometer visibility at a (fixed) EOM voltage. Doing so, we fix the phase offset measured in the entanglement and so the teleportation settings of the EOM. Notably, having a VOA in the interferometer can be a problem. Since the attenuation is done varying the length of a light-absorbing material, this also changes the optical length and so the phase acquired in the interferometer. Using the same settings every time for the VOA attenuation (both in the alignement and in the integration) is important to not have a random phase offset for every runs.

- Since every set of data for each polarization have a long integration time (∼ 1 week), having a reliable tool to predict the visibility of the teleportation is fundamental to choose the correct parameters of the experiment. The simulation reported in 2.5 were extensively used to understand which pair to choose and have a good estimation of the parameters to be optimize using the result of calibration measurements (like the entanglement reported in Fig. 2.2).

REFERENCES

[1] C. H. Bennett, G. Brassard, C. Crépeau, R. Jozsa, A. Peres, and W. K. Wootters, Teleporting an unknown quantum state via dual classical and Einstein-Podolsky-Rosen channels, Phys. Rev. Lett. **70**, 1895 (1993).

[2] N. Sangouard, C. Simon, H. de Riedmatten, and N. Gisin, Quantum repeaters based on atomic ensembles and linear optics, Rev. Mod. Phys. **83**, 33 (2011).

[3] R. Raussendorf and H. J. Briegel, A one-way quantum computer, Phys. Rev. Lett. **86**, 5188 (2001).

[4] S. Barz, E. Kashefi, A. Broadbent, J. F. Fitzsimons, A. Zeilinger, and P. Walther, Demonstration of blind quantum computing, Science **335**, 303 (2012).

[5] J. Chan, T. P. M. Alegre, A. H. Safavi-Naeini, J. T. Hill, A. Krause, S. Gröblacher, M. Aspelmeyer, and O. Painter, Laser cooling of a nanomechanical oscillator into its quantum ground state, Nature **478**, 89 (2011).

[6] H. J. Kimble, The quantum internet, Nature **453**, 1023 (2008).

[7] R. Riedinger, A. Wallucks, I. Marinković, C. Löschnauer, M. Aspelmeyer, S. Hong, and S. Gröblacher, Remote quantum entanglement between two micromechanical oscillators, Nature **556**, 473 (2018).

[8] A. Wallucks, I. Marinković, B. Hensen, R. Stockill, and S. Gröblacher, A quantum memory at telecom wavelengths, Nat. Phys. **16**, 772 (2020).

[9] M. Forsch, R. Stockill, A. Wallucks, I. Marinković, C. Gärtner, R. A. Norte, F. van Otten, A. Fiore, K. Srinivasan, and S. Gröblacher, Microwave-to-optics conversion using a mechanical oscillator in its quantum groundstate, Nature Phys. **16**, 69 (2020).

[10] W. Jiang, C. J. Sarabalis, Y. D. Dahmani, R. N. Patel, F. M. Mayor, T. P. McKenna, R. Van Laer, and A. H. Safavi-Naeini, Efficient bidirectional piezo-optomechanical transduction between microwave and optical frequency, Nature Commun. **11**, 1166 (2020).

[11] M. Mirhosseini, A. Sipahigil, M. Kalaee, and O. Painter, Superconducting qubit to optical photon transduction, Nature **588**, 599 (2020).

[12] M. Aspelmeyer, T. J. Kippenberg, and F. Marquardt, Cavity optomechanics, Rev. Mod. Phys. **86**, 1391 (2014).

[13] H.-J. Briegel, W. Dür, J. I. Cirac, and P. Zoller, Quantum repeaters: the role of imperfect local operations in quantum communication, Phys. Rev. Lett. **81**, 5932 (1998).

[14] D. Bouwmeester, J.-W. Pan, K. Mattle, M. Eibl, H. Weinfurter, and A. Zeilinger, Experimental quantum teleportation, Nature **390**, 575 (1997).

[15] A. Furusawa, J. L. Sørensen, S. L. Braunstein, C. A. Fuchs, H. J. Kimble, and E. S. Polzik, Unconditional Quantum Teleportation, Science **282**, 706 (1998).

[16] X.-S. Ma, T. Herbst, T. Scheidl, D. Wang, S. Kropatschek, W. Naylor, B. Wittmann, A. Mech, J. Kofler, E. Anisimova, V. Makarov, T. Jennewein, R. Ursin, and A. Zeilinger, Quantum teleportation over 143 kilometres using active feed-forward, Nature **489**, 269 (2012).

[17] R. Valivarthi, M. G. Puigibert, Q. Zhou, G. H. Aguilar, V. B. Verma, F. Marsili, M. D. Shaw, S. W. Nam, D. Oblak, and W. Tittel, Quantum teleportation across a metropolitan fibre network, Nature Photon. **10**, 676 (2016).

[18] S. Olmschenk, D. N. Matsukevich, P. Maunz, D. Hayes, L.-M. Duan, and C. Monroe, Quantum teleportation between distant matter qubits, Science **323**, 486 (2009).

[19] W. Pfaff, B. J. Hensen, H. Bernien, S. B. van Dam, M. S. Blok, T. H. Taminiau, M. J. Tiggelman, R. N. Schouten, M. Markham, D. J. Twitchen, and R. Hanson, Unconditional quantum teleportation between distant solid-state quantum bits, Science **345**, 532 (2014).

[20] P.-Y. Hou, Y.-Y. Huang, X.-X. Yuan, X.-Y. Chang, C. Zu, L. He, and L.-M. Duan, Quantum teleportation from light beams to vibrational states of a macroscopic diamond, Nature Commun. **7**, 11736 (2016).

[21] L. Jiang, J. M. Taylor, and M. D. Lukin, Fast and robust approach to long-distance quantum communication with atomic ensembles, Phys. Rev. A **76**, 012301 (2007).

[22] L. M. Duan, M. D. Lukin, J. I. Cirac, and P. Zoller, Long-distance quantum communication with atomic ensembles and linear optics., Nature **414**, 413 (2001).

[23] A. Bassi, K. Lochan, S. Satin, T. P. Singh, and H. Ulbricht, Models of wave-function collapse, underlying theories, and experimental tests, Rev. Mod. Phys. **85**, 471 (2013).

[24] F. Fröwis, P. Sekatski, W. Dür, N. Gisin, and N. Sangouard, Macroscopic quantum states: Measures, fragility, and implementations, Rev. Mod. Phys. **90**, 025004 (2018).

[25] R. Riedinger, S. Hong, R. A. Norte, J. A. Slater, J. Shang, A. G. Krause, V. Anant, M. Aspelmeyer, and S. Gröblacher, Non-classical correlations between single photons and phonons from a mechanical oscillator, Nature **530**, 313 (2016).

[26] J. Li, A. Wallucks, R. Benevides, N. Fiaschi, B. Hensen, T. P. M. Alegre, and S. Gröblacher, Proposal for optomechanical teleportation, Phys. Rev. A **102**, 032402 (2020).

[27] S. Pautrel, Z. Denis, J. Bon, A. Borne, and I. Favero, An optomechanical discrete variable quantum teleportation scheme, Phys. Rev. A **101**, 063820 (2020).

[28] S. M. Meenehan, J. D. Cohen, S. Gröblacher, J. T. Hill, A. H. Safavi-Naeini, M. Aspelmeyer, and O. Painter, Silicon optomechanical crystal resonator at millikelvin temperatures, Phys. Rev. A **90**, 011803 (2014).

[29] S. Hong, R. Riedinger, I. Marinković, A. Wallucks, S. G. Hofer, R. A. Norte, M. Aspelmeyer, and S. Gröblacher, Hanbury Brown and Twiss interferometry of single phonons from an optomechanical resonator, Science **358**, 203 (2017).

[30] L. D. Brown, T. T. Cai, and A. DasGupta, Interval Estimation for a Binomial Proportion, Stat. Sci. **16**, 101 (2001).

[31] Y. Chu and S. Gröblacher, A perspective on hybrid quantum opto- and electromechanical systems, Appl. Phys. Lett. **117**, 150503 (2020).

[32] A. H. Safavi-Naeini, T. P. M. Alegre, J. Chan, M. Eichenfield, M. Winger, Q. Lin, J. T. Hill, D. Chang, and O. Painter, Electromagnetically induced transparency and slow light with optomechanics, Nature **472**, 69 (2011).

[33] S. M. Meenehan, J. D. Cohen, G. S. MacCabe, F. Marsili, M. D. Shaw, and O. Painter, Pulsed Excitation Dynamics of an Optomechanical Crystal Resonator near Its Quantum Ground State of Motion, Phys. Rev. X **5**, 041002 (2015).

[34] J. R. Johansson, P. D. Nation, and F. Nori, Qutip: An open-source python framework for the dynamics of open quantum systems, Comp. Phys. Comm. **183**, 1760 (2012).

[35] J. R. Johansson, P. D. Nation, and F. Nori, Qutip 2: A python framework for the dynamics of open quantum systems, Comp. Phys. Comm. **184**, 1234 (2013).

[36] M. A. Luda, M. Drechsler, C. T. Schmiegelow, and J. Codnia, Compact embedded device for lock-in measurements and experiment active control, Rev. Scien. Instr. **90**, 023106 (2019).

[37] J. Minář, H. de Riedmatten, C. Simon, H. Zbinden, and N. Gisin, Phase-noise measurements in long-fiber interferometers for quantum-repeater applications, Phys. Rev. A **77**, 052325 (2008).

[38] C. K. Hong, Z. Y. Ou, and L. Mandel, Measurement of subpicosecond time intervals between two photons by interference, Phys. Rev. Lett. **59**, 2044 (1987).

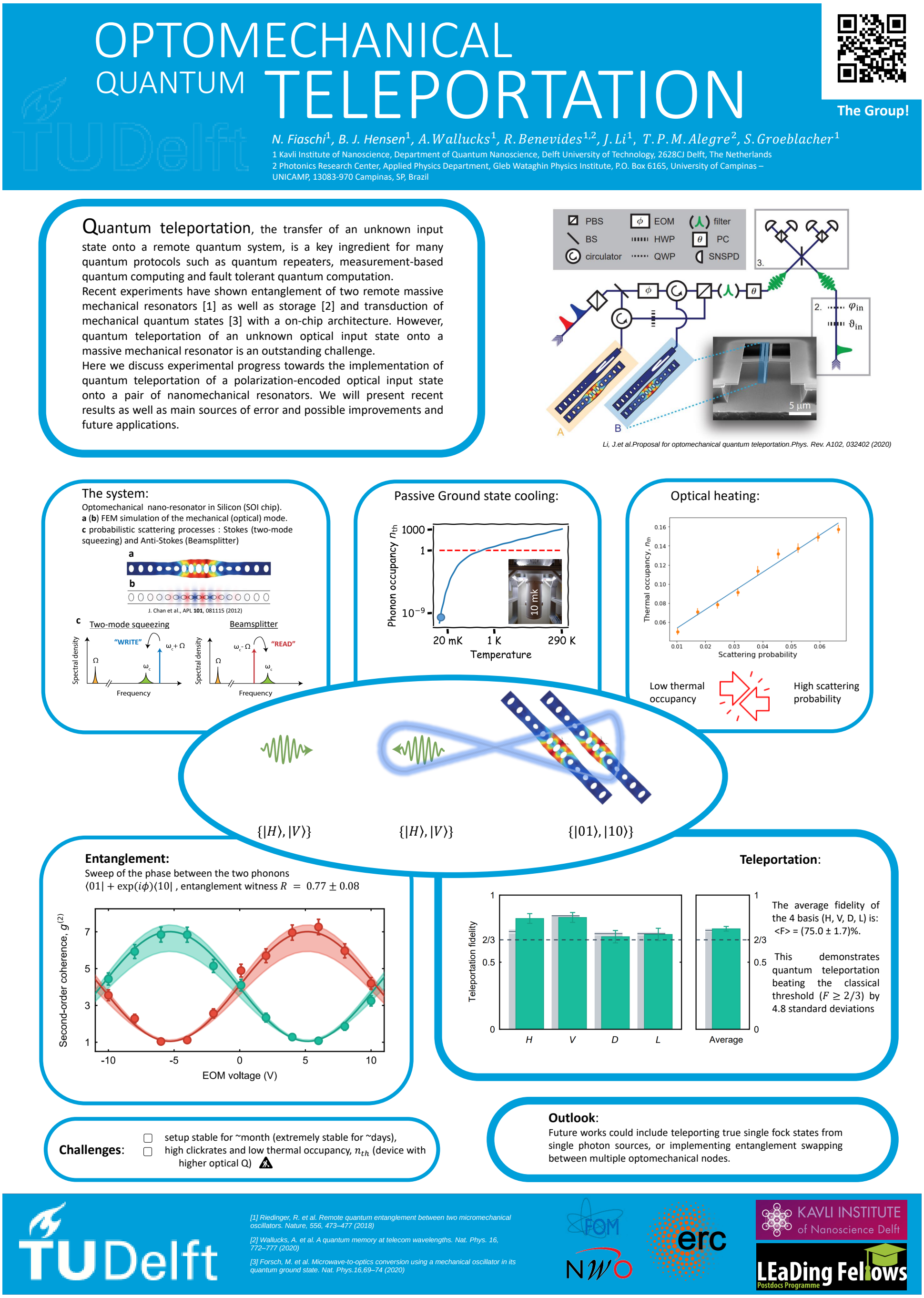

OPTOMECHANICAL QUANTUM TELEPORTATION

The Group!

N. Fiaschi[1], B. J. Hensen[1], A. Wallucks[1], R. Benevides[1,2], J. Li[1], T. P. M. Alegre[2], S. Groeblacher[1]
1 Kavli Institute of Nanoscience, Department of Quantum Nanoscience, Delft University of Technology, 2628CJ Delft, The Netherlands
2 Photonics Research Center, Applied Physics Department, Gleb Wataghin Physics Institute, P.O. Box 6165, University of Campinas – UNICAMP, 13083-970 Campinas, SP, Brazil

Quantum teleportation, the transfer of an unknown input state onto a remote quantum system, is a key ingredient for many quantum protocols such as quantum repeaters, measurement-based quantum computing and fault tolerant quantum computation.
Recent experiments have shown entanglement of two remote massive mechanical resonators [1] as well as storage [2] and transduction of mechanical quantum states [3] with a on-chip architecture. However, quantum teleportation of an unknown optical input state onto a massive mechanical resonator is an outstanding challenge.
Here we discuss experimental progress towards the implementation of quantum teleportation of a polarization-encoded optical input state onto a pair of nanomechanical resonators. We will present recent results as well as main sources of error and possible improvements and future applications.

Li, J.et al.Proposal for optomechanical quantum teleportation.Phys. Rev. A102, 032402 (2020)

The system:

Optomechanical nano-resonator in Silicon (SOI chip).
a (**b**) FEM simulation of the mechanical (optical) mode.
c probabilistic scattering processes : Stokes (two-mode squeezing) and Anti-Stokes (Beamsplitter)

J. Chan et al., APL **101**, 081115 (2012)

Passive Ground state cooling:

Optical heating:

Low thermal occupancy

High scattering probability

Entanglement:

Sweep of the phase between the two phonons
$\langle 01| + \exp(i\phi)\langle 10|$, entanglement witness $R = 0.77 \pm 0.08$

Teleportation:

The average fidelity of the 4 basis (H, V, D, L) is: <F> = (75.0 ± 1.7)%.

This demonstrates quantum teleportation beating the classical threshold ($F \geq 2/3$) by 4.8 standard deviations

Challenges:

☐ setup stable for ~month (extremely stable for ~days),
☐ high clickrates and low thermal occupancy, n_{th} (device with higher optical Q) ⚠

Outlook:

Future works could include teleporting true single fock states from single photon sources, or implementing entanglement swapping between multiple optomechanical nodes.

[1] Riedinger, R. et al. Remote quantum entanglement between two micromechanical oscillators. Nature, 556, 473–477 (2018)
[2] Wallucks, A. et al. A quantum memory at telecom wavelengths. Nat. Phys. 16, 772–777 (2020)
[3] Forsch, M. et al. Microwave-to-optics conversion using a mechanical oscillator in its quantum ground state. Nat. Phys.16,69–74 (2020)

Poster for the paper Niccolò Fiaschi*, Bas Hensen*, Andreas Wallucks, Rodrigo Benevides, Jie Li, Thiago P. Mayer Alegre and Simon Gröblacher, *Optomechanical quantum teleportation*, Nat. Photon. 15, 817–821 (2021).

3

NON-CLASSICAL MECHANICAL STATES GUIDED IN A PHONONIC WAVEGUIDE

Amirparsa ZIVARI, Robert STOCKILL, Niccolò FIASCHI, Simon GRÖBLACHER

The ability to create, manipulate and detect non-classical states of light has been key for many recent achievements in quantum physics and for developing quantum technologies. Achieving the same level of control over phonons, the quanta of vibrations, could have a similar impact, in particular on the fields of quantum sensing and quantum information processing. Here we present a crucial step towards this level of control and realize a single-mode waveguide for individual phonons in a suspended silicon micro-structure. We use a cavity-waveguide architecture, where the cavity is used as a source and detector for the mechanical excitations, while the waveguide has a free standing end in order to reflect the phonons. This enables us to observe multiple round-trips of the phonons between the source and the reflector. The long mechanical lifetime of almost 100 µs *demonstrates the possibility of nearly lossless transmission of single phonons over, in principle, tens of centimeters. Our experiment demonstrates full on-chip control over traveling single phonons strongly confined in the directions transverse to the propagation axis, potentially enabling a time-encoded multimode quantum memory at telecom wavelength and advanced quantum acoustics experiments.*

Parts of this chapter have been published in Amirparsa Zivari, Robert Stockill, Niccolò Fiaschi and Simon Gröblacher, *Non-classical mechanical states guided in a phononic waveguide,* Nat. Phys. 18, 789–793 (2022).

3.1. INTRODUCTION

CREATING and detecting quantum states of mechanical motion open up new possibilities for quantum information processing, quantum sensing and probing the foundations of quantum physics [1]. In particular within the field of quantum optomechanics many remarkable milestones have been reached over the past years: from showing the ability to realize the quantum ground state of a mechanical oscillator and single phonon control [2], unambiguous demonstration of the quantum nature of phonons through the creation of entangled states [3–5] and a Bell test [6], to realizing a long coherence-time quantum memory [7]. Furthermore, the field has shown the potential to enable crucial applications in connecting quantum computers, and transfer information between them [8–11]. While these applications usually rely on highly confined phononic states (with a typical mode volume on the order of the wavelength), the use of traveling phonons promises the ability to create on-chip architectures for classical and quantum information [12], with the potential to add completely new capabilities compared to their optical counterparts. The exciting prospects in this new field of quantum acoustics are enabled by the orders of magnitude slower propagation speed compared to photons, the inherently low loss, their extremely low energy and the small mode volume compared to GHz-frequency photons. These features make phonons ideally suited for direct manipulation on a chip with wavelength sized components, while the ability to realize significant time-delays in a short distance makes this type of system an ideal platform for on-chip operations [13]. Furthermore, phonons have also demonstrated their unique capability to efficiently couple and even mediate the interaction between various quantum systems [14], such as superconducting qubits [15], defect centers in solids [16], and quantum dots [17, 18]. Using mechanical excitations as low-loss carriers of quantum information will allow for the construction of two-dimensional architectures and large-scale phononic quantum networks [19].

While the creation of non-classical mechanical states have been demonstrated in multiple physical systems [20], only a very limited number of experiments have been able to realize propagating modes in the quantum regime, all based on surface acoustic waves [15, 21, 22]. This approach comes with its own limitations and challenges, such as relatively short lifetimes, losses due to beam steering and diffraction, typically only bi-directional emission and no full confinement of the mode except in resonators. In the classical domain on the other hand, several proof-of-concept experiments have realized the creation, transport and detection of mechanical states at cryogenic temperatures [23] over millimeter ranges, as well as at room temperature and atmospheric pressure [24]. The possibility of guiding a mechanical quantum state in a waveguide that confines the excitation in all directions transverse to its propagation, similar to optical fibers and waveguides, remains an open challenge.

3.2. METHODS

HERE we demonstrate a single-mode phononic waveguide directly coupled to an on-chip source and detector for non-classical mechanical states. We verify the non-classicality of the launched mechanical states by measuring their quantum correlations with an optical read-out field. In particular, we use the optomechanical interaction to

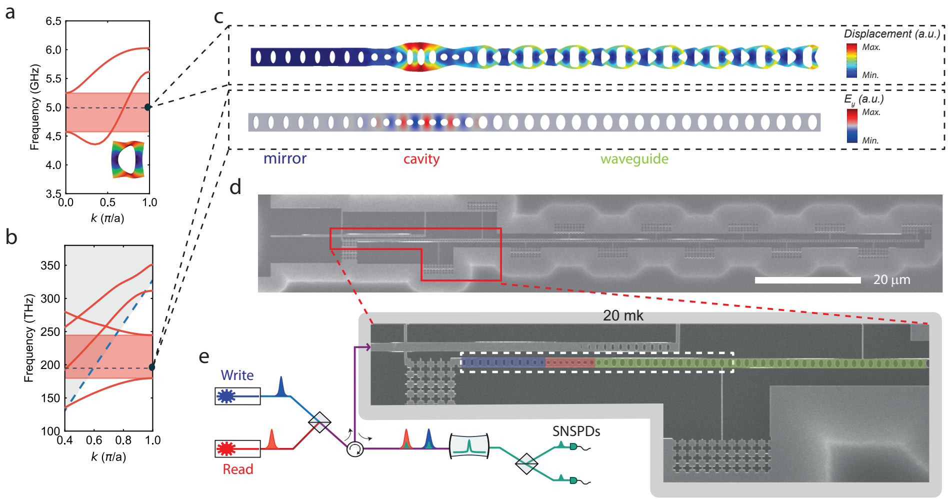

Figure 3.1: **Device and experimental setup.** a) Band diagram for the modes with symmetric displacement field with respect to the propagation direction along the waveguide. These modes are expected to couple efficiently to the resonant optomechanical cavity mode. The highlighted region (red) shows a single mode waveguide for the symmetric breathing mode with linear dispersion. The dashed line represent the frequency of the modes of the optomechanical structure. Inset: mode shape of the unit cell from this simulation for the band of interested. b) Band diagram for the optical TE mode of the phononic waveguide, exhibiting a band gap at telecom wavelengths, allowing for a confined optical mode inside the optomechanical resonator. The dashed blue line is the light cone, with the non guided modes in the gray shaded area. c) Mechanical (top) and optical (bottom) eigenfrequency simulation of the full cavity and waveguide structure. Clearly visible are the resonant breathing mode of the optomechanical crystal (left) and the waveguide mode (right). As the mechanical mode leaks through the waveguide, the optical mode stays confined inside the optomechanical resonator. d) A scanning electron microscope image of the device used in the experiment, showing the full device with mirror, cavity and the 92 μm long waveguide, as well as the optical coupling waveguide (top left). e) Schematic of the setup together with a zoomed-in section of (d) (indicated by the red box). The blue, red and green shaded regions show mirror, cavity and waveguide, respectively. The white dashed rectangle is the area of the simulation in (c). See the text and SI 3.5 for a more details.

herald the creation of a single phonon, which then leaks into the phononic waveguide. Since the waveguide has a free standing end that acts as a mirror for the phonons, the excitations bounce, i.e. reflect, back and forth with a certain characteristic time that is determined by the group velocity and the length of the waveguide. Moreover, we observe non-classical correlations between time-bin encoded phonons [25], by creating and detecting a phonon in either an early or late time window. The long mechanical lifetime of the device will also allow the creation of an on-chip network for quantum acoustic experiments. With the on-chip source, detector and waveguide presented in this work, only a phononic beam splitter and phase modulator need to be developed in order to obtain full coherent control over phonons on a chip.

We design our phononic crystal waveguide in thin-film silicon, which is single-mode for the symmetric breathing mode of the structure, in the frequency range of interest (at around 5 GHz with a single mode range of 750 MHz) and has an approximately linear dispersion, in order to maintain the spatial mode shape of the traveling phonons. This waveguide is connected to an optomechanical resonator acting as the single-phonon source and detector. For the waveguide design, only the symmetric breathing mode is considered, in order to enable a good mode overlap with the mode of the optomechanical cavity, as these resonant modes have large optomechanical coupling, and can easily be created and detected optically. At the same time, in order to realize a high-finesse optical cavity, we design our phononic waveguide to act as a mirror for photons, therefore confining the optical field in the optomechanical resonator.

The details of our design are shown in Fig. 3.1a and 3.1b, where we plot the band structure with the right mechanical symmetry, as well as the transverse electric (TE) polarized optical mode. An eigenvalue simulation of the full structure, cavity and waveguide, is shown in Fig. 3.1c. The mechanical mode extends into the waveguide, while the optical mode is strongly confined to the cavity region with a similar mode volume to previous works [4, 26–28]. The different sizes of the holes in the structure create the mirror, defect and waveguide. The hole dimensions and periodicity in the waveguide part are adjusted to tune the group velocity. We design the waveguide to have a small group velocity while still having a linear band inside the frequency range of interest (see SI for more details). From the simulated group velocity, the time duration of the mechanical packet (set by the optical pulse length of 40 ns), and the time of the mechanical excitation to leak from the cavity to the waveguide, we determine a minimum length of about 40 µm for the waveguide for the excitation to completely leave the cavity before it comes back again, which is why we choose a length of 92 µm. In order to support the long waveguide after suspension, we use narrow (50 nm wide) tethers to connect it to the surrounding silicon. Moreover, to prevent any mechanical dissipation through the tethers, they are directly connected to a phononic shield, as can be seen in the zoomed-in image of the device in Fig. 3.1e. The phononic shield features a bandgap from 4 GHz to 6 GHz, and by increasing the number of periods in the shields we can increase the mechanical lifetime (see SI). The same phononic shields are used at the left end of the device, to further increase the mechanical lifetime.

A picture of the device and sketch of the experimental setup can be found in Figure 3.1d-e. To excite and detect non-classical phonons we use laser pulses detuned from the optical resonance to address the optomechanical Stokes and anti-Stokes sidebands in order to create (write) the mechanical excitation and to map it onto the optical mode (read), respectively [29]. After being combined on a 50:50 beam splitter (BS), the light is routed via an optical circulator to the device. The reflected light from the device is then filtered using free space Fabry-Pérot cavities to block the pump laser pulses and, after another BS, is sent to the superconducting nanowire single photon detectors (SNSPDs). The device itself is cooled to 20 mK in order to initialize the mechanical mode of interest deep in the ground state.

3.3. RESULTS

FOR the initial characterization of the device, we use a tunable continuous-wave (CW) laser to determine the optical resonance in reflection. As shown in Fig. 3.2a, the fundamental optical resonance has a central wavelength around 1541 nm and a linewidth of $\kappa_t = 1021$ MHz (with extrinsic and intrinsic loss rates of $\kappa_e = 364$ MHz and $\kappa_i = 656$ MHz). We measure the mechanical spectrum using the optomechanical induced transparency

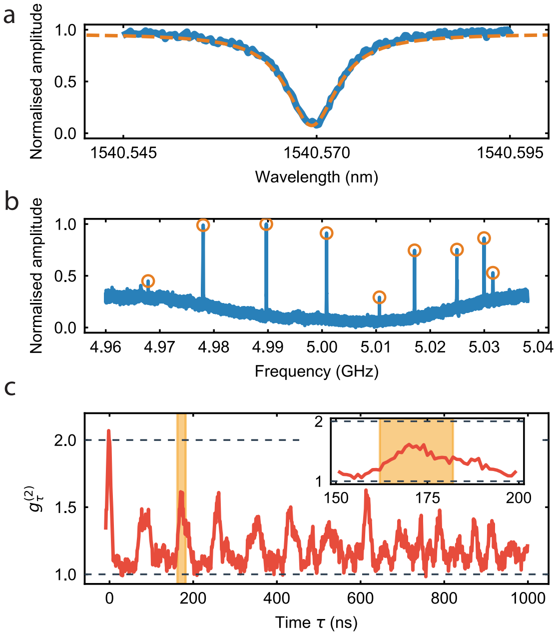

Figure 3.2: **Initial characterization.** a) Characterization of the optical resonance of the device in reflection. b) Mechanical spectrum measured using the OMIT technique at 20 mK. The series of peaks is given by the hybridization of the cavity mode and the modes of the waveguide (approximately equally spaced). c) $g_\tau^{(2)}$ of a waveguide-coupled thermal state for different delays between two detection events (τ). Note the series of peaks indicating the traveling back and forth of the phonons in the waveguide. The reduced maxima for these peaks is attributed to the non constant FSR. The area highlighted is the chosen round trip peak for the pulsed experiment with single phonon states. Inset: zoom-in around the highlighted area.

(OMIT) technique [30] (see SI for details). The resulting renormalized amplitude of the reflected probe field ($|S_{21}|$) is plotted in Fig 3.2b, where a series of (almost) equally spaced peaks shows the hybridization of the single mode of the cavity with the series of modes of the free-ended waveguide. We choose the first prominent mechanical resonance (around 4.98 GHz) as the frequency to which we detune the laser with respect to the optical resonance wavelength for addressing the Stokes and anti-Stokes interaction. We further measure the equivalent single photon optomechanical coupling rate from the Stokes scattering probability using a short optical pulse of full width at half maximum (FWHM) ≈ 40 ns, obtaining a collective $g_0/2\pi \approx 460\,\text{kHz}$ (for a detailed explanation see the SI). This is the joint coupling rate of all mechanical eigenmodes within the detection filter bandwidth.

In order to determine the time dynamics of the phononic wave packet, we measure the second order correlation function $g_\tau^{(2)}$ of the light scattered from the cavity with a CW read-out tone detuned to the anti-Stokes sideband. Due to non-negligible optical absorption in silicon, the continuous laser creates thermal mechanical population in the device [31]. In this experiment, the continuous red-detuned laser field excites thermal phonons in a broad frequency range. These phonons are read out by the same red-detuned field, which allows us to only measure the anti-Stokes scattered photons on resonance with the optical cavity. The phononic state is therefore mapped onto the photonic state, and the photons are finally detected using our SNSPDs. As a result the photon statistics of the optical field corresponds to the phonon statistics of the thermal mechanical mode. We obtain the $g_{\tau}^{(2)}$ between emitted photons from the device, by measuring two photon coincidences on two different SNSPDs and normalizing them to the single photon counts of the SNSPDs. Owing to the optomechanical interaction, this is equivalent to measuring the $g_{\tau}^{(2)}$ of the mechanical thermal states, for different delays between the SNSPDs clicks τ. The results are plotted in Fig 3.2c, showing an (almost) equally spaced series of peaks. As expected for a thermal state, at $\tau = 0$, we observe $g_{\tau}^{(2)} = 2$, which is then modulated as the state leaks into the waveguide. We attribute the reduced maxima for the round trip peaks ($g_{\tau}^{(2)} \approx 1.5$ instead of 2) to coupling to undesirable asymmetric mechanical modes (which have relatively low optomechanical coupling rate, and thus cannot be detected optically), as well as the non-constant FSR between mechanical modes of the device, which could be caused by the dispersion of the phononic waveguide. The exact effect will require a more detailed theoretical and experimental analysis in the future.

We use three 150-MHz broad filter cavities in series to filter out the strong optical driving pumps, which also filter the Stokes and anti-Stokes scattered photons within a frequency range of 80 MHz around the setpoint (4.98 GHz). In this way, any signal from the mechanical modes greater than 5.02 GHz is strongly suppressed and hence, only the part of the spectrum with the evenly spaced mechanical modes will contribute considerably to the correlation. These modes build a frequency comb with a free spectral range (FSR) of around 11 MHz, which corresponds to a rephasing time of 1/FSR = 91 ns. This is consistent with the round trip time that can be inferred from the measurement, which is around 85 ns.

In order to verify that we can guide a non-classical mechanical state, we employ a scheme in which we herald the creation of a quantum excitation in the optomechanical cavity, which we confirm by swapping out the mechanical excitation to an optical photon after some time and correlating the photon statistics from the two processes [29]. We obtain these correlations by measuring the coincidences between the events on the SNPSDs. We realize this scheme by first addressing the Stokes process with a 119 fJ blue-detuned 40 ns laser pulse creating a two-mode squeezed opto-mechanical state with scattering probability of $p_{\mathrm{s,write}} \approx 1.4\%$. Similarly, to readout the mechanical state from the optomechanical cavity, a red-detuned laser pulse with the same energy, duration and scattering probability of $p_{\mathrm{s,read}} \approx 1.4\%$, is sent to the device addressing the anti-Stokes process. These low values are chosen to avoid excess heating of the optomechanical device from the remaining optical absorption in the silicon. Note however that it has been shown that these can be increased up to around 30 % [27]. These scattering probabilities set the thermal occupation of the mode of interest to $n_{\mathrm{th}} \approx 0.27$ (see SI).

The scheme of the pulses can be seen in Fig. 3.3a and the delay between the red-detuned and blue-detuned pulses is set to approximately the second round trip time ($\tau \approx$ 170 ns). The detection of a single photon in one of the detectors from the blue-detuned pulse heralds the mechanical state of the defect to a single-phonon Fock state [27]. This phonon leaks through the attached phononic waveguide after a short time T_{c} and trav-

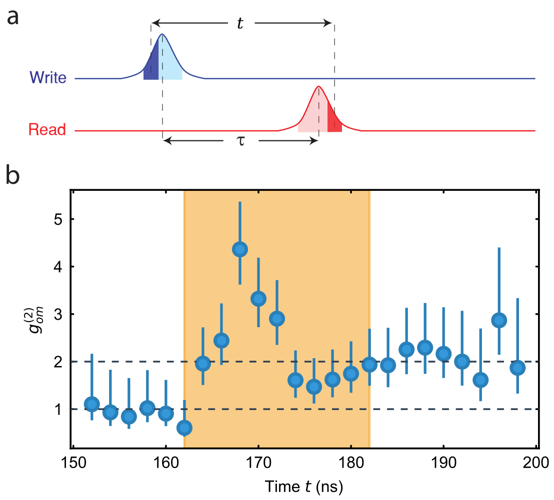

Figure 3.3: **Non-classical correlation.** a) Pulse scheme used for the cross correlation measurement. We fix the time between the pulses to $\tau \approx 170\,\mathrm{ns}$, as calibrated from the measurement of Fig 3.2c. In post-processing, we scan a narrow time window of 6 ns with an adjustable delay of t represented by the dark blue and red shaded areas over all of the acquired data (light shaded areas). This approach allows us to calculate the $g^{(2)}_{\mathrm{om}}$ of each point with an adjustable moving window. b) Cross correlation between the optical and the mechanical state for the pulsed experiment $g^{(2)}_{\mathrm{om}}(t)$. The correlation is higher than the classical threshold of 2, with a maxima of $g^{(2)}_{\mathrm{om}} = 4.4^{+1.0}_{-0.7}$, clearly demonstrating the non-classical character of the traveling phonons. For more details on the error calculation see the SI 3.5. The highlighted area in the figure has the same position as the one in Fig 3.2c.

els back and forth between the defect part and the end of the waveguide. In Figure 3.2c the highlighted area shows the chosen peak, that has a delay of $\tau \approx 170\,\mathrm{ns}$, which is much smaller than the measured lifetime $T_1 \approx 78\,\mu\mathrm{s}$ for this particular device (see the SI for more details). We choose to perform the measurement after two round trips of the phonons to avoid any overlap between the optical write and read pulses. Another reason for this is to overcome the SNSPDs' dead time of around 100 ns and hence be able to measure coincidences on the same SNSPD as well as from different SNSPDs. We would like to note that the expected cross-correlation between phonons and photons on multiple round trips is expected to be similar or slightly lower as a result of optical absorption and delayed heating [27, 29]. From this measurement, we can also infer the coupling between the cavity and the waveguide from the width of the chosen peak, obtaining a decay time of $T_c \approx 10\,\mathrm{ns}$, corresponding to a coupling rate of around $2\pi \times 16\,\mathrm{MHz}$.

In order to measure the coincidences required to determine the correlations, two 6-ns wide time windows, with a varying delay t between them, are scanned through the whole area of pulses in a post processing step (see Fig. 3.3a). Note that we also use the measurement shown in Fig. 3.2c to calibrate these filtering windows. By summing all the coincidences with each click happening in the same trial ($\Delta n = 0$, for n indicating each trial), we gather all the correlated coincidences for each delay. In order to obtain the average uncorrelated coincidences, we perform a similar post processing step, but finding coincidences in different trials ($\Delta n \neq 0$) where the clicks can be assumed to be uncorrelated. Averaging this value over different $\Delta n \neq 0$, gives the average number of uncorrelated coincidences. We use these two values to calculate $g^{(2)}_{\mathrm{om}}(t)$. The time window is chosen to be less than the coupling time between the cavity and the waveguide (T_c) in order to select only the correlated photons that have indeed traveled in the waveguide (see SI for more details). The result is shown in Fig. 3.3b. In order to gather more statistics, two separate measurements with identical thermal occupation have been used for the data shown here, one with the sequence of red and blue pulses repeated every 200 µs, the other every 300 µs. After merging all the coincidences, a maximum cross-correlation of $g^{(2)}_{\mathrm{om}} = 4.4^{+1.0}_{-0.7}$ is obtained from the reflected phonons at a time of $t = 168\,\mathrm{ns}$, which is more than 3 standard deviations above the classical threshold of 2, unambiguously showing the non-classical behavior of the guided single phonon state [29]. Furthermore, no non-classical correlations between the photons can be observed at times where the phonon is not spatially located inside the defect (i.e. outside a window of width T_c centered at $t \approx \tau \approx 170\,\mathrm{ns}$). We suspect the slightly increased correlations at longer times to be a result of the waveguide dispersion. This effect is also clearly visible in the envelope of the peak shape corresponding to the second round trip in the inset of Fig. 3.2c, with both patterns closely resembling one another.

We further explore the potential of creating a time-bin encoded phononic state by extending our scheme to using two optical excitation (write) and two detection pulses (read), effectively realizing a phononic FIFO quantum memory [32]. The identical blue-detuned optical pulses (FWHM 40 ns) have a scattering probability of $p_{\mathrm{s,write}} \approx 2.7\,\%$ with $\Delta\tau = 45\,\mathrm{ns}$ delay. The red-detuned detection pulses (FWHM 40 ns) have a scattering probability of $p_{\mathrm{s,read}} \approx 1.5\,\%$ and with the same time delay. The first blue- and red-detuned pulses are spaced by $\tau = 170\,\mathrm{ns}$ from each other and we repeat this sequence every 800 μs. We then measure the maximum cross correlation in time between all four combinations of write and read pulses, using the same technique for delay-filtering used to extract the data shown in Fig. 3.3. We choose 40-ns-long non-overlapping time windows to separate "early" write and read pulses from "late" ones, as depicted in Fig. 3.4a. As shown in Fig. 3.4b, we can clearly see strong non-classical correlation between the "early-early" and "late-late" combination of excitation and detection pulse, while observing only classical correlations (due to absorption-induced heating) between the other combinations of "early-late" and "late-early".

3.4. DISCUSSION

OUR results clearly demonstrate the potential for creating, guiding, and detecting a non-classical mechanical state inside a phononic crystal, using optomechanical techniques. Thanks to the long mechanical lifetime (up to 5.5 ms for similar devices on the same chip) and the full lateral confinement, this type of device paves the way towards on-chip quantum acoustic experiments. The current efficiency of the device is limited by residual optical absorption in the silicon, which can be reduced through improved fabrication [27] and surface passivation [33]. While some of the motivation for these experiments stems from the similarity to quantum optics, phonons are crucially different, due to the 5 orders of magnitude smaller propagation speed and the ease of coupling them

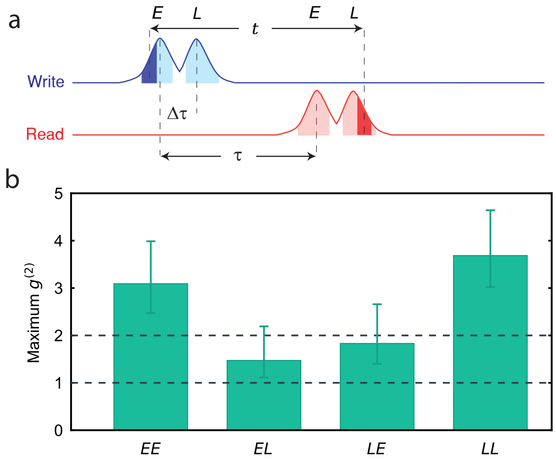

Figure 3.4: **Double pulse non-classical correlation.** a) Pulse scheme for the generation of time-bin encoded phonon states with $\Delta\tau = 45$ns and $\tau = 170$ns. The area used to gather coincidences is depicted by the light blue (red) shaded area for the write (read) pulses, respectively. In the post-processing step a similar technique as before is used, in order to achieve high timing resolution. An example of 6ns wide coincidence-filtering windows are sketched by dark blue (red) areas for write (read) pulses for the "early-late" combination. *E* (*L*) stands for early (late). b) As expected, the maximum cross correlations for the various settings clearly shows non-classical correlations for the "early-early" and "late-late" combinations, whereas in the other two we only observe classically correlated phonons.

to other quantum systems. The realization of phononic beamsplitters and phase modulators will complete the toolbox required for full control over traveling single phonons and more complex quantum experiments on a chip. Furthermore, the possibility of retrieving the state after several round-trips and with having time-bin encoded phononic states, together with the full engineerability of the bandstructure, will allow for the creation of time-bin encoded phononic qubits and an optomechanical multimode quantum memory working natively at telecom wavelengths. We also expect guided phonon modes to play a crucial role in the low-energy transmission of quantum information on a chip and for next generation filtering.

Acknowledgments We would like to thank Ewold Verhagen and Roel Burgwal for valuable discussions, as well as Moritz Forsch for experimental support. We further acknowledge assistance from the Kavli Nanolab Delft. This work is financially supported by the European Research Council (ERC CoG Q-ECHOS, 101001005), and by the Netherlands Organization for Scientific Research (NWO/OCW), as part of the Frontiers of Nanoscience program, as well as through Vidi (680-47-541/994) and Vrij Programma (680-92-18-04) grants. R.S. also acknowledges funding from the European Union under a Marie Skłodowska-Curie COFUND fellowship.

Author Contributions: A.Z., R.S. and S.G. devised and planned the experiment. A.Z. simulated, designed and fabricated the sample. A.Z., R.S. and N.F. built the setup and performed the measurements. All authors analysed the data and wrote the manuscript. S.G. supervised the project.

Competing Interests: The authors declare no competing interests.
Data Availability: Source data for the plots are available on Zenodo.

3.5. SUPPLEMENTARY INFORMATION

FABRICATION

The device is fabricated from a silicon-on-insulator chip with a device layer of 250 nm. We first pattern the structure using electron-beam lithography into the resist (CSAR) and then transfer it to the silicon layer with a SF_6/O_2 reactive-ion etch. The structure is then cleaned with a piranha solution and suspended by undercutting the sacrificial oxide layer using hydroflouric acid (HF). A last cleaning step with piranha and diluted HF (1%) is performed just before mounting the sample in the dilution refrigerator.

EXPERIMENTAL SETUP

A complete overview of the experimental setup is shown in Fig. 3.5. The optical control pulses are created from two separate tunable CW external-cavity diode lasers. They are stabilized over time using a wavelength meter (not shown) and are filtered with fiber based filter cavities (50 MHz linewidth) to suppress the classical laser noise at GHz frequencies. We create the pulses using two 110 MHz acousto-optic modulators (AOMs) gated via a pulse generator. The optical paths are combined through a fiber beamsplitter. The pulses are routed to the device in the dilution refrigerator via an optical circulator, and then to the device's optical waveguide using a lensed fiber. The optical signal coming from the device is filtered with three 150 MHz broad free-space Fabry-Pérot cavities in series, that results into an equivalent series bandwidth of about 80 MHz. The average suppression ratio is 114 dB for the blue detuned pulse and 119 dB for the red detuned pulse (the small difference is due to small misalignment and mode mismatch of the cavities). Every ~10 s the experiment is paused and continuous light is send to the filter cavities to lock them at the optical resonance of the device using optical switches. For this, the red-detuned laser is used after passing through a 50:50 beam splitter, and the detuning is compensated via an electro-optics modulator to match the optical resonance. It takes around 6 s to lock the cavities each time.

The effect of dark counts, mostly unwanted photons from stray light which couple into the fiber and leakage of pump photons through the filter chain, are negligibly small compared to the photon rate that is obtained via the Stokes and anti-Stokes scatterings. During the cross-correlation measurement shown in Fig. 3.3, we get total photon rates of approximately 8×10^{-4} and 1.7×10^{-4} per trial from the Stokes and anti-Stokes scatterings, respectively, from the full area of optical pulses. At the same time, the average total dark count rate, which is constant in time, is only 1×10^{-5} per trial.

COHERENT EXCITATION MEASUREMENT

Here we study the routing of a coherent mechanical wavepacket, as a verification to the round-trip time of the measurement of Fig. 3.2c of the main text. We excite the mechanical wave packet with a 40 ns long pulse of laser light, blue-detuned by 7 GHz with respect to optical resonance of the cavity. Importantly, as the Stokes scattered photons are more than two linewidths away from the optical resonance, the Stokes process will be highly attenuated. We pass this laser pulse through an electro-optical modulator (EOM) which produces two side bands at around 4.978 GHz (the frequency of the mechanical mode which we use to detune our lasers and also lock our free space filter cavities in front of the

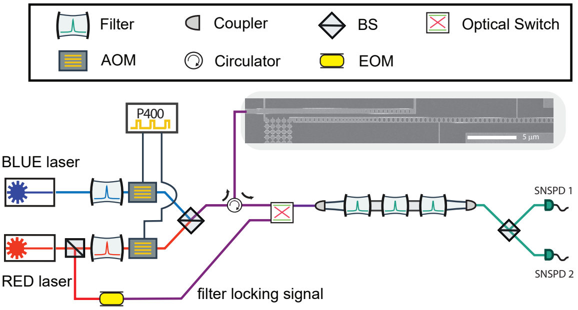

Figure 3.5: The experimental setup, with BS the beam splitter and SNSPD the superconducting nanowire single-photon detectors. See text for more details.

SNSPDs). The beating signal between these optical sidebands and the main carrier frequency now results in a coherent driving of the mechanical modes in a broad frequency range, which excites a mechanical packet inside the cavity. Following this excitation, we use a continuous red-detuned laser tone to continuously read the mechanical population. The resulting count rate from this read tone is shown in Fig. 3.6a. We can clearly see the propagating behavior of the packet, first leaving the cavity resulting in a reduction of the population, followed by the reflection back to the cavity.

In order to verify that the reflection is indeed a result of the phonon leaving the cavity, we perform the same measurement on an identical device, with a 2.5 times longer waveguide attached to it. As expected, the longer waveguide should result in a 2.5 times longer traveling time of the packet, which is fully consistent with the time difference between the peaks in Fig. 3.6b. Note that the two experiments are performed with different power settings of the coherent drive and the readout compared to the experiments in the main text, which is the reason of not seeing a full decay of the click rates in Fig. 3.6a. This results in an increased thermal background introduced by the high power readout laser, as well as the pulse length of 40 ns that is comparable with the round trip time of that device. Additionally, the peak widths are broader, since in this experiment only the modes within the bandwidth of the laser pulse will be excited. Therefore, the time domain behavior is limited by the bandwidth of the laser pulse as it is much narrower than the cavity-waveguide coupling and the bandwidth of the filter cavities.

Scattering probabilities

The Stokes and anti-Stokes scattering probabilities are determined from the click rates (Γ_r, Γ_b) on the SNSPDs and by measuring the detection efficiency of the experimental setup (η_{det})

$$\Gamma_r = p_{\text{s,read}} \cdot n_{\text{th}} \cdot \eta_{\text{det}} \tag{3.1}$$

$$\Gamma_b = p_{\text{s,write}} \cdot (1 + n_{\text{th}}) \cdot \eta_{\text{det}} \tag{3.2}$$

where the $p_{\text{s,read}}$ and $p_{\text{s,write}}$ are the scattering probabilities from the red detuned (anti-Stokes) and blue detuned (Stokes) laser pulses, respectively, and n_{th} is the mechan-

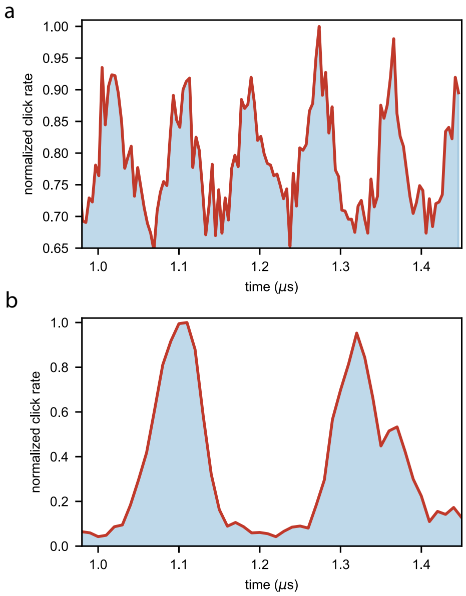

Figure 3.6: Coherent mechanical population of the cavity versus time for different waveguide lengths of a) 92 μm and b) 230 μm. The time difference between the two peaks in the bottom figure is around $\tau \approx 210\,$ns compared to $\tau \approx 85\,$ns for the shorter waveguide, which is fully consistent with the difference in waveguide length.

ical mode thermal phonon occupancy. The measurement of the detection efficiency gives $\eta_{\text{det}} \approx 3.8\%$. This includes the coupling between the optical cavity and the optical coupler waveguide η_{dev}, the coupling from fiber to the optical coupler waveguide η_{c}, the filter setup efficiency η_{F}, the SNSPDs detection efficiency η_{SNSPD}, as well as all other losses in the optical path η_{loss}. Hence, the overall detection efficiency can be written as $\eta_{\text{det}} = \eta_{\text{c}} \cdot \eta_{\text{dev}} \cdot \eta_{\text{F}} \cdot \eta_{\text{SNSPD}} \cdot \eta_{\text{loss}}$. By shining a continuous off-resonance laser to the device and measuring the power at each point of the setup, we obtain $\eta_{\text{c}} = 37\%$, $\eta_{\text{F}} = 38\%$, $\eta_{\text{SNSPD}} \approx 90\%$ and $\eta_{\text{loss}} \approx 80\%$. Furthermore, the device efficiency $\eta_{\text{dev}} = \frac{\kappa_{\text{e}}}{\kappa_{\text{t}}}$ and is measured using a similar method to [34].

In the weak coupling regime ($g \ll \kappa$), the scattering probabilities are given by the efficiency ($\eta_{\text{dev}} = \frac{\kappa_{\text{e}}}{\kappa_{\text{t}}}$) and the incident laser pulse energy E_{p} [27]:

$$p_{\text{s,read}} = 1 - \exp\left(\frac{-4\eta_{\text{dev}} g_0^2 E_{\text{p}}}{\hbar\omega_{\text{c}}(\omega_m^2 + (\kappa_{\text{t}}/2)^2)}\right) \tag{3.3}$$

$$p_{\text{s,write}} = \exp\left(\frac{4\eta_{\text{dev}} g_0^2 E_{\text{p}}}{\hbar\omega_{\text{c}}(\omega_m^2 + (\kappa_{\text{t}}/2)^2)}\right) - 1 \tag{3.4}$$

where ω_{c} is the optical resonance frequency and ω_m the mechanical frequency.

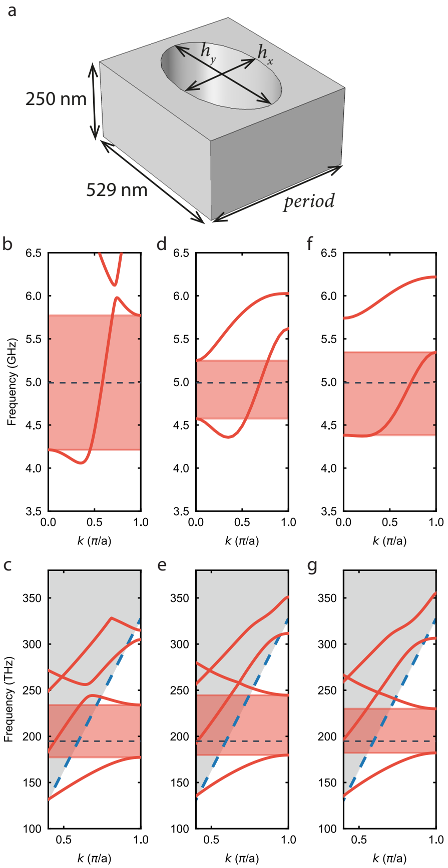

Figure 3.7: Engineering the band structure and phonon group velocity by adjusting the hole dimensions: h_x diameter along the waveguide orientation, h_y, diameter perpendicular to the waveguide orientation, and the size of the unit cell (period). A sketch of the unit cell is shown in a). b,c) Mechanical and optical band diagram for a waveguide with parameters of $h_y = 187\,\text{nm}$, $h_x = 320\,\text{nm}$, $period = 436\,\text{nm}$ resulting in a mechanical group velocity of $v_g = 1946\ m/s$. d,e) Parameters of $h_y = 430\,\text{nm}$, $h_x = 272\,\text{nm}$, $period = 458\,\text{nm}$, with $v_g = 2766\ m/s$. f,g) Parameters of $h_y = 468\,\text{nm}$, $hw = 240\,\text{nm}$, $period = 458\,\text{nm}$, with $v_g = 6298\ m/s$. In our experiment, we use the second set of parameters (shown in d) and e)) in order to have a small group velocity, while simultaneously maintaining a linear region of the mechanical band to minimize dispersion.

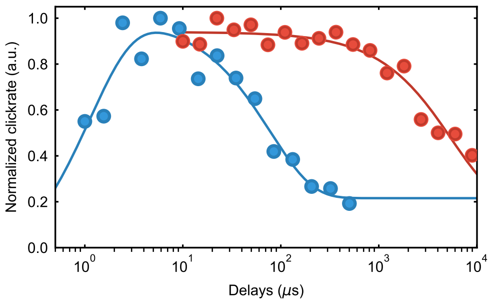

Figure 3.8: Normalized clickrates (directly proportional to the thermal population) from a thermally excited mechanical mode as a function of time. The population exhibits a double exponential behavior, which corresponds to the initial heating and subsequent decay. For the device used in the measurements the rise and decay times are $T_{\text{rise}} \approx 1\,\mu\text{s}$ and $T_1 \approx 78\,\mu\text{s}$ (data in blue), respectively. An exemplary second device, with increased number of phononic shield periods connected to the tethers, resulting in an much longer decay time $T_1 \approx 5.5\,\text{ms}$ is also shown (data in red). The solid lines are exponential fits to the data.

BAND STRUCTURE

The band structure of the waveguide can be engineered by changing the hole dimensions and the periodicity of unit cells, while keeping the width and thickness of the beam fixed. In Fig. 3.7 three designs of a waveguide with different mechanical band structure and group velocity are shown. All these designs act as optical mirrors for the cavity, as can be seen from the optical band diagrams.

LIFETIME

One of the fundamental properties of the device is the extremely long lifetime T_1 of the mechanical excitation. In order to measure T_1 we use a red detuned strong optical pulse to heat the device, creating a thermal population in the mode. We then send another, much weaker, red detuned pulse, to probe the thermal population as a function of time, which is directly proportional to the clickrates. The result of the measurement is shown in Fig. 3.8. Note that, as previously seen [7], the clickrates have a double exponential trend, with a rise time T_{rise} and a decay time T_1. For our measurement we choose one of the shorter lifetime devices (to allow for higher repetition rates), while several structures with up to 5.5 ms are also fabricated on the same chip, as shown in the plot.

THERMAL OCCUPANCY OF THE MECHANICAL MODE

The mechanical modes, having a frequency of around 5 GHz, have a thermal occupation of $< 10^{-5}$ at 20 mK. Due to absorption of the optical pulses used to create and read the state, the thermal occupation during the experiment is however significantly higher. We measure the mode temperature via the sideband asymmetry as shown in figure Fig. 3.9a. In more detail, we send a blue-detuned and red-detuned optical pulse with exactly equal energies (and thus equal scattering probabilities) and a long delay between (few times of the mechanical lifetime in order to reinitialize to the ground state at the starting of each pulse) and measure the click rates from each pulse (Γ_r, Γ_b). Using Eq. 3.1 and 3.2, we extract the thermal occupancy for different scattering probabilities. This measurement allows us calibrate the mode heating that occurs during the optical red-detuned (anti-Stokes) pulse, the instantaneous heating. To mimic the real experimental conditions with two pulses (as used for Fig. 3.3a), we send an additional red detuned pulse to the device 170 ns before the pulses used to measure the thermal occupation, which effectively heats the mechanical mode. The results are shown in Fig. 3.9b, where the x-axis is the inferred scattering probability of the heating pulse.

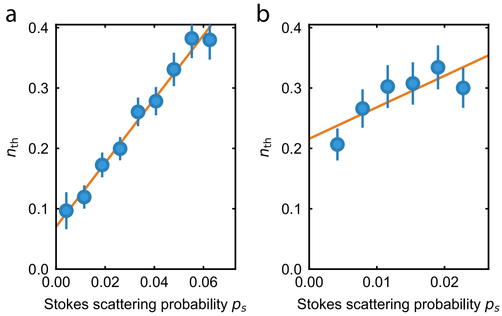

Figure 3.9: a) Thermal occupation of the mode of interest as a function of the scattering probability of the Stokes and anti-Stokes process $p_{s,write} = p_{s,read} = p_s$. n_{th} is measured from the asymmetry of Stokes/anti-Stokes scattering rates. The fit follows $n_{th} = (0.070 \pm 0.0095) + (5.29 \pm 0.25) \times p_s$. We choose to work at $p_{s,read} =$ 1.4%. b) Thermal occupation with the pulse scheme of the experiment as a function of the inferred scattering probability of the anti-Stokes process for the heating pulse. Here a heating pulse is sent to the device 170 ns before the pulses used to measure the thermal occupation. Since the heating dynamics is similar for both Stokes and anti-Stokes processes, we can send either a red-detuned or a blue-detuned pulse as heating pulse. The fitting of the resulting data follows $n_{th} = (0.216 \pm 0.028) + (5.21 \pm 1.88) \times p_s$. Choosing a scattering probability of $p_{s,write} = 1.4\%$ results in a total thermal occupation of $n_{th} \approx 0.27$. In both figures the fits are linear and the errors are one standard deviation.

ERROR ON THE $g^{(2)}_{OM}$

As discussed in the main text, we record the coincidences from the same trial ($N_{\Delta n=0}$, where n is an indicator for each experimental round), and the average number of coincidences from different trials ($\overline{N}_{\Delta n \neq 0}$), which is expected to be uncorrelated. In order to calculate the $g^{(2)}_{om}$ we divide these two quantities, such that $g^{(2)}_{om}(t) = N_{\Delta n=0}(t)/\overline{N}_{\Delta n \neq 0}(t)$. Using $\Delta n \gg 1$, one can gather enough statistics to estimate $\overline{N}_{\Delta n \neq 0}$ with a negligible error. For the estimation of the error on $N_{\Delta n=0}$, which dominates the statistical uncertainty, a binomial distribution function is considered for the number of coincidences on each trial. Therefore, from this distribution, the probability of getting different numbers of coincidences can be calculated and thus, the error of the number of coincidences will be estimated. This is similar to the method used in [29].

EFFECT OF TIME FILTERING WINDOW ON $g^{(2)}_{OM}$

Due the strong coupling between the optomechanical defect and the mechanical waveguide, the phononic packet has a narrow length of around $T_c \approx 10$ ns. Therefore, in order to study the non-classical properties of the phononic packet, we have to filter the coincidences happening with a certain delay in time, with a narrow time window around that delay. In Fig. 3.3 the width of the time filtering window is 6 ns and the delay of the window is scanned through the write and read pulses for each delay. The cross-correlation is calculated by dividing the number of coincidences happening in the same trial ($\Delta n = 0$), by the number of coincidences happening in different trials ($\Delta n \neq 0$), which are uncorrelated. By changing the filtering window, the number of uncorrelated coincidences resulting from the thermal background noise of mechanical motion is changed, reducing the cross correlations resulting from the heralded mechanical state. To further study this effect, we plot the cross correlations in Fig. 3.10, where we increase the filtering window from 3 ns to 30 ns. As can be seen, with a shorter filtering window the number of coincidences gathered for each delay is a reduced and thus, despite having a higher cross correlation, the error bars of the measurement is also larger. For window widths smaller than the packet lifetime we recover strong correlations, however for widths shorter than 5 ns we only obtain a small number of coincidences, resulting in an increased uncertainty in the correlation parameter. For windows longer than the packet length, the increased contribution of uncorrelated coincidences reduces the measured correlations. Please note that the cross-correlations of classical state can never exceed 2.

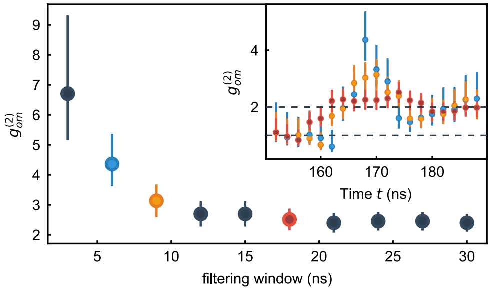

Figure 3.10: Maximum cross correlations obtained with varying filtering window width, using similar time delays as in Fig. 3.3. Inset: full cross correlations as a function of time for 3 selected data points.

DOUBLE PULSE $g^{(2)}_{\mathrm{OM}}(t)$

In this experiment we use two write and two read pulses. In Fig. 3.11a, the click rates are shown in time. The two pairs of pulses are clearly overlapping, since the delay between them is close to their FWHM. We gather coincidences from the shaded area of the pulses, choosing them to not overlap to not double count coincidences. We use a similar technique to the one use for Fig. 3.3, with filtering the coincidences in a 6 ns time window with varying delays, in order to obtain finer time resolution. In Fig. 3.11b, the cross correlation between these fine-filtered coincidences is shown as a function of delay between them for different combinations of write and read pulse. The maximum cross correlation of these plots is depicted in Fig. 3.4b. Note that the maximum cross correlation for "early-early" and "late-late" combinations happen at $t \approx 170$ ns which matches the second round trip of phonons, as expected.

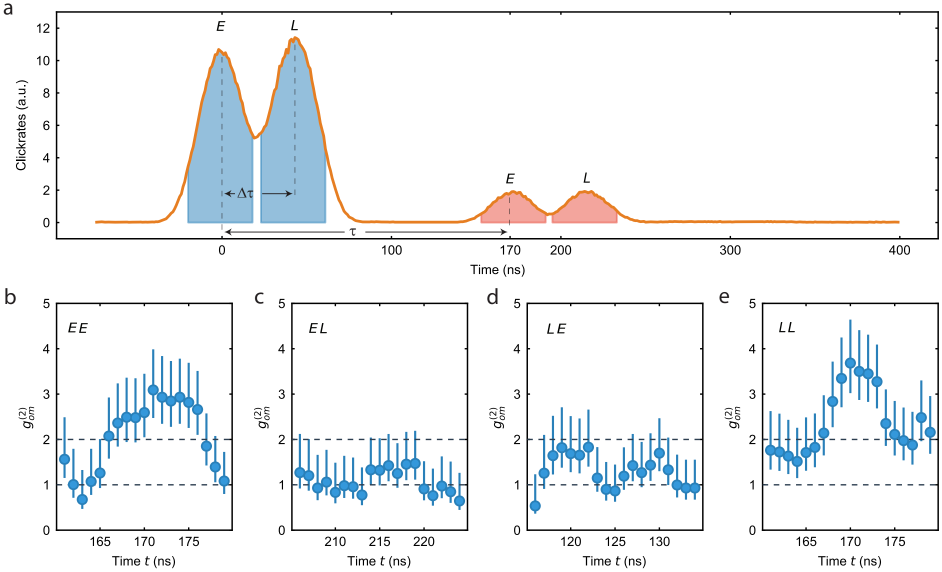

Figure 3.11: a) Double-pulse click rate versus time. The two slightly overlapping write pulses preceding the read pulses are clearly distinguishable into earlier and later time. The delay between pulses is $\tau = 170\,\text{ns}$ for both "early-early" and "late-late" combinations, $\tau + \Delta\tau = 215\,\text{ns}$ for "early-late", and $\tau - \Delta\tau = 125\,\text{ns}$ for "late-early". b) Cross correlation between coincidences having a delay not more than 10 ns deviation from the delay between pulses, for different combinations. In all figures here "E"("L") stands for "early"("late").

THEORY OF OPTOMECHANICAL INDUCED TRANSPARENCY

We assume to have an optomechanical cavity which is coupled to a truncated waveguide, acting as a Fabry-Pérot interferometer, and can write the total Hamiltonian ($\hbar = 1$) as

$$\begin{aligned} H = &\omega_c a^\dagger a + \omega_m b^\dagger b + \sum_l \omega_l c_l^\dagger c_l + \sum_l \gamma_{e,l} c_l^\dagger b + h.c. \\ &+ g_0 a^\dagger a (b^\dagger + b) \end{aligned} \tag{3.5}$$

where a and b are the annihilation operators for the optical and mechanical modes of the optomechanical cavity and g_0 represents the single photon optomechanical coupling rate. Additionally, $\gamma_{e,l}$ represents the coupling between the mechanical mode of the cavity and the l-th mode of the Fabry-Pérot interferometer with annihilation operator c_l and frequency ω_l.

The linearized Hamiltonian in the rotating frame of the laser field after applying the perturbation over the optical field is then given by [1]

$$\begin{aligned} H = &\Delta a^\dagger a + \omega_m b^\dagger b + g_0 \alpha (a^\dagger + a)(b^\dagger + b) \\ &+ \sum_l \Omega_l c_l^\dagger c_l + \sum_l \gamma_{e,l} c_l^\dagger b + h.c. \end{aligned} \tag{3.6}$$

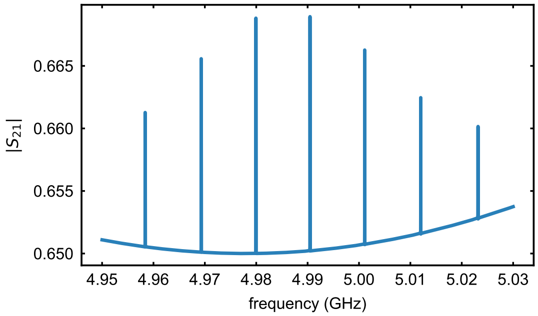

Figure 3.12: Numerically calculated S_{21} signal, using the parameters given in the main text.

where $\Delta = \omega_c - \omega_l$ is the detuning of the cavity with respect to the laser frequency. Here, a is now the annihilation operator for the optical field fluctuation inside the cavity with the steady state field of α. The equivalent optomechanical coupling to the field fluctuation is defined by $g = g_0.\alpha$.

The Langevin equations after applying the rotating wave approximation, by assuming having the pump field at the red sideband and neglecting the counter rotating terms, follow as

$$\frac{da}{dt} = -i\Delta a - igb - \frac{\kappa}{2}a + \sqrt{\kappa_e}a_{in} \tag{3.7}$$

$$\frac{db}{dt} = -i\omega_m b - iga - \frac{\Gamma_m}{2}b - i\sum_l \gamma_{e,l}c_l \tag{3.8}$$

$$\frac{dc_l}{dt} = -i\omega_l c_l - i\gamma_{e,l}b - \frac{\Gamma_l}{2}b \tag{3.9}$$

Here κ is the optical decay which includes both external and internal cavity loss $\kappa = \kappa_e + \kappa_i$. Similarly, Γ_m and Γ_l are the mechanical decay rate for the cavity mechanical mode and l-th mechanical mode of the Fabry-Pérot interferometer, respectively. Also, a_{in} are the cavity input field fluctuations.

For an OMIT measurement we pass the pump laser field through an amplitude EOM which produces sidebands at frequency ω, thus the input field to the system can be written as $E_0 + E_+e^{-i\omega t} + E_-e^{i\omega t}$. We are now interested in calculating the reflection coefficients of each component and eventually calculate the output field as $a_{out} = r_0E_0 + r_+E_+e^{-i\omega t} + r_-E_-e^{i\omega t}$. Without loss of generality, we can assume that the two sidebands are equal and produced in-phase ($E_+ = E_- = E_1$) by the amplitude EOM. Moreover, by operating in the resolved sideband regime ($\kappa < \omega_m, \Delta$), the fields at frequencies far detuned from the cavity frequency reflect identically and we can assume $r_0 \approx r_- \approx 1$. We therefore have to only calculate the reflection coefficient of the component close to the cavity resonance r_+. By considering only this input field in Eq. 3.7 and assuming $a = a_+e^{-i\omega t}$, $b = b_+e^{-i\omega t}$ and $c_l = c_{+,l}e^{-i\omega t}$, we have

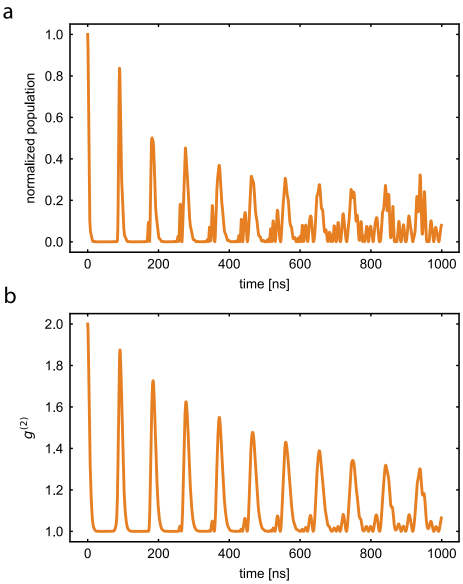

Figure 3.13: a) Simulated normalized cavity population as a function of time, detected after passing through the filter cavities. b) Second order correlation function of the cavity mechanical field, calculated using the Siegert relation.

$$b_+ = \frac{g}{\omega - \omega_m + i\frac{\Gamma_m}{2} - \sum_l \frac{\gamma_{e,l}^2}{\omega - \omega_l + i\frac{\Gamma_l}{2}}} a_+ \tag{3.10}$$

$$a_+ = \frac{i\kappa_e}{\omega - \Delta + i\frac{\kappa}{2} - \chi(\omega)} E_1 \tag{3.11}$$

$$\chi(\omega) = \frac{g^2}{\omega - \omega_m + i\frac{\Gamma_m}{2} - \sum_l \frac{\gamma_{e,l}^2}{\omega - \omega_l + i\frac{\Gamma_l}{2}}} \tag{3.12}$$

with $\chi(\omega)$ being the mechanical susceptibility to the optical field. After that, by using the input-output relation of $a_{out} = a_{in} - \sqrt{\kappa_e} a$, we can extract the reflection coefficient as

$$r_+ = 1 - \frac{i\kappa_e}{\omega - \Delta + i\frac{\kappa}{2} - \chi(\omega)} \tag{3.13}$$

A fast photodiode detects the power of the output field as

$$\begin{aligned} P = |E_0|^2 + |E_1|^2 + |r_+ E_1|^2 + E_0 E_1 e^{-i\omega t} + \\ r_+ E_0 E_1 e^{-i\omega t} + r_+ |E_1|^2 e^{-i2\omega t} + c.c. \end{aligned} \tag{3.14}$$

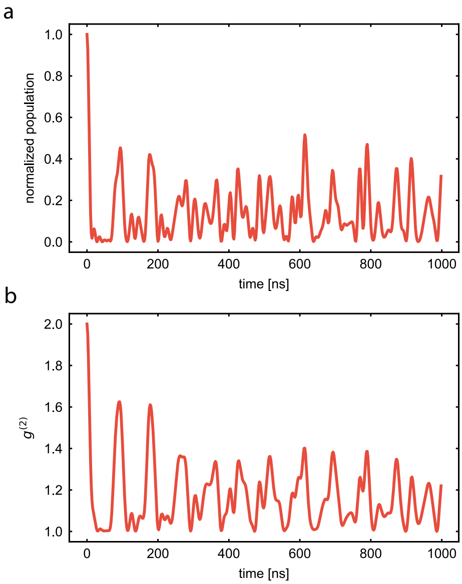

Figure 3.14: We apply the same model to the OMIT spectrum measured for the real device in the main text, obtaining the cavity population and $g^{(2)}$ of a thermal state as a function of time.

The voltage produced by the fast photodiode is connected to channel 2 of a vector network analyzer (VNA) which measures the quadratures of the signal, and thus measures S_{21} with magnitude of $|S_{21}| = \frac{1+Re\{r_+\}}{2}$. For simplicity, we assume all the Fabry-Pérot interferometer modes to have a similar coupling rate to the cavity. We now numerically calculate and plot this signal in Fig. 3.12 given the parameters of the system, which are reported in the main text. The resulting graph is very similar to the measurement shown in Fig. 3.2b. Note that the peaks in the transparency window at each mechanical mode are a direct result of the optomechanical coupling in the denominator of Eq. 3.13.

MECHANICAL RESPONSE OF THE CAVITY-WAVEGUIDE STRUCTURE

In order to develop a simple theoretical model describing the measurements in Fig. 3.2c in the main text we first look at the time domain behavior of the mechanical system and then calculate its $g^{(2)}$ function. The state-swap interaction performed with the red-detuned optical drive is such that the optical $g^{(2)}$ we recover reproduces the mechanical state [27]. For the time domain response we use Eq. 3.8 and Eq. 3.9, where we set the optomechanical interaction term to zero ($g \approx 0$). We solve them using a Python module that solves a system of linearly coupled differential equations (Scipy.integrate.odeint module), with the initial conditions of having a unity population in the cavity ($b(0) = 1$) and all the Fabry-Pérot interferometer modes in the vacuum state ($c_l(0) = 0$). For simplicity, we solve the time dynamics for scalar classical fields. We then use the solution of $b(t)$ to further obtain the cavity population and the first order correlation function $g^{(1)}$

$$g_\tau^{(1)} = \frac{\int \langle b^\dagger(t) b(t+\tau) \rangle \, dt}{\int \langle |b(t)|^2 \rangle \, dt} \tag{3.15}$$

We then proceed by using the Siegert relation [35] to calculate the second order correlation $g_\tau^{(2)}$ of a thermal chaotic field

$$g_\tau^{(2)} = 1 + |g_\tau^{(1)}|^2 \tag{3.16}$$

The general results for our simple model including the time domain response of the cavity population, as well as the intensity correlation $g_\tau^{(2)}$ are shown in Fig. 3.13. The model clearly shows that having the adjacent waveguide results in a leakage of the phonon population, followed by a subsequent revival after each round-trip with the reflection from the free-standing end. A similar behavior is observed for the intensity correlation, where $g_\tau^{(2)}$ decays as the thermal field leaves the cavity and then rises again as the mechanical field reflects back into the cavity.

We can now use the same method in combination with the measured OMIT data as the input and simulate the expected time domain response, as well as the mechanical $g_\tau^{(2)}$ as a function of time, using the same assumptions as above (see Fig. 3.14). This simple model allows us to qualitatively model our measured data from Fig. 3.2c very well.

3.6. APPENDIX

In this appendix we report some facts and some *a posteriori* consideration on the experiment reported in this chapter. The idea is to give insights on the challenges encountered on the path to acquire the final dataset.

- Since a cooldown and a warm up of a dilution refrigerator takes 3 days, having a reliable metric to characterize the devices ar room temperature was a fundamental part of this work. As shown in SI section 3.5, we found that the mechanical spectrum is a reliable metric to determine the bouncing pattern of the phononic packet.

- Having a constant FSR in the mechanical spectrum is fundamental to have high $g_{\text{om}}^{(2)}$ on the bounced phonons. However having also a short lifetime is important to reduce the integration time. We suggest to have most of the devices with short lifetime on chip and only a few, as proof of principle, with long lifetime.

REFERENCES

[1] M. Aspelmeyer, T. J. Kippenberg, and F. Marquardt, Cavity optomechanics, Rev. Mod. Phys. **86**, 1391 (2014).

[2] A. D. O'Connell, M. Hofheinz, M. Ansmann, R. C. Bialczak, M. Lenander, E. Lucero, M. Neeley, D. Sank, H. Wang, M. Weides, J. Wenner, J. M. Martinis, and A. N. Cleland, Quantum ground state and single-phonon control of a mechanical resonator, Nature **464**, 697 (2010).

[3] T. Palomaki, J. Teufel, R. Simmonds, and K. Lehnert, Entangling mechanical motion with microwave fields, Science **342**, 710 (2013).

[4] R. Riedinger, A. Wallucks, I. Marinković, C. Löschnauer, M. Aspelmeyer, S. Hong, and S. Gröblacher, Remote quantum entanglement between two micromechanical oscillators, Nature **556**, 473 (2018).

[5] C. F. Ockeloen-Korppi, E. Damskägg, J.-M. Pirkkalainen, M. Asjad, A. A. Clerk, F. Massel, M. J. Woolley, and M. A. Sillanpää, Stabilized entanglement of massive mechanical oscillators, Nature **556**, 478 (2018).

[6] I. Marinković, A. Wallucks, R. Riedinger, S. Hong, M. Aspelmeyer, and S. Gröblacher, An optomechanical Bell test, Phys. Rev. Lett. **121**, 220404 (2018).

[7] A. Wallucks, I. Marinković, B. Hensen, R. Stockill, and S. Gröblacher, A quantum memory at telecom wavelengths, Nat. Phys. **16**, 772 (2020).

[8] R. W. Andrews, R. W. Peterson, T. P. Purdy, K. Cicak, R. W. Simmonds, C. A. Regal, and K. W. Lehnert, Bidirectional and efficient conversion between microwave and optical light, Nature Phys. **10**, 321 (2014).

[9] A. Vainsencher, K. J. Satzinger, G. A. Peairs, and A. N. Cleland, Bi-directional conversion between microwave and optical frequencies in a piezoelectric optomechanical device, Appl. Phys. Lett. **109**, 033107 (2016).

[10] M. Forsch, R. Stockill, A. Wallucks, I. Marinković, C. Gärtner, R. A. Norte, F. van Otten, A. Fiore, K. Srinivasan, and S. Gröblacher, Microwave-to-optics conversion using a mechanical oscillator in its quantum groundstate, Nature Phys. **16**, 69 (2020).

[11] M. Mirhosseini, A. Sipahigil, M. Kalaee, and O. Painter, Superconducting qubit to optical photon transduction, Nature **588**, 599 (2020).

[12] S. J. M. Habraken, K. Stannigel, M. D. Lukin, P. Zoller, and P. Rabl, Continuous mode cooling and phonon routers for phononic quantum networks, New J. Phys. **14**, 115004 (2012).

[13] P. Delsing *et al.*, The 2019 surface acoustic waves roadmap, J. Phys. D: Appl. Phys. **52**, 353001 (2019).

[14] M. J. A. Schuetz, E. M. Kessler, G. Giedke, L. M. K. Vandersypen, M. D. Lukin, and J. I. Cirac, Universal Quantum Transducers Based on Surface Acoustic Waves, Phys. Rev. X **5**, 031031 (2015).

[15] A. Bienfait, K. J. Satzinger, Y. P. Zhong, H.-S. Chang, M.-H. Chou, C. R. Conner, E. Dumur, J. Grebel, G. A. Peairs, R. G. Povey, and A. N. Cleland, Phonon-mediated quantum state transfer and remote qubit entanglement, Science **364**, 368 (2019).

[16] D. A. Golter, T. Oo, M. Amezcua, I. Lekavicius, K. A. Stewart, and H. Wang, Coupling a surface acoustic wave to an electron spin in diamond via a dark state, Phys. Rev. X **6**, 041060 (2016).

[17] S. Hermelin, S. Takada, M. Yamamoto, S. Tarucha, A. D. Wieck, L. Saminadayar, C. Bäuerle, and T. Meunier, Electrons surfing on a sound wave as a platform for quantum optics with flying electrons, Nature **477**, 435 (2011).

[18] R. P. G. McNeil, M. Kataoka, C. J. B. Ford, C. H. W. Barnes, D. Anderson, G. A. C. Jones, I. Farrer, and D. A. Ritchie, On-demand single-electron transfer between distant quantum dots, Nature **477**, 439 (2011).

[19] M. C. Kuzyk and H. Wang, Scaling phononic quantum networks of solid-state spins with closed mechanical subsystems, Phys. Rev. X **8**, 041027 (2018).

[20] Y. Chu and S. Gröblacher, A perspective on hybrid quantum opto- and electromechanical systems, Appl. Phys. Lett. **117**, 150503 (2020).

[21] M. V. Gustafsson, P. V. Santos, G. Johansson, and P. Delsing, Local probing of propagating acoustic waves in a gigahertz echo chamber, Nature Phys. **8**, 338 (2012).

[22] M. V. Gustafsson, T. Aref, A. F. Kockum, M. K. Ekström, G. Johansson, and P. Delsing, Propagating phonons coupled to an artificial atom, Science **346**, 207 (2014).

[23] R. N. Patel, Z. Wang, W. Jiang, C. J. Sarabalis, J. T. Hill, and A. H. Safavi-Naeini, Single-mode phononic wire, Phys. Rev. Lett. **121**, 040501 (2018).

[24] K. Fang, M. H. Matheny, X. Luan, and O. Painter, Optical transduction and routing of microwave phonons in cavity-optomechanical circuits, Nature Photon. **10**, 489 (2016).

[25] P. Farrera, G. Heinze, and H. De Riedmatten, Entanglement between a Photonic Time-Bin Qubit and a Collective Atomic Spin Excitation, Phys. Rev. Lett. **120**, 100501 (2018).

[26] J. Chan, A. H. Safavi-Naeini, J. T. Hill, S. Meenehan, and O. Painter, Optimized optomechanical crystal cavity with acoustic radiation shield, App. Phys. Lett. **101**, 081115 (2012).

[27] S. Hong, R. Riedinger, I. Marinković, A. Wallucks, S. G. Hofer, R. A. Norte, M. Aspelmeyer, and S. Gröblacher, Hanbury Brown and Twiss interferometry of single phonons from an optomechanical resonator, Science **358**, 203 (2017).

[28] L. Qiu, I. Shomroni, P. Seidler, and T. J. Kippenberg, Laser cooling of a nanomechanical oscillator to its zero-point energy, Phys. Rev. Lett. **124**, 173601 (2020).

[29] R. Riedinger, S. Hong, R. A. Norte, J. A. Slater, J. Shang, A. G. Krause, V. Anant, M. Aspelmeyer, and S. Gröblacher, Non-classical correlations between single photons and phonons from a mechanical oscillator, Nature **530**, 313 (2016).

[30] S. Weis, R. Rivière, S. Deléglise, E. Gavartin, O. Arcizet, A. Schliesser, and T. J. Kippenberg, Optomechanically Induced Transparency, Science **330**, 1520 (2010).

[31] S. M. Meenehan, J. D. Cohen, S. Gröblacher, J. T. Hill, A. H. Safavi-Naeini, M. Aspelmeyer, and O. Painter, Silicon optomechanical crystal resonator at millikelvin temperatures, Phys. Rev. A **90**, 011803 (2014).

[32] X.-L. Pang, A.-L. Yang, J.-P. Dou, H. Li, C.-N. Zhang, E. Poem, D. J. Saunders, H. Tang, J. Nunn, I. A. Walmsley, and X.-M. Jin, A hybrid quantum memory-enabled network at room temperature, Sci. Adv. **6**, eaax1425 (2020).

[33] M. Borselli, T. J. Johnson, and O. Painter, Measuring the role of surface chemistry in silicon microphotonics, Appl. Phys. Lett. **88**, 131114 (2006).

[34] S. Gröblacher, J. T. Hill, A. H. Safavi-Naeini, J. Chan, and O. Painter, Highly efficient coupling from an optical fiber to a nanoscale silicon optomechanical cavity, Appl. Phys. Lett., **103**, 181104 (2013).

[35] A. Lebreton, I. Abram, N. Takemura, M. Kuwata-Gonokami, I. Robert-Philip, and A. Beveratos, Stochastically sustained population oscillations in high-β nanolasers, New J. Phys. **15**, 033039 (2013).

4

ON-CHIP DISTRIBUTION OF QUANTUM INFORMATION USING TRAVELING PHONONS

**Amirparsa ZIVARI*, Niccolò FIASCHI*, Roel BURGWAL,
Ewold VERHAGEN, Robert STOCKILL, Simon GRÖBLACHER**

Distributing quantum entanglement on a chip is a crucial step towards realizing scalable quantum processors. Traveling phonons – quantized guided mechanical wavepackets – can be used as a medium to transmit quantum states, due to their small size and low propagation speed compared to other carriers, such as electrons or photons. Moreover, phonons are highly promising candidates to connect heterogeneous quantum systems on a chip, such as microwave and optical photons for long-distance transmission of quantum states via optical fibers. Here, we experimentally demonstrate the distribution of quantum information using phonons, entangling two traveling phonons and creating a time-bin encoded traveling phononic qubit. The mechanical quantum state is generated in an optomechanical cavity and propagates into a phononic waveguide for around 200 micrometers. We further prove that the entangles phonon-photon pair can be used to violate a Bell-type inequality.

Parts of this chapter have been published in Amirparsa Zivari*, Niccolò Fiaschi*, Roel Burgwal, Ewold Verhagen, Robert Stockill, and Simon Gröblacher, *On-chip distribution of quantum information using traveling phonons*, Science Advances Vol 8, Issue 46 (2022).
* indicates equal contribution

4.1. INTRODUCTION

OVER the past decades, quantum technologies have evolved from scientific proof-of-principle experiments to a nascent and thriving industry. With recent demonstrations of quantum advantage over classical computation in multiple systems [1, 2], the need for connecting such resources is becoming ever more urgent. Distributing quantum entanglement between distant parties is a crucial step towards implementing quantum repeaters and networks [3, 4]. Distributing it on-chip is needed for sparse qubit array architectures, which require on-chip long-range qubit couplers [5]. Additionally, having entanglement between a stationary quantum memory and a flying qubit plays a central role in low-loss quantum information transfer over long distances [3].

One of the key challenges of building a quantum network is forming interfaces between heterogeneous quantum devices. A highly versatile system for this task has been identified in phonons, which can act as efficient intermediaries between different resources [6]. In particular, phonons have been shown to be highly useful in converting states between different optical wavelengths [7], as well as for microwave to optics frequency conversion [8–14]. Most recently, such a mechanical transducer has been used to transfer signals from a superconducting qubit to an optical fiber [15], a key step for quantum information transfer. Moreover, the potential for quantum gate operations using phonons has been shown [16–18], owing to long coherence times and high transfer fidelities of phonons. The interest in traveling phonons in fact goes well beyond enabling long-distance quantum networks. Several of the most exciting prospects are arising from their many orders of magnitude slower propagation speed compared to light, low loss transmission and their small mode volume compared to traveling GHz photons. These unique features could have the potential to enable the on-chip distribution and processing of quantum information in a highly compact fashion [19], allow for coherent interactions with a large variety of quantum systems such as defect centers [20], superconducting qubits [21] and quantum dots [22, 23], in both homogeneous or heterogeneous implementations [24]. Demonstrating the basic building blocks, such as marking the distribution of quantum information using highly confined phonons, remains an open challenge to date.

Quantum optomechanics has proven to be a versatile toolbox for controlling stationary, strongly confined phonons [25, 26]. Previously, bulk and surface acoustic waves (BAWs and SAWs, respectively) have been shown to be able to operate in the quantum regime [17, 19], for example, by coupling to superconducting qubits for transducer and quantum information applications [27, 28], as well as entangling acoustic phonons [29]. These systems benefit from deterministic quantum operations with high fidelities, enabled by the non-linearity of the superconducting qubit and strong coupling between the qubit and the phononic channel. However, the confinement of the phonons in optomechanical devices results in several advantages, such as stronger field coupling [30], higher coherence and longer lifetime [31], and long distance routing capability on chip [32, 33]. In this work, building on these recent developments, we experimentally distribute quantum information using phonons in a waveguide. Our device is composed of an optomechanical cavity, which acts as the single phonon source and detector, that is connected to a single-mode phononic waveguide. Using this device we then create a time-bin entangled state of a pair of traveling phonons. Furthermore, we unambigu-

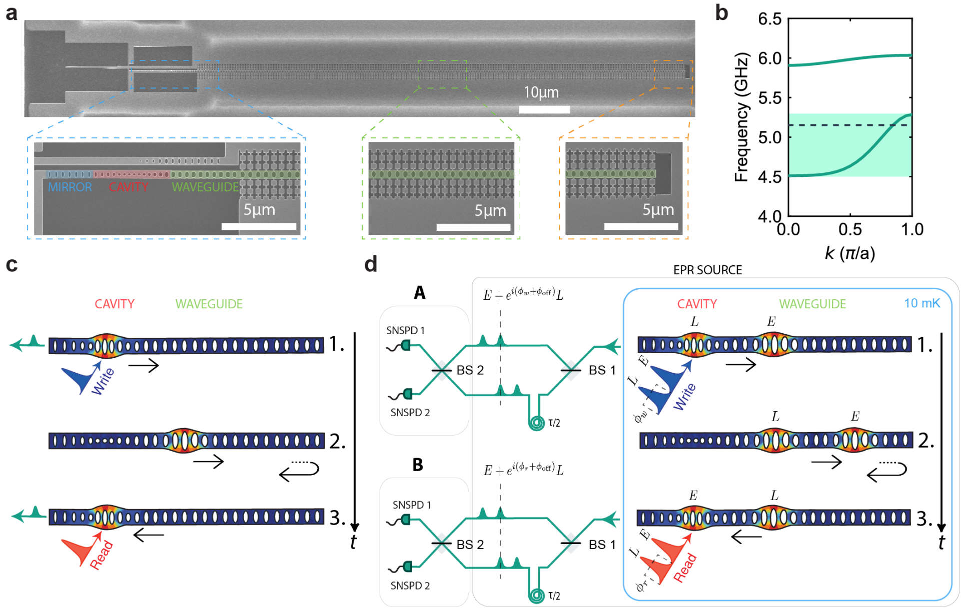

Figure 4.1: **Device and experimental setup.** a) Scanning electron microscope (SEM) image of the device. Bottom left: photonic and phononic mirror (highlighted in blue), optomechanical cavity (red) and initial part of the phononic waveguide, which also acts as a photonic mirror (green). Bottom center: section of the phononic waveguide. Bottom right: free standing end of the waveguide, which acts as a mirror for the phonons. b) Band diagram of a unit cell of the waveguide showing its single mode design for the symmetric mode, with the frequency of interest depicted by the black dashed line (see the SI section 1). c) The control pulses (write and read) are sent to the cavity to create 1. and retrieve 3. the mechanical excitation. The green pulses depict the scattered Stokes and anti-Stokes photons. In 2. the mechanical excitation travels in the waveguide (round-trip time of τ). d) Simplified schematics of the time-bin entangling protocol. 1. Creation of the entangled state between the Early (E) and Late (L) Stokes-scattered photons and the traveling phononic excitation in the waveguide. The pulses have a time delay of $\tau/2$ and are depicted here in shorter succession than in the experiment for clarity of the drawing. 2. Propagation of the mechanical qubit in the waveguide, with the reflection at the end. 3. Mapping of the phononic onto a photonic state in order to verify the entanglement. The boxes conceptually divide Einstein–Podolsky–Rosen (EPR) source, and measurements setups A and B (which are the same experimental setup at different times t), used to create and detect the entangled state. SNSPDs are superconducting nanowire single-photon detectors. The arrows in c) and d) represent the direction of propagation of the mechanical excitations and the time axis is shown by the vertical black arrow.

ously show the non-classical correlations between an optical and the traveling phononic qubit, by violating a Bell-type inequality [34–36].

4.2. METHODS

Our device consists of a single mode optomechanical cavity connected to a phononic waveguide (cf. Fig. 4.1a), similar to a previous design [33]. The cavity is used as a source and detector for mechanical excitations, controlled with telecom-wavelength optical pulses (via Stokes and anti-Stokes scattering [37]). We engineer the photonic and phononic band structure of the different parts of the device such that the mechanical mode extends into the waveguide while the optical mode remains fully confined in the cavity (see the Supplementary Information (SI) for more details on the device design). The waveguide has a free standing end, which acts as mirror for the traveling phonons and effectively forms a Fabry-Pérot cavity. The coupling between the single mode cavity and this Fabry-Pérot cavity results in a hybridization of the cavity and waveguide modes into (almost) evenly spaced modes separated by the free spectral range (FSR) of the Fabry-Pérot cavity. The FSR is determined by the length of the waveguide and by the group velocity of the phonons. We design the waveguide to be single mode for the symmetry of the mechanical mode used in this work (the band structure is shown in Fig. 4.1b).

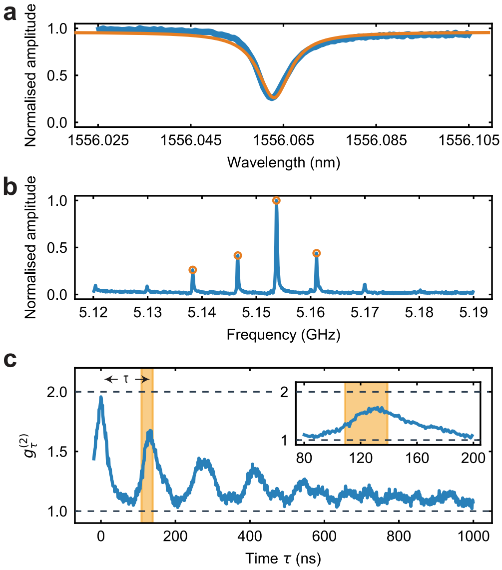

Figure 4.2: **Initial characterization.** a) Optical spectrum of the device measured in reflection. b) Mechanical spectrum measured using optomechanically induced transparency (OMIT). c) Second order correlations of a thermal state for different time delays between the SNSPDs click events τ. The series of equally spaced peaks shows that when the thermal mechanical excitations leave the optomechanical cavity, they are reflected from the end of the waveguide and then return back into the cavity. The inset is a close-up of the area around the first peak. The shaded regions show the delay and control pulse area chosen for all the subsequent experiments in this work ($\tau = 126$ ns, with a time length of 30 ns).

In order to create a propagating mechanical excitation we use a blue-detuned write (Stokes) control pulse, which via a two-mode squeezing interaction, creates entangled photon-phonon pairs. The phononic excitation created in the cavity then leaks into the waveguide, is reflected by the end mirror and returns back periodically to the cavity after a round-trip time τ. Finally, to retrieve the mechanical state, a red-detuned read (anti-Stokes) control pulse enables the optomechanical beam-splitter interaction which maps the mechanical into a photonic excitation (see Fig. 4.1c for details on the scheme). To create a time-bin encoded mechanical qubit using this scheme, we first place the device in a dilution refrigerator at 10 mK, initializing the mechanical mode in its quantum ground state. We then send two blue-detuned write pulses separated by $\tau/2$ to the device in the cryostat, as shown in Fig. 4.1d, and send the resulting scattered photons into an optical interferometer. One arm is delayed with respect to the other one by $\tau/2$ to overlap the scattered photons in time. The reflected control pulses are suppressed using optical filters (see SI) and the resulting interferometer output signals are detected on two superconducting nanowire single-photon detectors (SNSPDs). By operating in the low pulse energy regime (low optomechanical scattering probabilities, p_w), the two identical write pulses create the optomechanical state

$$\left|\psi_0\right\rangle \propto |0000\rangle + \sqrt{p_\mathrm{w}}\big(|1010\rangle_{E_oL_oE_mL_m} + e^{i\phi_\mathrm{w}}|0101\rangle_{E_oL_oE_mL_m}\big) + \mathcal{O}(p_\mathrm{w}), \tag{4.1}$$

where E_m (L_m) and E_o (L_o) indicate the “Early" (“Late") mechanical and optical state, and ϕ_w is the phase difference between the two “Early" and “Late" write pulses, set with an electro-optical modulator (EOM) (see SI section 4 for more details). By overlapping these “Early" and “Late" photons on a beamsplitter, after passing through the unbalanced interferometer, we erase any “which path" information. Consequently, by detecting a Stokes-scattered photon from the overlapped “Early" and “Late" pulses on one of the detectors, we perform an entanglement swapping operation resulting in an heralded entangled state between the “Early" and “Late" traveling mechanical excitations

$$\left|\psi_m\right\rangle \propto |10\rangle_{E_mL_m} \pm e^{i(\phi_\mathrm{w}+\phi_\mathrm{off})}|01\rangle_{E_mL_m}, \tag{4.2}$$

with the plus (minus) sign resulting from a detection event in either detector. The phase ϕ_off is a fixed phase difference between the two arms of the unbalanced interferometer (SI sections 5 and 6). Note how the state is maximally entangled in the Fock-basis, which at the same time serves as a mechanical qubit.

The entangled phonon state travels through the waveguide and after re-entering the cavity can be mapped onto an optical state with the red-detuned anti-Stokes control pulses. The entire 4-mode optical state of write and read scattered photons can be expressed as:

$$\left|\psi_{AB}\right\rangle \propto \big[(1+e^{i(\phi_\mathrm{w}+\phi_\mathrm{r}+2\phi_\mathrm{off})})(\hat{a}^\dagger_{\mathrm{w},1}\hat{a}^\dagger_{\mathrm{r},1} - \hat{a}^\dagger_{\mathrm{w},2}\hat{a}^\dagger_{\mathrm{r},2}) + i(1-e^{i(\phi_\mathrm{w}+\phi_\mathrm{r}+2\phi_\mathrm{off})})(\hat{a}^\dagger_{\mathrm{w},2}\hat{a}^\dagger_{\mathrm{r},1} + \hat{a}^\dagger_{\mathrm{w},1}\hat{a}^\dagger_{\mathrm{r},2})\big]|0000\rangle \tag{4.3}$$

where $\hat{a}^\dagger_{\mathrm{w},1}$ ($\hat{a}^\dagger_{\mathrm{w},2}$) and $\hat{a}^\dagger_{\mathrm{r},1}$ ($\hat{a}^\dagger_{\mathrm{r},2}$) are the creation operators of the photon coming from the write pulse and read pulse, on detector 1 (2). An additional phase ϕ_r is applied only on the “Late" read pulse, which is used to rotate the readout basis. Here the read pulses map the mechanical state onto the optical mode and hence this state is a direct result of the entanglement between the photonic and the traveling phononic qubit. For verifying the mechanical entanglement of Eq. 4.2 we use $\phi_\mathrm{r} = 0$.

In order for our protocol to work, we need to fulfill several basic requirements. For both the phononic and photonic qubits, for example, we have to create orthogonal states (the basis), and thus for the time-bin encoding we have to be able to unambiguously distinguish the “Early" and “Late" states. Experimentally we implement this by realizing a ~100 µm long phononic waveguide and by choosing the control pulse length as 30 ns, given a simulated group velocity in the waveguide of approx. 2000 m/s. Moreover the thermal occupation of the mechanical mode, mainly given by a small absorption of the control pulses in the optomechanical cavity, has to be $\ll 1$ in order to realize a high-fidelity entangled state. This limits the maximum scattering probability of the write and read control pulses (see SI section 3).

4.3. RESULTS

To characterize the device we first measure its optical properties at 10 mK and observe a resonance at $\lambda \approx 1556.06$ nm with FWHM of $\kappa/2\pi \approx 1.05$ GHz (intrinsic loss rate $\kappa_\mathrm{i}/2\pi = 250$ MHz, see Fig. 4.2a). We use the optomechanically induced transparency (OMIT) technique to measure the mechanical spectrum of the device [33, 38]. As can be seen in Fig. 4.2b, the hybridized modes exhibit a clean, evenly spaced spectrum with FSR $\approx$ 8 MHz. We choose the most prominent mechanical resonance in Fig. 4.2b (around 5.154 GHz) as the frequency to which we detune the lasers with respect to the optical resonance in order to address Stokes and anti-Stokes interactions. We further use the rate of Stokes-scattered photons from a 30 ns long pulse to determine the equivalent single photon optomechanical coupling rate [39] of the ensemble of optomechanically coupled modes at $g_0/2\pi \approx 380$ kHz.

In order to measure the round-trip time and coupling between the cavity and waveguide we pump our device with a continuous red-detuned laser. Due to the non-zero optical absorption in the device, the continuous laser creates a thermal mechanical population inside the optomechanical device that leaks into the phononic waveguide and reflects from the free standing end before returning back into the optomechanical cavity. The same red-detuned laser then maps the mechanical state onto a photonic state and we measure the two-photon detection coincidence with varying delays between two events. This measurement allows us to obtain the intensity correlation $g^{(2)}_\tau$ of the mechanical thermal state in the optomechanical cavity, as can be seen in Fig. 4.2c. The coincidence rate is normalized to the single photon click rates. For zero time delay we find a $g^{(2)}_{\tau=0} \approx 2$, as expected for a thermal state. The correlation drops down to 1, as the thermal state leaves the optomechanical cavity into the waveguide resulting in uncorrelated clicks, and then periodically increases again when the thermal population returns back to the cavity [33]. We use this measurement to determine the round-trip time for an excitation in the waveguide, $\tau = 126$ ns.

Note that the decay in the peak values is mainly due to the small difference in FSR between the mechanical modes [33], as well as the short mechanical lifetime $T_1 \approx 2.2\,\mu$s (see section 7 in the SI for more details). From the FWHM of the peak centered around zero time delay in Fig. 4.2c we can extract the packet time duration of $\approx$ 30 ns. To match the packet time length, we then choose to use 30 ns-long Gaussian write and read pulses in all experiments.

As a next step we verify our ability to distinguish between multiple phonon wavepackets. To do this, we measure the photon cross-correlations in a double write / read pulse sequence, in which we create and measure the second wavepacket after half of the round trip time $\tau/2 \approx 63$ ns. In this experiment, the delay arm of the interferometer is disconnected, such that the pulses do not interfere. Two write and two read pulses are sent to the device with a relative delay between them of $\tau/2$, as shown in Fig. 4.3a. In all the

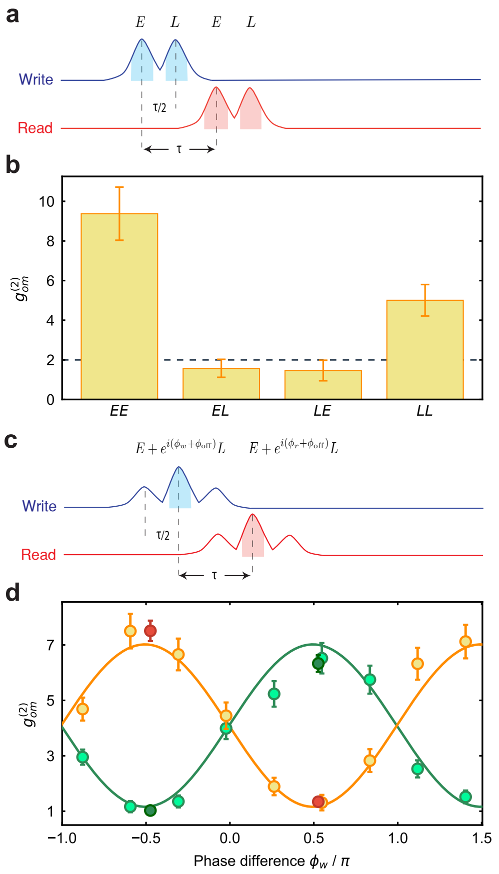

Figure 4.3: **Time-bin phononic entanglement.** a) Pulse scheme for a double write / read pulse cross-correlation measurement. In this experiment the delayed arm of the interferometer is open. The two write and two read pulses are called “Early" (E) and “Late" (L) and are delayed by $\tau/2$. The shaded areas are the regions from which the coincidences are gathered (time length of 30 ns). b) Extracted values of the cross-correlation $g^{(2)}_{\text{om}}$ measured for the four combinations of write / read pulses. The correlations for EE and LL are significantly exceeding the classical threshold of 2 (dashed line), while the other two combinations of EL and LE only exhibit classical correlations. c) Control pulse scheme to create and detect time-bin phononic entanglement at the interferometer. The “Early" pulse passing through the delay arm of the interferometer and the “late" pulse passing through the direct arm of the interferometer overlap in time. d) Second-order correlations of the Stokes and anti-Stokes photons as a function of the relative phase difference ϕ_{w} between the “Early" and “Late" write pulses. The events for same detector coincidences are shown in green, while different detectors coincidences are orange. Two additional measurements, red and dark green points, are performed at two phase settings to obtain more statistics for verifying the phononic entanglement. The maximum violation is $R = 0.72 \pm 0.06$, almost 5 SDs below the classical threshold of 1. All error bars are one SD. The solid curves are the joint fit of the data and serve as guide to the eye.

pulsed measurement we set a waiting time between trials of ~7 T_1 (15 µs) to let the mechanical modes thermalize to the ground state (see SI section 3). The energy of each pulse is 26 fJ (112 fJ) for the write (read), probabilistically scattering photons through the

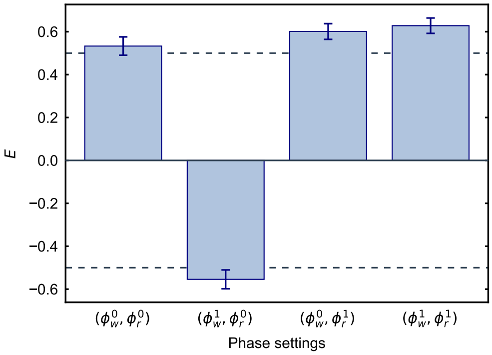

Figure 4.4: **Bell test.** The values of the correlation coefficients E grouped for the four ideal phase settings of the CHSH inequality, which are $(\phi_\mathrm{w}^0, \phi_\mathrm{r}^0) = (\phi_0 - \pi/4, 0)$, $(\phi_\mathrm{w}^1, \phi_\mathrm{r}^0) = (\phi_0 + \pi/4, 0)$, $(\phi_\mathrm{w}^0, \phi_\mathrm{r}^1) = (\phi_0 - \pi/4, \pi/2)$ and $(\phi_\mathrm{w}^1, \phi_\mathrm{r}^1) = (\phi_0 + \pi/4, \pi/2)$. The total number of events for each phase setting is ∼400. The dashed lines are the threshold for each correlation coefficient to violate the inequality. From these values we obtain $S = 2.32 \pm 0.08$, which violates the inequality by 4 SD. All errors are one SD.

Stokes (anti-Stokes) process, with a probability of $p_\mathrm{w} = 0.2\%$ ($p_\mathrm{r} = 0.7\%$). The measured thermal phonon number of the mechanical resonator after applying the four pulses are 0.022 ± 0.002, 0.040 ± 0.003, 0.066 ± 0.003 and 0.095 ± 0.004 (cf. SI section 3). We measure the second order cross-correlation between the four combinations of “Early" and “Late" write and read pulses, $g_\mathrm{cc}^{(2)}$ as shown in Fig. 4.3b. We observe strong non-classical correlations of $g_\mathrm{cc}^{(2)} = 9.4 \pm 1.3$ between “Early"-“Early" and $g_\mathrm{cc}^{(2)} = 5.0 \pm 0.8$ between “Late"-“Late" combinations, while the other two combinations show only classical correlations of $g_\mathrm{cc}^{(2)} = 1.5 \pm 0.5$ [40]. Note that the lower value for the “Late"-“Late" combination, with respect to “Early"-“Early", is caused by the small accumulated thermal population induced by the pulses (see SI section 3 for more information).

We now proceed to verify that we have created a traveling mechanical qubit encoded in a superposition of “Early" and “Late" time bins, by sending the same pulse sequence to the device, with the delay arm of the interferometer connected. This way the part of the “Early" scattered photons that pass through the delay line and the part of the “Late" scattered photons that pass though the direct arm are overlapped in time, such that a single photon detection event after BS2 projects the mechanical state in Eq. 4.2. The pulse sequence at the detectors is shown in Fig. 4.3c, where the highlighted peaks are the overlapped and interfered “Early" and “Late" pulses, from which we detect the photons. We sweep the excitation phase ϕ_w and measure the second order correlation $g^{(2)}$ between the write and read photon detection events occurring at the same (green) or different (orange) output of BS2, displayed in Fig. 4.3d. The periodic dependence on the phase demonstrates the coherence of the generated entangled state. To show that the state shown in Eq. 4.2 is indeed entangled, we use an entanglement witness, denoted by R, designed for optomechanical systems [41], as previously used in [42]. After sufficient integration we gather more than 500 coincidence events and we obtain $R = 0.72 \pm 0.06$, violating the classical threshold of 1 by almost 5 standard deviations.

To unambiguously demonstrate the non-classical character of the traveling phononic qubit and the photon state in Eq. 4.3, we perform a Bell-type test using the CHSH inequality [34]. We define the correlation coefficients

$$E(\phi_\mathrm{w},\phi_\mathrm{r}) = \frac{n_{11}+n_{22}-n_{12}-n_{21}}{n_{11}+n_{22}+n_{12}+n_{21}}, \tag{4.4}$$

where n_{kl} are the events where detector k clicked after a write pulse (station A in Fig. 4.1d) and detector l after a read pulse (station B in Fig. 4.1d). The inequality then states that

$$S = |E(\phi_\mathrm{w}^0,\phi_\mathrm{r}^0) - E(\phi_\mathrm{w}^1,\phi_\mathrm{r}^0) + E(\phi_\mathrm{w}^0,\phi_\mathrm{r}^1) + E(\phi_\mathrm{w}^1,\phi_\mathrm{r}^1)| \le 2. \tag{4.5}$$

The maximum violation is expected to occur for $(\phi_\mathrm{w}^i = \phi_0 + (-1)^{i+j}\pi/4,\ \phi_\mathrm{r}^j = (\pi/2)^j)$, with $i, j = \{0,1\}$, and where $\phi_0 = 2\phi_\mathrm{off} + \pi/2 \approx 1.0\pi$ is the phase for which the correlation coefficient is zero (with negative slope). We choose phase settings with a small offset compared to these values to have the highest possible value of S for our setup (see SI section 6 for more details). To violate the CHSH inequality we lower the energy of the write pulses slightly, such that we use 15 fJ (112 fJ) for the write (read) pulse, with a scattering probability of $p_\mathrm{w} = 0.13\%$, $(p_\mathrm{r} = 0.7\%)$. The measured thermal populations for the four pulses are then 0.027 ± 0.003, 0.038 ± 0.004, 0.055 ± 0.002 and 0.090 ± 0.004 (see SI section 3).

From the correlation coefficient we define the visibility as $V = max(|E|)$. We first perform an additional measurement at the phase of maximum visibility obtaining $V = 0.82 \pm 0.04$, which is considerably higher than the threshold of $V > 1/\sqrt{2} \approx 0.7$ required for violating the CHSH inequality. We then measure at the four optimal phase settings for the Bell test (see Fig. 4.4) obtaining a value of $S = 2.32 \pm 0.08$, which corresponds to a violation of the CHSH inequality by 4 standard deviations. The rate of events for this measurements is around 30 per hour of integration, allowing us to measure the full data set for the violation within 56 hours.

4.4. DISCUSSION

We have unambiguously demonstrated a traveling phononic qubit in the form of a time-bin entangled state, which can be used to distribute quantum information on a chip. The routing process is shown to be fully coherent, which is of fundamental importance for routing quantum information and interconnecting quantum devices. While we limit ourselves to show two-mode entanglement, the same device can be used with up to four modes, given the round-trip time and mechanical packet length, or more by using a longer waveguide. Additionally, the quantum state can be retrieved at arbitrary multiples of the round trip time, allowing for long storage and controlled emission of the state. Moreover, as the phononic entangled state travels down the waveguide, a straightforward extension using our device will allow to distribute quantum entanglement to different points on a chip. We have chosen to use a waveguide design with a lifetime of only $T_1 \approx 2.2\,\mu\mathrm{s}$, limiting the maximal phonon traveling length for this devices to around 3 mm. By adding additional phononic shielding, this can however easily be extended to meter scales as the device's lifetime increases to several milliseconds [31].

The demonstrated time-bin entanglement between a photonic and a traveling phononic qubit, verifying their non-classical correlations by violating a CHSH inequality, underlines the suitability of the phononic system as a DLCZ unit cell [43]. In this work, the fidelity of the entangled state is limited by residual optical absorption, which can be further reduced by up to an order of magnitude through optimized fabrication, allowing for state retrieval efficiencies of up to 30 % [40].

The ability to excite, guide, and detect traveling phonons is the basic toolbox for phonon manipulation on-chip, enabling a completely new field using traveling mechanical modes in the quantum regime. Together with a phononic phase modulator [44] and beamsplitter, this work will lead to full coherent control of guided phonons and paves the way to novel quantum acoustic experiments. Moreover, our measurements highlight the potential of phonons as ideal candidates for realizing quantum networks and repeaters, as well as for on-chip distribution of quantum information in hybrid quantum devices, for example for interfacing microwave superconducting circuits with spin quantum memories [24] or to couple on-chip qubits using electron-phonon interaction in solids [22].

Acknowledgments We would like to thank Matteo Lodde, Andrea Fiore and Bas Hensen for valuable discussions. We further acknowledge assistance from the Kavli Nanolab Delft. This work is financially supported by the European Research Council (ERC CoG Q-ECHOS, 101001005) and is part of the research program of the Netherlands Organization for Scientific Research (NWO), supported by the NWO Frontiers of Nanoscience program, as well as through Vidi (680-47-541/994) and Vrij Programma (680-92-18-04) grants. R.S. acknowledges funding from the European Union under a Marie Skłodowska-Curie COFUND fellowship.

Conflict of interests: The authors declare no competing interests.

Author contributions: A.Z., R.S. and S.G. devised and planned the experiment. A.Z., N.F, R.B. simulated and designed the device. N.F. fabricated the sample, A.Z. and N.F. built the setup and performed the measurements. A.Z., N.F., R.S. and S.G. analyzed the data and wrote the manuscript with input from all authors. E.V. and S.G. supervised the project.

Data Availability: Source data for the plots are available on Zenodo.

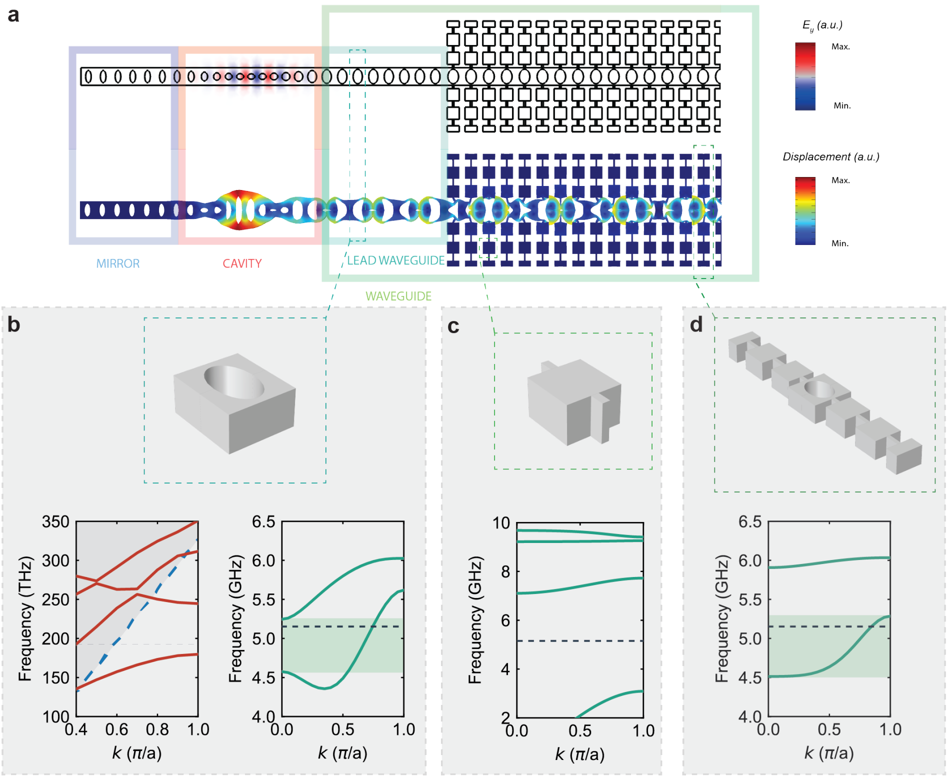

Figure 4.5: a) Optical (top) and mechanical (bottom) eigenmode simulations of the full structure. The mechanical mode shown is a cavity-waveguide supermode. Note how the optical mode is confined in the cavity, while the mechanical mode is extended into the waveguide. b) Lead waveguide unit cell, with its optical (left) and mechanical (right) band diagram shown below. The gray area for the optical part depicts the light cone, delimited by the blue dashed line. c) Shield unit cell, used in the clamps to connect the waveguide to the substrate and its mechanical band diagram below. d) Unit cell of the shield-clamped waveguide, with its band structure shown underneath. In all plots the horizontal black dashed lines are the working optical and mechanical frequencies, while the highlighted area are the single mode regions of the waveguides.

4.5. SUPPLEMENTARY INFORMATION

DESIGN

Our device, which is shown in Fig. 4.1a, is composed of three distinct parts: a mirror, a cavity and a waveguide. To design the device we use finite element simulations (COMSOL) and engineer a suspended silicon nanobeam (width 529 nm and thickness of 250 nm) with elliptical holes patterned into it. The hole dimensions are varied along the beam in order to realize the different parts of our device. The finite element simulation of the full structure is shown in Fig. 4.5a. The left part (blue) is a phononic and photonic mirror, with the respective bandgaps at the resonance frequencies of the cavity. The optomechanical cavity, acting as the source and detector for phonons, has a co-localized single optical mode in the telecom band and a single mechanical mode around 5 GHz, similar

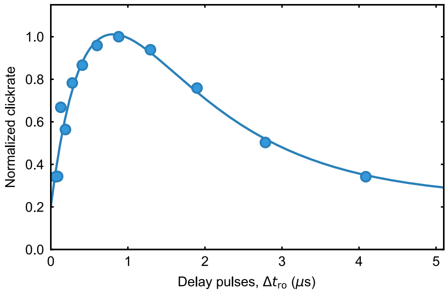

Figure 4.6: Normalized clickrates from the probe pulse that gives an uncalibrated measure of the thermal population in time. The delay between pump and probe pulse is Δt_{ro}. We extract $T_1 \approx 2.2\,\mu s$, by fitting the data (solid curve).

to [37, 45]. The phononic waveguide (green) is a single mode phononic waveguide for the symmetric mechanical breathing mode in the frequency range of interest (around 5 GHz). Only this mode is considered, as it matches the mechanical mode shape of the cavity, enabling large mechanical coupling between the cavity and the waveguide. The first part of the waveguide, referred to as the “lead waveguide" in the figure, acts as a photonic mirror having a bandgap in the telecom range. The unit cell of this part, together with its optical and mechanical band structure, are shown in Fig. 4.5b and c, respectively. As a result of our design, the optical mode stays confined inside the optomechanical cavity, while the mechanical mode is guided with very little loss through the waveguide, as shown in Fig. 4.5a. The second part of the waveguide is connected to the substrate via phononic shield clamps for structural support. The band diagram of the phononic shield together with the unit cell are shown in Fig. 4.5d and e. The shield minimizes the mechanical loss from the waveguide to the substrate, fully confining the mechanical mode in the waveguide. The design of the waveguide with clamping differs from the lead waveguide to avoid perturbations of its band structure. The unit cell shape of this waveguide and the band structure are shown in Fig. 4.5f and g. Note how the mode in the waveguide has an approximately linear dispersion in the range of interest.

MECHANICAL LIFETIME

To measure the mechanical lifetime of the device (T_1) we send a series of red-detuned double pulses with the interferometer delay arm open. The strong first pulse creates, via optical absorption, a relatively large thermal population that is probed by the second pulse, and which is delayed by time Δt_{ro}. With this pump-probe experiment we can access the uncalibrated thermal population of the device in time [40] (see Fig. 4.6). From the exponential decay we measure $T_1 \approx 2.2\,\mu s$, much longer than the 126 ns delay used in the experiments. We set the time between trials in all experiments equal to 15 μs, to let the population fully decay. Note that while the device is intentionally designed to have a short lifetime in order to allow for a high repetition rate of the experiment, previous work with similar structures has reported lifetime up to 5.5 ms [33]. We would also like to note that an additional phononic shield period at the mirror side (blue part in Fig. 4.1a) does

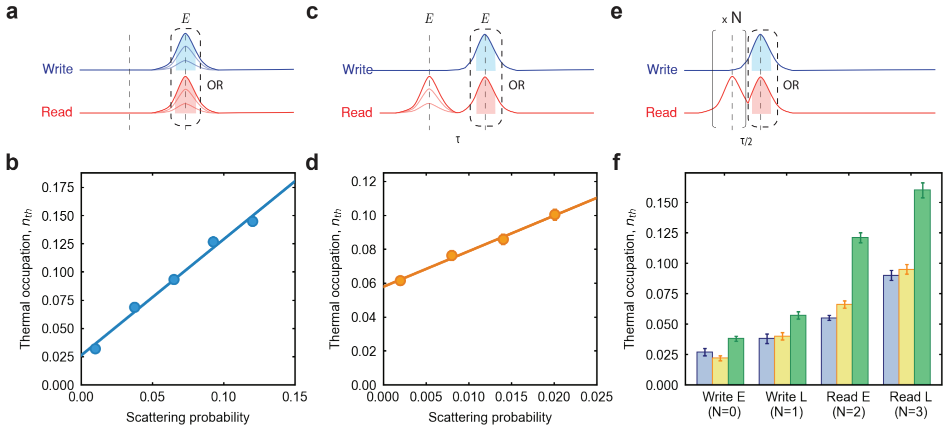

Figure 4.7: a) Pulse scheme for the thermal occupation measurement. We send trains of pulses alternating between write and read to measure the asymmetry in their scattering probabilities. The opaque pulses represents the sweep in energy of the pulse, while the shaded area is the integration region. b) Thermal occupation as a function of the measured scattering probability for a single pulse (equivalent to the read "Early" situation in the experiments). The solid line is a linear fit to the data. c) Same as a) for the two pulse calibration of the thermal occupation. Note how the read pre-pulse is only for heating the mechanical mode and its energy is swept. The alternating pulses used to measure the n_{th} are in the black dashed box and have fixed energy. d) Thermal occupation of the second pulse (read "Early" in the experiment) as a function of the measured scattering probability of the first pulse (write "Early" in the experiment). Note how the offset in this measurement strongly depends on the energy of the second pulse, which in this case is 225 fJ (twice the energy of the single read pulses used in the phononic entanglement experiment of Fig. 4.3 in the main text). The solid line is a linear fit to the data. e) Same as a) but for multiple pre-pulses. We send N pre-pulses (with $N = (0,1,2,3)$ for write E, write L, read E and read L, respectively) and use the alternating pulses in the dashed black box to measure the thermal population. Each pulse has the energy used in the experiments. f) Measured thermal occupation for the four pulses used in the experiments. In blue for the scattering probabilities used in the measurements for the additional phononic entanglement data and Bell test (Fig. 4.4 in the main text), in orange for the double pulse cross correlation and the phononic entanglement with the sweep in ϕ_{w} (Fig. 4.3 in the main text) and in green for the phase calibration (section 4.5). All error bars are one standard deviation.

not increase the lifetime any further. The increase in thermal population for short delays ($\Delta t_{ro} < 1\,\mu\mathrm{s}$) is given by the delayed absorption [37].

THERMAL OCCUPANCY OF THE MECHANICAL MODE

In order to determine the thermal occupation of the mode of interest we send trains of alternating write and read pulses to the device, as shown in Fig. 4.7a. From the asymmetry in clickrates of these pulses we can calculate the thermal mechanical population n_{th}. We adjust the scattering probability by sweeping the energy of the pulses and measure the resulting thermal occupation, see Fig. 4.7b. To further mimic the same heating conditions as in the experiment, without the optomechanically excited coherent population created from the write pulses, we use heating pre-pulses from the read laser. The alternating pulses, used to measure n_{th}, are sent at a delay given by the round-trip time τ and have a fixed energy, while the energy of the pre-pulse is swept. In Fig. 4.7 we show the pulse scheme for these measurements, as well as the thermal occupation at the second pulse (in the experiment the read pulse) as a function of the scattering probability of the

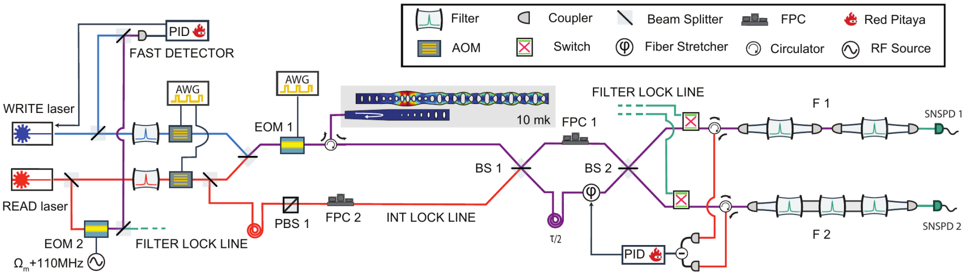

Figure 4.8: Detailed scheme of the setup (see text for more details). AOM are the acousto-optic modulators, AWG the arbitrary waveform generators, EOM the electro-optic modulator, VOA the variable optical attenuator, BS the beamsplitters, and PBS the polarizing BS, FPC the fiber polarization controller and SNSPD the superconducting nanowire single-photon detectors. Ω_m the mechanical frequency. All the components (apart from the free-space filters F 1 and F 2) are fiber based.

first pulse (in the experiment the write pulse). We use the two asymmetry measurements (Fig. 4.7b and d) to choose the single write/read scattering probabilities that will give a total thermal population below 0.1, with a third of this thermal occupation given by the first pulse and the rest by the second (to minimize the effects of delayed heating).

We then measure the values of n_{th} for the pulses used in the experiments. We send heating pre-pulses and use the alternating pulses to measure the thermal population, as drawn in Fig. 4.7e. Each of these pulses has the corresponding energy used in the experiments and all are delayed by $\tau/2$ with respect to each other. In Fig. 4.7f we report the measured thermal occupation for the four pulses of the experiments, for the three sets of scattering probabilities used: in blue the one for the additional phononic entanglement data and the Bell test (Fig. 4.4 in the main text), in orange for the double pulse cross correlation and the phononic entanglement with the sweep in ϕ_w (Fig. 4.3 in the main text) and in green for the phase calibration (section 4.5). Note how the thermal population increases non-linearly with increasing number of pulses due to delayed heating, as is clearly visible in Fig. 4.7.

EXPERIMENTAL SETUP

A sketch of the experimental setup is shown in Fig. 4.8. Two continuous-wave (CW) lasers (write and read) are frequency-locked to one another by detecting the interference between their light on a fast detector (in particular: the light from the write laser and the second order sideband of the read laser generated by EOM 2, which have a frequency difference of 2×110 MHz). The laser light from the CW lasers is filtered to remove GHz noise using fiber filters. The pulses are created by gating the CW light with 110 MHz AOMs, which are driven by an arbitrary waveform generator and the laser pulses are combined on a beam splitter. A phase EOM, driven by another AWG, is used to add a phase offset to the "Late" pulses (to set ϕ_r and ϕ_w). The pulses are then routed to a circulator and to the cryostat, where a lensed fiber allows the coupling to the device's optical waveguide, with efficiency of $\eta_c \approx 50\%$. The light from the device is fed to an unbalanced Mach-Zehnder interferometer, defined by BS 1 and BS 2, where the time delay between the arms is $\tau/2 = 63$ ns. These two BSs have a relative difference in the splitting ratio

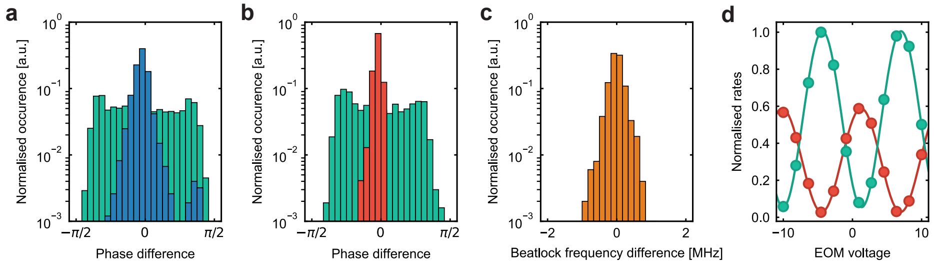

Figure 4.9: a) Occurrence histogram of the phase difference acquired by the write pulses when the interferometer is locked (in blue) and unlocked (in green). The FWHM is $\approx \pi/7$. b) Same as a) for the read pulses, for the case of a locked interferometer (in red) and unlocked (in green). The FWHM here is $\approx \pi/20$. c) Occurrence histogram of the frequency difference of the write and read lasers as from the beatlock. Here the FWHM is ≈ 0.5 MHz. This relative frequency jitter causes a bigger phase difference spread for the write pulses compared to the read ones. d) Normalized count rates of SNSPD1 (red) and SNSPD2 (green) for weak coherent pulses on resonance with the filter cavities. Sweeping the EOM voltage results in the observed interference pattern, which we use to calibrate the phase given by the EOM. In this case the interferometer visibility is $V_{\text{int}} \approx 94\,\%$. Error bars are one standard deviation and are too small to be seen.

of the two output ports smaller than 0.5%, while the losses in both lines are negligible. The interferometer is actively stabilized using a home-built fiber stretcher controlled by a PID loop that uses the signal from pulses coming from the INT LOCK LINE (see section 4.5 for more details). The polarization of the two arms are matched at BS 3 using the fiber polarization controller 1 (FPC 1). The light from the interferometer is filtered by two sets of free space optical Fabry-Pérot cavities (F 1 and F 2) with suppression ratios of the strong control pulses of about 115 dB (F 1) and 112 dB (F 2). This gives a pump pulse leakage rate of 2×10^{-7} and 4×10^{-7} photons per repetition from the write pulse and 1.4×10^{-6} and $2.6 \times 10{-}6$ from the read pulse, for F 1 and F 2, respectively. Note that the two sets of filters have a CW efficiency of transmission at resonance of ~65%. Due to the different total bandwidth of 40 MHz (80 MHz) for F 1 (F 2), the relative transmission efficiency of the pulses is about 40% lower for F 1 using 30 ns long pulses. The experiment is paused and the filters are locked on resonance with the cavity every 8 s, flipping the switches to use the CW signal from the FILTER LOCK LINE (detectors not shown). The average time needed to lock the two filter setups is about 1 s. The signal photons are detected using superconducting nanowire single photon detectors (SNSPD).

PHASE STABILITY

A fundamental part of the experiment is the phase difference acquired by the pulses in the unbalanced Mach-Zehnder interferometer, which has to be actively locked. In order to do so, the two strong control pulses from the read laser line are routed via a 90:10 BS to a long delay line (≈1 μs of delay) to have them temporally spaced from the signal. A PBS is inserted in the line to minimize polarization drifts. After passing through the unbalanced interferometer, the pulses are reflected by the first cavity of both filter setups and are routed by circulators to a balanced detector. A sample&hold board (not shown in Fig 4.8) is used to select the correct pulse and feed it as the input voltage to a Red Pitaya board. The output of the board is amplified (not shown) and sent to the fiber stretcher.

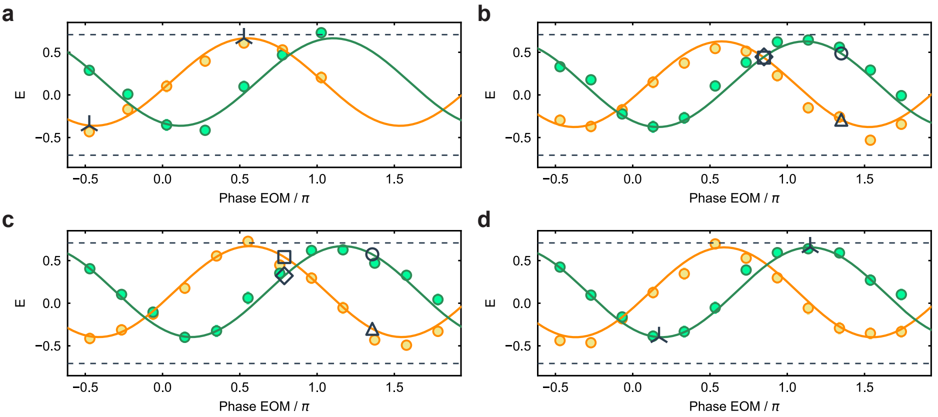

Figure 4.10: a) Correlation coefficients E, sweeping ϕ_w and for $\phi_\mathrm{r} = 0$ (in orange) and $\phi_\mathrm{r} = \pi/2$ (in green), for higher pulse energies with respect to the main text. The black markers (tri) are at the chosen phases for the additional measure of R. b), c) Same as a) for the calibration of the phases for the Bell test. The chosen points differ from the optimal theoretical points of $\phi_0 \pm \pi/4$ by no more than $\approx \pi/20$. The black markers are square, triangle, diamond and circle for the CHSH point $(\phi^0_\mathrm{w}, \phi^0_\mathrm{r})$, $(\phi^1_\mathrm{w}, \phi^0_\mathrm{r})$, $(\phi^0_\mathrm{w}, \phi^1_\mathrm{r})$ and $(\phi^1_\mathrm{w}, \phi^1_\mathrm{r})$ respectively. d) As reported in a) for the additional measurement of R with $\phi_\mathrm{r} = \pi/2$. All errors are one standard deviation and are too small to be seen. The small asymmetry in the value of E around zero is a result of the different filter setup efficiencies (see section 4.5).

The Red Pitaya runs a PID program [46] and the feedback loop is ultimately limited by the bandwidth of the fiber stretcher (approx. 20 kHz).

The phase stability can be measured by tracking the voltage of the locking pulse on the balanced detector. In Fig. 4.9a (b) we plot the occurrence histogram of the phase difference acquired passing the interferometer for the write (read) pulses, in the case the interferometer is locked (in blue (red)), or unlocked (in green). The FWHM are $\approx \pi/7$ for the write and $\approx \pi/20$ for the read pulses. This phase spread is the same for the Stokes (anti-Stokes) scattered photons. Note that the FWHM of phase difference for write and read pulses are different, since the phase acquired by the write laser pulse also depends on the relative frequency jitter of the two lasers. This will only affect the pulses from the write laser since the lock pulses are generated from the read laser. This frequency jitter is reported in Fig. 4.9c, where the occurrence histogram of the frequency difference from the beatlock is shown. Here the FWHM is around 0.5 MHz.

We use FPC 2 to balance the lock signal from the INT LOCK LINE at the balanced detector. We then lock the interferometer and use the first order interference from very weak pulses from the write laser, on resonance with the filter cavities, to measure the interferomenter visibility. We set the EOM voltage to the maximum visibility point and maximize it using FPC 1 (i.e. we align the polarization of the signal) while compensating with FPC 2 for the lock pulses. A typical interference pattern is shown in Fig. 4.9d. We report an average interferometer visibility of $V_\mathrm{int} \approx 94\,\%$ during the whole experiment.

PHASE CALIBRATION

To perform the measurements in the main text we need to first accurately calibrate the phase setting. This is done by performing a measurement of E while sweeping ϕ_w and for two settings of ϕ_r. Here we use higher pulse energies with respect to the actual measurement reported in the main text, such that the scattering probability increases at the expense of having a lower value of E. We use 90 fJ (225 fJ)) for the write (read) pulses, which gives $p_\mathrm{w} = 0.6\%$, $p_\mathrm{r} = 1.4\%$. With these settings we obtain more than 200 events per point in about 30 minutes. Fig. 4.10 shows several such calibration measurements for:

- the additional measurement of the R value (Fig. 4.10a),
- the two runs of integration for the Bell test (Fig. 4.10b, c)
- and for a final measure of R with $\phi_\mathrm{r} = \pi/2$ (and to check that the phase difference during the second run of integration for the Bell test is small, Fig. 4.10d).

The values in orange are for $\phi_\mathrm{r} = 0$, while $\phi_\mathrm{r} \approx \pi/2$ is shown in green. A small deviation from the desired $\pi/2$ phase difference between the orange and green curves can be seen and the exact values are $\phi_\mathrm{r} = \pi/1.8, \pi/1.9, \pi/1.7, \pi/1.8$, for Fig. 4.10a,b,c,d respectively. For the fits of the two datasets we use a sinusoidal function, which serves as a guide to the eye and to numerically calculate the optimal phase points. For the additional measure of R we simply use the phases where E is maximum and minimum (tri markers, Fig. 4.10a and d). For the Bell test, instead, we use the fit to numerically calculate the expected S value and choose the phases where the expected S is maximum (square, triangle, diamond and circle markers for the CHSH point $(\phi_\mathrm{w}^0, \phi_\mathrm{r}^0)$, $(\phi_\mathrm{w}^1, \phi_\mathrm{r}^0)$, $(\phi_\mathrm{w}^0, \phi_\mathrm{r}^1)$ and $(\phi_\mathrm{w}^1, \phi_\mathrm{r}^1)$ respectively). In doing so, the experimentally obtained values differ slightly from the theoretical optimal point of $\phi_0 - \pi/4$ and $\phi_0 + \pi/4$ by a small margin ε. The value for ε for the data in Fig. 4.10b (c) is $\approx \pi/30$ and $\approx \pi/20$ ($\approx -\pi/40$ and $\approx \pi/20$), respectively. The phase offset ϕ_off is calibrated using the maximum and minimum point of E. We choose this particular calibration method to compensate for eventual drifts in the phase offset (ϕ_off), as well as small inaccuracies of phase difference for two sets of measurements with different ϕ_r. Using light to lock the interferometer at a different frequency and from a different path from that of the signal, gives rise to a (fixed) phase offset ϕ_off in the entangled state (see section 4.5). Note that without an external reference PBS a relative change in the polarization between lock pulses and signal pulses will cause a change in the phase shift ϕ_off. However, in our case, the relative change in ϕ_0 (equivalently for ϕ_off) is less than $\pi/50$ in all four measurements.

To further avoid that phase drifts affect only parts of the datasets, we integrate for one hour at each phase point at a time. We then cycle the chosen phases 4 times for phononic entanglement data (and 12 for the longer integration points), and 16 times for the Bell test.

EFFECT OF NON-CONSTANT FSR

The small dispersion in the waveguide causes a non-constant FSR between the mechanical peaks (see Fig. 4.2b). In Fig. 4.11a we report the histogram of the FSR between the mechanical modes. By using the frequency and amplitude of each mechanical peak in

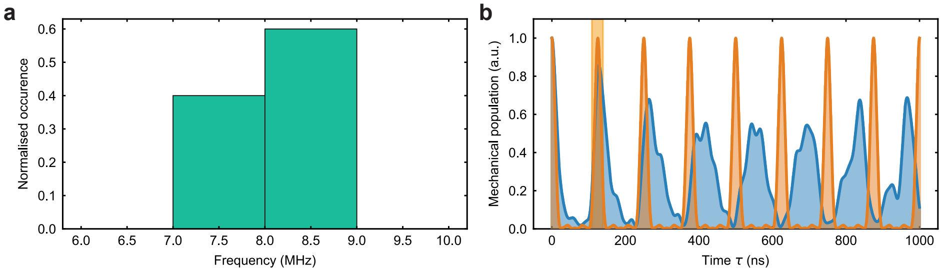

Figure 4.11: a) Normalized histogram of the FSR between the mechanical peaks shown in Fig. 4.2c of the main text with mean value of 8.3 MHz and standard deviation 0.8 MHz. b) The numerically calculated time-domain mechanical population (normalized) for the device spectrum (blue) and ideal spectrum with constant FSR (orange). The shaded area is the same as in Fig. 4.2c.

the spectrum, we numerically simulate the time-domain behavior of the mechanical system and compare it with the simulation of the ideal case (i.e. with perfectly constant FSR) [33]. As can be seen in Fig. 4.11b (blue graph), the mechanical packet is broadened and dimmer after several round-trips due to dispersion of the waveguide compared to the ideal case (orange graph). In this calculation the energy decay of the phonons has not been considered, tracing out any mechanical dissipation, and thus only taking the effect of the dispersion and non-constant FSR into account.

4.6. APPENDIX

In this appendix we report some facts and some *a posteriori* consideration on the experiment reported in this chapter. The idea is to give insights on the challenges encountered on the path to acquire the final dataset.

- To have a constant FSR in the mechanical spectrum it's fundamental to have a structure with as little as possible changes in every period in the direction of propagation. So it is better to have holes of the same size for the lead waveguide and waveguide, and clamps for each period of the waveguide.

- Even in simulation the FSR is not perfectly constant. This can be caused by some residual (little) dispersion of the waveguide and some disturbance of the waveguide band structure caused by strongly coupling the single mode cavity to the waveguide. A longer waveguide with higher group velocity can help to minimize the first contribution, and it will also have the advantage of a larger bandwidth of linear group velocity to be more robust on fabrication imperfection (so that relative shifts in the cavity and the center of the single mode band of the waveguide have less effect on the FSR distribution). However having more modes should be detrimental to the bouncing pattern, since the number of modes with a large contribution to the bouncing pattern is higher and so their non perfect FSR count more. This can be understood in the limit of 2 modes, were the FSR is always "perfect". We use the code of Fig. 4.11 to simulate this effect and we report the result in

Fig. 4.12. It is clear that for longer waveguides, so for higher number of modes, the bouncing efficiency decreases. Too short waveguides (normalized lenght<0.75) are not possible since the phononic packet needs to completely leave the cavity and it does not to overlap with the second pulse sent at $\tau/2$. Decreasing the coupling from cavity to waveguide is non trivial since also the cavity parameters needs to be changed to still have the mechanical and optical mode at the desired frequencies. Also, having too long pulses is non desirable since the effect of the delayed heating will increase.

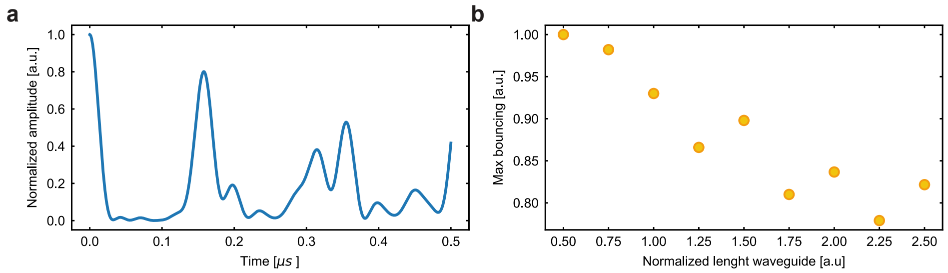

Figure 4.12: a) Bouncing pattern as calculated in Fig. 4.11, for a waveguide with 4 modes centerd at 5 GHz each with amplitude from a gaussian distribution with sigma=20 MHz (that gives a nominal packet length of 50 ns). We add to the nominal FSR=8 MHz (that gives a nominal bouncing time τ = 120 ns) a random small shift in the frequency for each mode (gaussian, with sigma=FSR/10). This numbers are close to the one of the device reported. b) Average of the maximum of the bouncing pattern in function of the normalized length of the waveguide. Each average is 20 repetition of the random gaussian shift. Length of 1 is for 4 modes waveguide as the device reported inthe main text. The length is changed in the simulation modifying the FSR.

- Despite the precision in the nanofabrication, the devices fabricated will most likely have a bigger spread of the distribution of the FSR. We report that having the hole and beam sizes exactly as the simulated ones (within the precision of measurement of the SEM)) is fundamental to have more devices with good bouncing pattern.

- We fabricated 35 chips before having one with devices with sufficiently constant FSR. We characterize 58 devices measuring the one-way coupling from the lensed fiber to the optical waveguide, the optical and mechanical resonances, the lifetime, the thermal occupancy in function of the scattering rates and the thermal $g_\tau^{(2)}$. We then select devices with one-way coupling higher than 55% (20 devices), lifetime longer than 1 µs (12 devices with both condition) and thermal occupancy lower than 0.1 for a fixed 5% scattering probability (5 devices with all 3 conditions). The last selecting criteria was having the maximum of the bounced $g_\tau^{(2)}$ higher than 1.6 (2 devices with all four conditions). We then selected the one with lower thermal occupancy for the experiment reported.

- Here we report another version of Fig. 4.1d, which, despite the less intuitive representation, is closer to the standard figure of a Bell test.

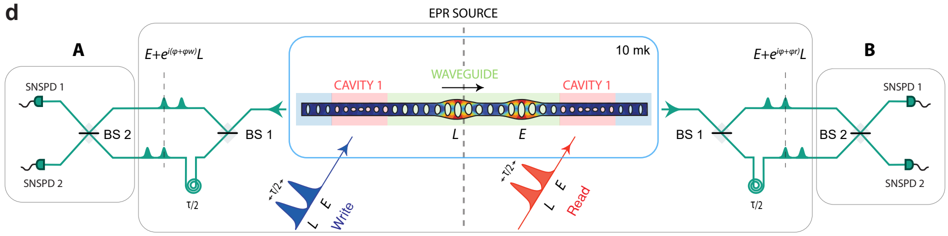

Figure 4.13: Different version of Fig. 4.1d. The vertical dashed line represent a "mirroring" of the device and setup. despite being less accurate and intuitive, it gives a very clear and immediate idea of the EPR pair (Stokes scattered photons and the phonons that traveled in the waveguide once converted in anti-Stokes scattered photons) and of the station A and B.

REFERENCES

[1] F. Arute et al., Quantum supremacy using a programmable superconducting processor, Nature **574**, 505 (2019).

[2] C. Zhong, Z. Wang, C. Zou, M. Zhang, X. Han, W. Fu, M. Xu, S. Shankar, M. H. Devoret, H. X. Tang, and L. Jiang, Proposal for Heralded Generation and Detection of Entangled Microwave-Optical-Photon Pairs, Phys. Rev. Lett. **124**, 10511 (2020).

[3] H. J. Kimble, The quantum internet, Nature **453**, 1023 (2008).

[4] N. Sangouard, C. Simon, H. de Riedmatten, and N. Gisin, Quantum repeaters based on atomic ensembles and linear optics, Rev. Mod. Phys. **83**, 33 (2011).

[5] L. M. K. Vandersypen, H. Bluhm, J. S. Clarke, A. S. Dzurak, R. Ishihara, A. Morello, D. J. Reilly, L. R. Schreiber, and M. Veldhorst, Interfacing spin qubits in quantum dots and donors—hot, dense, and coherent, npj Quantum Inf. **3**, 1 (2017).

[6] M. Wallquist, K. Hammerer, P. Rabl, M. Lukin, and P. Zoller, Hybrid quantum devices and quantum engineering, Phys. Scr. **T137**, 014001 (2009).

[7] J. T. Hill, A. H. Safavi-Naeini, J. Chan, and O. Painter, Coherent optical wavelength conversion via cavity optomechanics, Nature Commun. **3**, 1196 (2012).

[8] A. Vainsencher, K. J. Satzinger, G. A. Peairs, and A. N. Cleland, Bi-directional conversion between microwave and optical frequencies in a piezoelectric optomechanical device, Appl. Phys. Lett. **109**, 033107 (2016).

[9] R. W. Andrews, R. W. Peterson, T. P. Purdy, K. Cicak, R. W. Simmonds, C. A. Regal, and K. W. Lehnert, Bidirectional and efficient conversion between microwave and optical light, Nature Phys. **10**, 321 (2014).

[10] X. Han, W. Fu, C. Zhong, C.-L. Zou, Y. Xu, A. A. Sayem, M. Xu, S. Wang, R. Cheng, L. Jiang, and H. X. Tang, Cavity piezo-mechanics for superconducting-nanophotonic quantum interface, Nature Commun. **11**, 3237 (2020).

[11] G. Arnold, M. Wulf, S. Barzanjeh, E. S. Redchenko, A. Rueda, W. J. Hease, F. Hassani, and J. M. Fink, Converting microwave and telecom photons with a silicon photonic nanomechanical interface, Nature Commun. **11**, 4460 (2020).

[12] W. Jiang, C. J. Sarabalis, Y. D. Dahmani, R. N. Patel, F. M. Mayor, T. P. McKenna, R. Van Laer, and A. H. Safavi-Naeini, Efficient bidirectional piezo-optomechanical transduction between microwave and optical frequency, Nature Commun. **11**, 1166 (2020).

[13] M. Forsch, R. Stockill, A. Wallucks, I. Marinković, C. Gärtner, R. A. Norte, F. van Otten, A. Fiore, K. Srinivasan, and S. Gröblacher, Microwave-to-optics conversion using a mechanical oscillator in its quantum groundstate, Nature Phys. **16**, 69 (2020).

[14] R. Stockill, M. Forsch, F. Hijazi, G. Beaudoin, K. Pantzas, I. Sagnes, R. Braive, and S. Gröblacher, Ultra-low-noise Microwave to Optics Conversion in Gallium Phosphide, Nature Commun. **13**, 6583 (2022).

[15] M. Mirhosseini, A. Sipahigil, M. Kalaee, and O. Painter, Superconducting qubit to optical photon transduction, Nature **588**, 599 (2020).

[16] T. Palomaki, J. Teufel, R. Simmonds, and K. Lehnert, Entangling mechanical motion with microwave fields, Science **342**, 710 (2013).

[17] Y. Chu, P. Kharel, W. H. Renninger, L. D. Burkhart, L. Frunzio, P. T. Rakich, and R. J. Schoelkopf, Quantum acoustics with superconducting qubits, Science **358**, 199 (2017).

[18] R. Blatt and D. Wineland, Entangled states of trapped atomic ions, Nature **453**, 1008 (2008).

[19] P. Delsing *et al.*, The 2019 surface acoustic waves roadmap, J. Phys. D: Appl. Phys. **52**, 353001 (2019).

[20] D. A. Golter, T. Oo, M. Amezcua, I. Lekavicius, K. A. Stewart, and H. Wang, Coupling a surface acoustic wave to an electron spin in diamond via a dark state, Phys. Rev. X **6**, 041060 (2016).

[21] A. Bienfait, K. J. Satzinger, Y. P. Zhong, H.-S. Chang, M.-H. Chou, C. R. Conner, E. Dumur, J. Grebel, G. A. Peairs, R. G. Povey, and A. N. Cleland, Phonon-mediated quantum state transfer and remote qubit entanglement, Science **364**, 368 (2019).

[22] R. P. G. McNeil, M. Kataoka, C. J. B. Ford, C. H. W. Barnes, D. Anderson, G. A. C. Jones, I. Farrer, and D. A. Ritchie, On-demand single-electron transfer between distant quantum dots, Nature **477**, 439 (2011).

[23] S. Hermelin, S. Takada, M. Yamamoto, S. Tarucha, A. D. Wieck, L. Saminadayar, C. Bäuerle, and T. Meunier, Electrons surfing on a sound wave as a platform for quantum optics with flying electrons, Nature **477**, 435 (2011).

[24] T. Neuman, M. Eichenfield, M. E. Trusheim, L. Hackett, P. Narang, and D. Englund, A phononic interface between a superconducting quantum processor and quantum networked spin memories, npj Quantum Inf. **7**, 1 (2021).

[25] M. Aspelmeyer, T. J. Kippenberg, and F. Marquardt, Cavity optomechanics, Rev. Mod. Phys. **86**, 1391 (2014).

[26] S. Barzanjeh, A. Xuereb, S. Gröblacher, M. Paternostro, C. A. Regal, and E. M. Weig, Optomechanics for quantum technologies, Nature Phys. **18**, 15 (2022).

[27] M. K. Ekström, T. Aref, J. Runeson, J. Björck, I. Boström, and P. Delsing, Surface acoustic wave unidirectional transducers for quantum applications, Appl. Phys. Lett. **110**, 073105 (2017).

[28] É. Dumur, K. J. Satzinger, G. A. Peairs, M.-H. Chou, A. Bienfait, H.-S. Chang, C. R. Conner, J. Grebel, R. G. Povey, Y. P. Zhong, and A. N. Cleland, Quantum communication with itinerant surface acoustic wave phonons, npj Quantum Inf. **7**, 173 (2021).

[29] A. Bienfait, Y. P. Zhong, H. S. Chang, M. H. Chou, C. R. Conner, Dumur, J. Grebel, G. A. Peairs, R. G. Povey, K. J. Satzinger, and A. N. Cleland, Quantum Erasure Using Entangled Surface Acoustic Phonons, Phys. Rev. X **10**, 21055 (2020).

[30] J. Chan, A. H. Safavi-Naeini, J. T. Hill, S. Meenehan, and O. Painter, Optimized optomechanical crystal cavity with acoustic radiation shield, App. Phys. Lett. **101**, 081115 (2012).

[31] A. Wallucks, I. Marinković, B. Hensen, R. Stockill, and S. Gröblacher, A quantum memory at telecom wavelengths, Nature Phys. **16**, 772 (2020).

[32] R. N. Patel, Z. Wang, W. Jiang, C. J. Sarabalis, J. T. Hill, and A. H. Safavi-Naeini, Single-mode phononic wire, Phys. Rev. Lett. **121**, 040501 (2018).

[33] A. Zivari, R. Stockill, N. Fiaschi, and S. Gröblacher, Non-classical mechanical states guided in a phononic waveguide, Nature Phys. **18**, 789 (2022).

[34] J. F. Clauser, M. A. Horne, A. Shimony, and R. A. Holt, Proposed experiment to test local hidden-variable theories, Phys. Rev. Lett. **23**, 880 (1969).

[35] I. Marinković, A. Wallucks, R. Riedinger, S. Hong, M. Aspelmeyer, and S. Gröblacher, An optomechanical Bell test, Phys. Rev. Lett. **121**, 220404 (2018).

[36] S. T. Velez, V. Sudhir, N. Sangouard, and C. Galland, Bell correlations between light and vibration at ambient conditions, Science Adv. **6**, eabb0260 (2020).

[37] R. Riedinger, S. Hong, R. A. Norte, J. A. Slater, J. Shang, A. G. Krause, V. Anant, M. Aspelmeyer, and S. Gröblacher, Non-classical correlations between single photons and phonons from a mechanical oscillator, Nature **530**, 313 (2016).

[38] S. Weis, R. Rivière, S. Deléglise, E. Gavartin, O. Arcizet, A. Schliesser, and T. J. Kippenberg, Optomechanically Induced Transparency, Science **330**, 1520 (2010).

[39] R. Stockill, M. Forsch, G. Beaudoin, K. Pantzas, I. Sagnes, R. Braive, and S. Gröblacher, Gallium phosphide as a piezoelectric platform for quantum optomechanics, Phys. Rev. Lett. **123**, 163602 (2019).

[40] S. Hong, R. Riedinger, I. Marinković, A. Wallucks, S. G. Hofer, R. A. Norte, M. Aspelmeyer, and S. Gröblacher, Hanbury Brown and Twiss interferometry of single phonons from an optomechanical resonator, Science **358**, 203 (2017).

[41] K. Børkje, A. Nunnenkamp, and S. M. Girvin, Proposal for entangling remote micromechanical oscillators via optical measurements, Phys. Rev. Lett. **107**, 123601 (2011).

[42] R. Riedinger, A. Wallucks, I. Marinković, C. Löschnauer, M. Aspelmeyer, S. Hong, and S. Gröblacher, Remote quantum entanglement between two micromechanical oscillators, Nature **556**, 473 (2018).

[43] L. M. Duan, M. D. Lukin, J. I. Cirac, and P. Zoller, Long-distance quantum communication with atomic ensembles and linear optics., Nature **414**, 413 (2001).

[44] J. C. Taylor, E. Chatterjee, W. F. Kindel, D. Soh, and M. Eichenfield, Reconfigurable quantum phononic circuits via piezo-acoustomechanical interactions, npj Quantum Inf. **8**, 19 (2022).

[45] J. Chan, T. P. M. Alegre, A. H. Safavi-Naeini, J. T. Hill, A. Krause, S. Gröblacher, M. Aspelmeyer, and O. Painter, Laser cooling of a nanomechanical oscillator into its quantum ground state, Nature **478**, 89 (2011).

[46] M. A. Luda, M. Drechsler, C. T. Schmiegelow, and J. Codnia, Compact embedded device for lock-in measurements and experiment active control, Rev. Scien. Instr. **90**, 023106 (2019).

[47] A. Aspect, J. Dalibard, and G. Roger, Experimental test of bell's inequalities using time-varying analyzers, Phys. Rev. Lett. **49**, 1804 (1982).

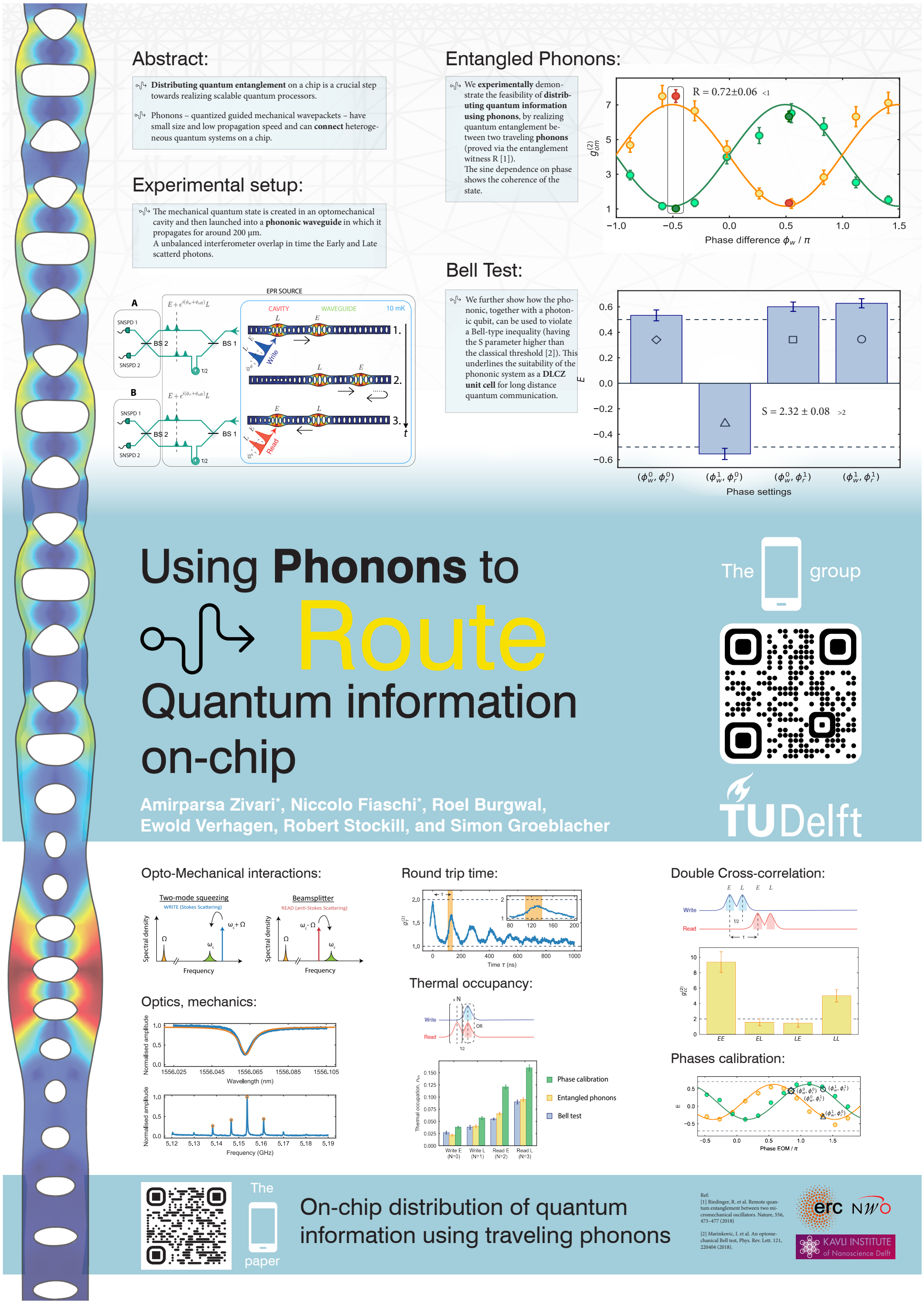

Abstract:

Distributing quantum entanglement on a chip is a crucial step towards realizing scalable quantum processors.

Phonons – quantized guided mechanical wavepackets – have small size and low propagation speed and can **connect** heterogeneous quantum systems on a chip.

Experimental setup:

The mechanical quantum state is created in an optomechanical cavity and then launched into a **phononic waveguide** in which it propagates for around 200 µm.
A unbalanced interferometer overlap in time the Early and Late scatterd photons.

Entangled Phonons:

We **experimentally** demonstrate the feasibility of **distributing quantum information using phonons**, by realizing quantum entanglement between two traveling **phonons** (proved via the entanglement witness R [1]).
The sine dependence on phase shows the coherence of the state.

Bell Test:

We further show how the phononic, together with a photonic qubit, can be used to violate a Bell-type inequality (having the S parameter higher than the classical threshold [2]). This underlines the suitability of the phononic system as a **DLCZ unit cell** for long distance quantum communication.

Using **Phonons** to Route Quantum information on-chip

Amirparsa Zivari*, Niccolo Fiaschi*, Roel Burgwal, Ewold Verhagen, Robert Stockill, and Simon Groeblacher

The group

TU Delft

Opto-Mechanical interactions:

Optics, mechanics:

Round trip time:

Thermal occupancy:

Double Cross-correlation:

Phases calibration:

The paper

On-chip distribution of quantum information using traveling phonons

Ref:
[1] Riedinger, R. et al. Remote quantum entanglement between two micromechanical oscillators. Nature, 556, 473–477 (2018)

[2] Marinkovic, I. et al. An optomechanical Bell test, Phys. Rev. Lett. 121, 220404 (2018).

Poster for the paper Amirparsa Zivari*, Niccolò Fiaschi*, Roel Burgwal, Ewold Verhagen, Robert Stockill, and Simon Gröblacher, *On-chip distribution of quantum information using traveling phonons*, Science Advances Vol 8, Issue 46 (2022).

5

TIME-RESOLVED SPECTRAL DIFFUSION OF A MULTIMODE MECHANICAL MEMORY

**Niccolò FIASCHI, Amirparsa ZIVARI, Lorenzo SCARPELLI,
Alexander Rolf KORSCH, Simon GRÖBLACHER**

Phonons hold great promises as carriers of quantum information on-chip. Thanks to the coherent interaction with several systems, they compact mode volume and slow group velocity, they have been recently used for the coherent transport of information on chip, interconnecting quantum devices. The strong confined phonons in waveguide-like systems, are especially interesting because of their long lifetime. However, it is well known that this type of mechanical system suffers from spectral diffusion (mechanical frequency jitter), which ultimately limits the coherence time in multi-mode mechanical devices [1–3]. Here we perform a time-domain study on two adjacent mechanical modes (separated by $\sim 5\,\mathrm{MHz}$*) and show that the frequency positions of the two modes are not correlated in time. This result can help in understanding the mechanism of dephasing, and so pave the path towards long coherence mechanical quantum memory.*

5.1. INTRODUCTION

OVER the past years several groundbreaking experiments have proven that high frequency phonons (~ 5 GHz) can be efficiently used as carriers of information on-chip. In particular, using Surface Acoustic Waves (SAWs) as mediators, it has been recently shown quantum state transfer and remote entanglement between two superconducting qubits [4]. SAWs are particularly interesting since over the years they have been proven as a mature platform for coherent control of quantum information on-chip, having also demonstrated a beam-splitter [5] and a phase shifter [6]. However, SAWs have limited coherence time because the short lifetime (in the order of μs). Due to lifetime exceeding ms, more strongly confined phonons in waveguide-like systems are a promising platform for on-chip distribution of quantum information [7, 8]. In this type of system, the coherence of the information that travels in the waveguide is ultimately limited by the spectral diffusion (frequency jitter of the mechanical mode). This phenomenon was initially observed and studied in single mode optomechanical cavities [1], where the coherence time of the single mechanical mode is in the order of 100 µs [2, 3]. In this work, we study the spectral diffusion of two spectrally close mechanical modes (centred at ~ 5 GHz and spaced by ~ 5 MHz) of the same optomechanical device. We find that the time traces of the frequency positions of the two mechanical modes are non correlated.

5.2. METHODS

THE device used is identical to the one of [7]. This type of device has a optomechanical cavity connected to a single-mode mechanical waveguide (ended with a free standing end, that acts as a mechanical mirror). The hybridized mechanical mode of the structure forms a comb of closely spaced mechanical modes, with similar mode shapes, separated by ~ 5 MHz around a central frequency of 5 GHz. On the other side, the cavity is still single mode for the optical field with the resonance in the telecom band around 1550 nm. We report in Fig. 5.1a the SEM of a device identical to the one used in this work. We highlight the optomechanical cavity in red, the photonic and phononic mirror in blue and the phononic waveguide (that still acts as a mirror for photons) in green.

To resolve in time the mechanical frequency of the device we use a frequency demodulation setup, which is schematically shown in Fig. 5.1b. The orange curve is the measured (averaged) Power Spectral Density of the mechanical mode. Two Real-time Spectrum Analizers (RSAs) are used in zero-span mode to acquire the total power filtered from the Resolution BanWidth (RBW) filter in the function of time. One RSA (RSA1, green line in the figure), has the filter detuned by -RBW/2 = -100 kHz from the mechanical mode. In this way, the frequency jitter is mapped into an amplitude modulation of the signal measured by RSA1. A cartoon image of the time trace of the frequency jitter is depicted with the dark orange line, while the dark green line is the corresponding amplitude variation of the signal measured (the dashed lines are the time axis). However, a change in the amplitude of the mechanical peak will also cause a change in the amplitude of the signal measured. For this reason, the other RSA (RSA2, dark grey line) have the filter on resonance with the mechanical mode. In this way, we can measure the amplitude fluctuations of the signal with RSA2 and the (amplitude) and frequency fluctuations with RSA1. Normalizing the signal from RSA1 with the one from RSA2 allows

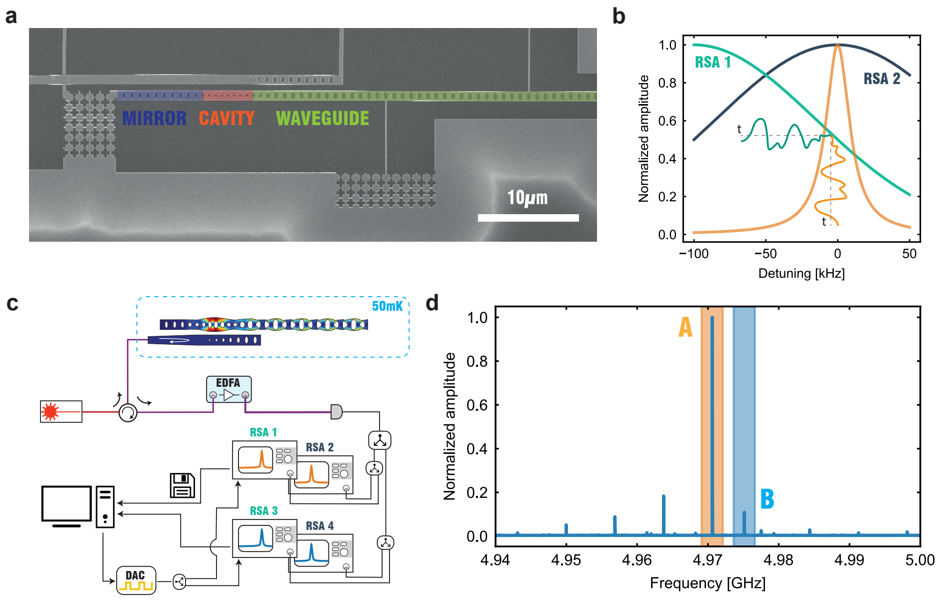

Figure 5.1: **Setup and initial characterization.** a) SEM of a device identical to the one used in the measurements. The optomechanical cavity is highlighted in red, the photonic and phononic mirror in blue and the single mode mechanical waveguide (and photonic mirror) in green. b) Cartoon picture of the measurement of the jitter in time of a single mode broadened by frequency diffusion (orange line). One RSA has the filter at the mechanical frequency (RSA2, dark grey line), to capture in time the amplitude fluctuations of the signal, while the other RSA has the filter detuned by -RBW/2 = -100 kHz, to be also sensitive to the frequency jitter of the mechanical mode (RSA1, green line). A Cartoon picture of a time trace of the jittering (dark orange line) shows how the frequency fluctuations are mapped into amplitude fluctuations (dark green line). The dashed lines are the time axis. c) Scheme of the experimental setup. The laser is routed to the device in the mk stage of the dilution refrigerator via a fiber circulator and a lensed fiber. The light coming out of the device is amplified with an Erbium Doped Fiber Amplifier (EDFA) and sent to a fast photodiode. The signal from the photodiode is split with RF splitters and analysed with four synchronized Real Time Spectrum Analyzers (RSA1, 2, 3 and 4). All RSAs are triggered externally via a TTL signal from a DAC card, which allows sub-mu*s* synchronization. b) Mechanical spectrum of the device with several visible modes. The modes used in the measurements are called mode A (shaded in orange), and mode B (shaded in blue).

us to extract the frequency position of the mechanical mode in time, even if the signal is modulated in amplitude and frequency. We will use two RSAs in this configuration for each mechanical mode in all the measurements.

The setup used in this work for the frequency demodulation is schematically shown in Fig. 5.1c. A Continuous Wave (CW) laser, red detuned from the optical resonance by the average mechanical frequency of the modes of interest (≈ 5 GHz), is routed to the device inside the bottom stage of a dilution refrigerator (temperature of 50 mK) via a circulator and a lensed fiber (coupling efficiency of 10%). The CW light is partially absorbed by the device, creating a thermal population in the mechanical modes of interest. This population is read via the beam-splitter interaction with the same CW laser, which creates sidebands detuned from the laser carrier by the mechanical frequencies [7]. In all the measurements the instantaneous photon number in the optomechanical cavity is ≈3000 (see 5.5 for more). The output of the circulator is amplified with an Erbium Doped fiber Amplifier (EDFA) to have a high enough signal on the fast detector. The output of the detector is split with 3 power splitters and sent to 4 Real time Spectrum Analyzer (RSA1, 2, 3 and 4). RSA1 and 3 are detuned by -RBW/2 = -100 kHz from the mechanical mode measured, while RSA2 and 4 are always in resonance with it. The RSAs are synchronized in the data acquisition via a TTL signal that triggers all the RSAs simultaneously, with a relative delay of sub-μs. The data is then saved on the computer for the post-process.

After we scan the optical resonance (see section 5.5 for more), we measure the Power Spectral Density (PSD) of the device with a broad range of frequencies to identify the two mechanical modes of interest, and we report this in Fig. 5.1b. We see that the device has a comb of mechanical modes, due to the hybridization of the single mode mechanical cavity with the Fabry-Pérot cavity formed by the long waveguide with the free standing edge [7]. We highlight with a shaded region in the plot the two modes used in this work: mode A in orange and mode B in blue. With the power used in this work, the peaks have a FWHM = 20 kHz (see section 5.5 for more). We measure with Optomechanical Induced Transparency (OMIT) the optomechanical coupling of each mode, finding 0.3 MHz for A and 0.2 MHz for B.

To initially characterize the jitter we can use RSA1 and RSA3 to take frequency scans of the peaks (PSD), as previously done in [2]. We report that to have sensible information of the peak, the fastest scan possible takes 200 µs (RBW = 10 kHz). Even in this configuration, approximately half of the scans have more than one prominent peak (see section 5.5 for more). This indicates that the time scale of the jitter is much faster than the scan time. We can overcome this limit by using the frequency demodulation technique, which allows us to use a larger RBW and so have a finer time resolution.

5.3. RESULTS

WE use the four RSAs to measure time traces of the two mechanical modes in four configurations: AA, AB, BA and BB. RSA1 (3) is detuned by -RBW/2 = -100 kHz from the mode A (A), A (B), B (A) and B (B), respectively, while RSA2 and 4 are always on resonance with the mode measured by RSA1 and 3, respectively. Each time trace is 10 ms long, with 30000 points. For this measurement the choice of the RBW is crucial. We choose a 200 kHZ RBW filter as a trade-off for having a high enough time resolution ($\sim 1/RBW = 5$µs) and still high enough signal to noise ratio, high dynamical range and still a high sensitivity. With this bandwidth, the frequency jitter is in the linear part of the filter (in the detuned case) and on the flat part (in the resonance case). For the chosen filter, a frequency fluctuation of HWHM = 10 kHz gives a 0.7% change in amplitude for the filter at resonance with the mechanical mode, and a 7% change for the filter detuned by -RBW/2. With the amplitude of the signal from RSA2 and 4, we normalize the trace measured from RSA1 and 3. We then use the filter shape to convert the amplitude fluctuations into frequency fluctuations (see section 5.5 for more). The result of the measurements is reported in Fig. 5.2a, where we plot the frequency shift in time, from top to bottom, for the four configurations AA, AB, BA and BB, in orange (blue) and light orange (light blue) for mode A (B) measured from RSA1 and RSA3. In this plot, we show

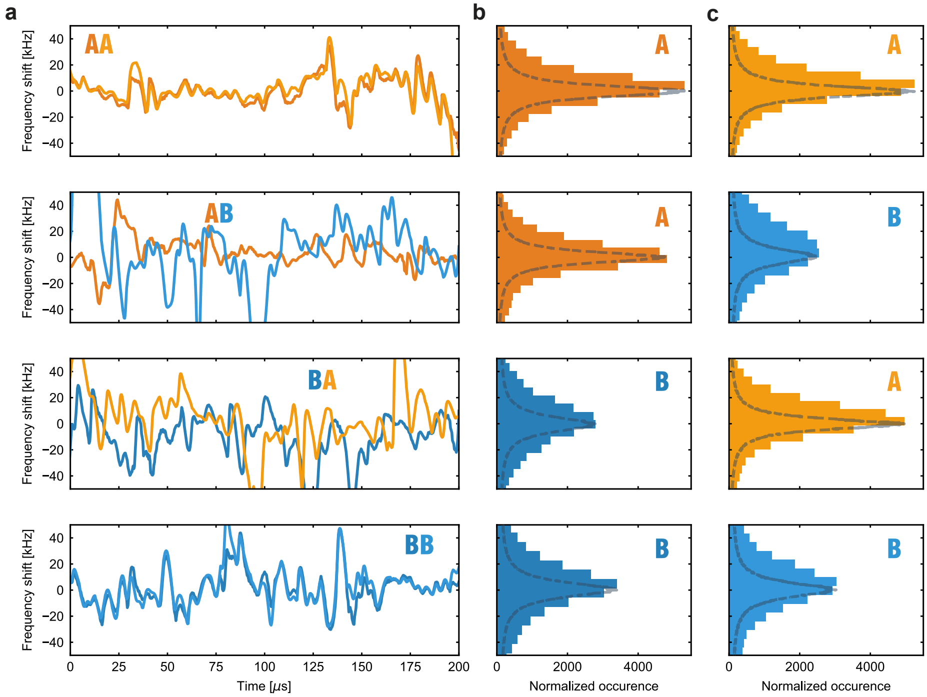

Figure 5.2: **Frequency jitter in time.** a) Time traces of the frequency jitter for mode A (orange as measured from RSA1 and light orange as measured from RSA3) and B (blue as measured from RSA1 and light blue as measured from RSA3). From top to bottom: the synchronized measurements are for the configurations AA, AB, BA and BB measured from RSA1 and RSA3 respectively (using RSA2 and RSA4 for the amplitude normalization). It's visible that AA and BB have (almost) identical time traces, while AB and BA show uncorrelated time traces. b) and c) Histogram of the frequency shift as measured from RSA1 and RSA3 for the modes AA, AB, BA, BB (from top to bottom) for a trace with 10 ms length. The dashed black line is the averaged mechanical spectrum measured with the corresponding RSA.

a 200 µs long segment of the full trace. We report a average signal to noise ratio of 10 for mode A (with a maximum value of 80) and 5 for B (with a maximum value of 30). It is visible that the AA and BB configuration have highly correlated signals, while the AB and BA configurations have uncorrelated time traces of the two modes. We report that the amplitude variation measured from RSA2 and 4 have uncorrelated traces, with changes of an order of magnitude in a scale as fast as 10 µs (see section 5.5 for more). We also report that the (common mode) frequency jitter that can be caused by laser frequency shifts and changes of laser power is much smaller than the one reported here (see section 5.5 for more). We show in Fig. 5.2b and c, the histogram of the frequency shift for the complete trace. The dashed black line is the mechanical PSD as measured from the RSAs (averaging for ≈ 30 s for each measurement). Note that the two (independent) measurements have a very good agreement, confirming the validity of the method used. The (little) discrepancy in FHWM of the distribution should arise mainly from the noise in the measurement of the amplitude from RSA2 and 4.

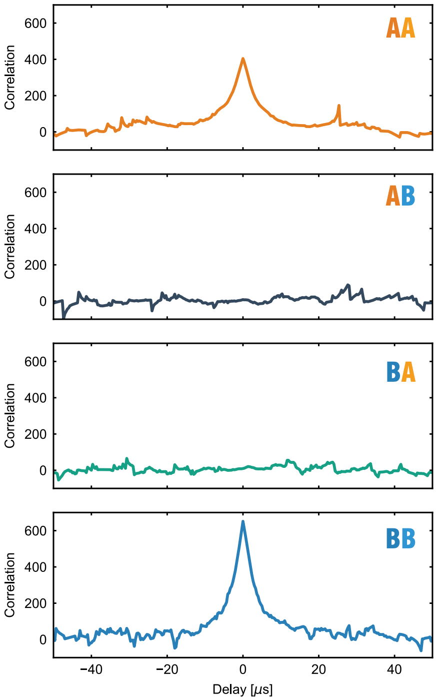

Figure 5.3: **Correlation of the frequency jitter.** From top to bottom: correlation function (as defined in the main text) for the configuration AA (orange line), AB (dark grey line), BA (green line), and BB (blue line) for the full traces of Fig. 5.2 with 10 ms length. The AA and BB case shows a strong correlation at zero delays and exponential decay to zero (uncorrelated), while the AB and BA case only shows uncorrelated values for all delays.

To assess quantitatively if the traces are correlated or not, and to extract the correlation time of the frequency shift, we calculate the correlation function in the four configurations. We use the full time trace, with a total length of 10 ms, divided into segments. Each segment is defined as consequent points of the trace that have only physical values of the frequency jitter (non physical values can arise from the calibration of the y-axis, or because of the noise floor). We use 2/3 of the total data points. The correlation function for each segment is define as:

$$C_j(\tau) = \sum_{i=0}^{N_j} (S_j(t_i) - \overline{S})(S_j(t_i + \tau) - \overline{S}) \tag{5.1}$$

were S_j is the segment j, with N_j points, of the frequency shift in time and $\overline{S}$ the average value [9]. We average between the calculated correlation of all segments (each with a weight given by the number of points of the segment) and we show the results in Fig. 5.3, from top to bottom for AA (in orange), AB (in dark grey), BA (in green) and BB (in blue). It is visible from the graph that AA and BB have a strong correlation at zero delay, while AB and BA have only non correlated values. Fitting the exponential decay of the correlation we measure a decay constant of 3.5µs for both AA and BB. This decay time should be limited by the RBW used which sets a 5µs integration time. A more detailed study with different RBWs could determine more accurately this number. We stress that this decay time is not the coherence time.

We also report in section 5.5 the Fast Fourier Transform (FFT) of the complete time trace. Since we find that the spectra of the frequency jitter of the two modes are identical, the decoherence mechanism should be the same. We perform the same experiment at a temperature of 800 mK and we report that the results are identical. This indicates that the effective temperature of the device, caused by the optical absorption, is much higher than the base temperature of the dilution refrigerator (see section 5.5 for more).

5.4. DISCUSSION

OUR experiment shows that two mechanical modes even if spectrally close and with extremely similar mode shapes have an uncorrelated spectral diffusion. For this reason, using two devices in a dual rail scheme [10, 11] or a single device with multiple mechanical modes [8] will have (at best) the same coherence time. However, a single device scheme will allow for an easier experimental setup and less stringent requirements in the fabrication process. We expect that the two modes have the same dephasing mechanism since they have the same FFT of the frequency jitter. This could mean that the two modes are coupled very differently to the same surface defects which, most likely, are the cause of this jittering [3]. Our result shreds some light on the cause of the frequency diffusion in mechanical oscillators and can open the way to long coherence time mechanical quantum memories. In particular, it shows that a detailed analysis via surface treatments of the silicon (or even using other materials, like Silicon Nitride) is necessary. It also shows that, if the surface defects are the cause of the dephasing, they can be saturated to have long coherence time in the mechanical quantum memory.

Acknowledgments We would like to thank Raymond Schouten for valuable discussions and Clinton Potts for support. We further acknowledge assistance from the Kavli Nanolab Delft. This work is financially supported by the European Research Council (ERC CoG Q-ECHOS, 101001005) and is part of the research program of the Netherlands Organization for Scientific Research (NWO), supported by the NWO Frontiers of Nanoscience program, as well as through Vidi (680-47-541/994) and Vrij Programma (680-92-18-04) grants.

Conflict of interests: The authors declare no competing interests.

Author contributions: N.F. devised and planned the experiment, built the setup and performed the measurements. A.R.K. found the device. N.F., A.R.K., A.Z. characterize the device. N.F., A.Z. fabricated the sample, N.F., A.Z., L.S. and S.G. analyzed the data and wrote the manuscript with input from all authors. S.G. supervised the project.

Data Availability: Source data for the plots are available on Zenodo

5.5. SUPPLEMENTARY INFORMATION

OPTICAL AND MECHANICAL RESONANCE(S)

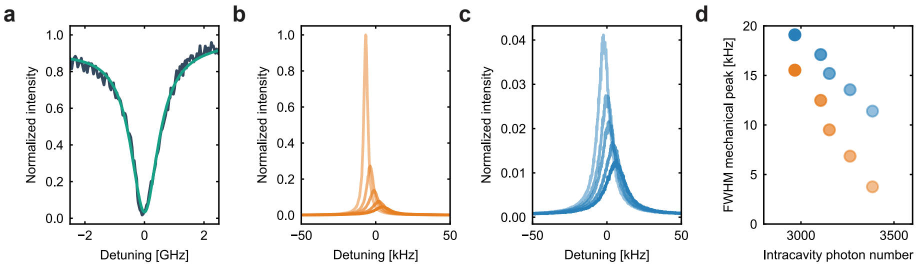

Figure 5.4: a) Optical resonance of the optomechanical cavity. The resoance is centered at ≈ 1535 nm and has a linewidth of 1.1 GHz. b) and c) Averaged mechanical PSD of mode A (in orange) and B (in blue), each measurement is integrated for ≈ 30 s. The several spectra are for different intracavity photon numbers (increasing intracavity photon numbers for lighter colours, see d for the actual values), that are proportional to the power sent to the device. Optomechanical spring effect and phonon lasing, shift the resonances and decrease the linewidth with increased intracavity photon number. d) Linewidth of the mechanical peaks (A in orange and B in blue), as a function of the intracavity photon number. In the measurement in the main text, the intracavity photon number is ≈ 3000.

To measure the optical resonance we scan the laser in frequency and we measure the power coming from the device on a photodiode. We report the data in Fig. 5.4a, in dark grey, and the Lorentzian fit, in green. From the fit, we can extract a resonance frequency of ≈ 1535 nm and a linewidth of 1.1 GHz. We then measure the (averaged) PSD of the two mechanical modes, Fig. 5.4b and c for mode A (orange) and mode B (blue), as a function of the intracavity photon number (proportional to the power sent to the device, see Fig. 5.4d for the actual values). As expected, the optomechanical spring effect and phonon lasing shift the mechanical resonances and decrease the linewidth with increased intracavity photon number [1, 12, 13]. In Fig. 5.4d we report the measure linewidths for mode A (in orange) and mode B (in blue), in the function of the intracavity photon number. In the measurement in the main text, the intracavity photon number is ≈ 3000, which is the lower value we could use to still have a high enough signal to noise ratio for the time traces of mode B.

LIFETIME

To measure the lifetime of the phonons in the device we send series of pairs of red-detuned pulses: pump and probe [11]. The pump pulse (the first one to arrive at the device), creates a thermal population in the cavity, while the probe pulse (that arrives at the device after a certain delay) measures the not-normalized thermal occupation of the cavity. We repeat the pair of pulses every 50 ms. Sweeping the delay between the pulses, allows us to measure the decay of the thermal population created from the first pulse and extract the lifetime of the phonons. The data points (orange dots) and the exponential fit (orange line) are shown in Fig. 5.5. We measure a lifetime of $T_1 \approx 1$ ms.

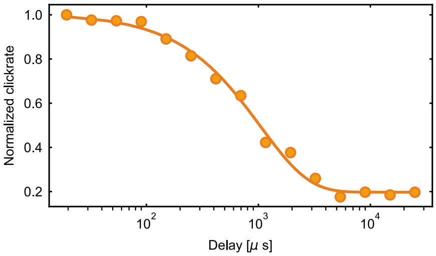

Figure 5.5: Normalized click rates of the probe pulse in the function of the delay between the two pulses (pump and probe). The clickrates are directly proportional to the thermal population of the device allowing to measure the lifetime of the phonons in the structure. From the exponential fit (orange line) we extract a $T_1 \approx 1\,\text{ms}$.

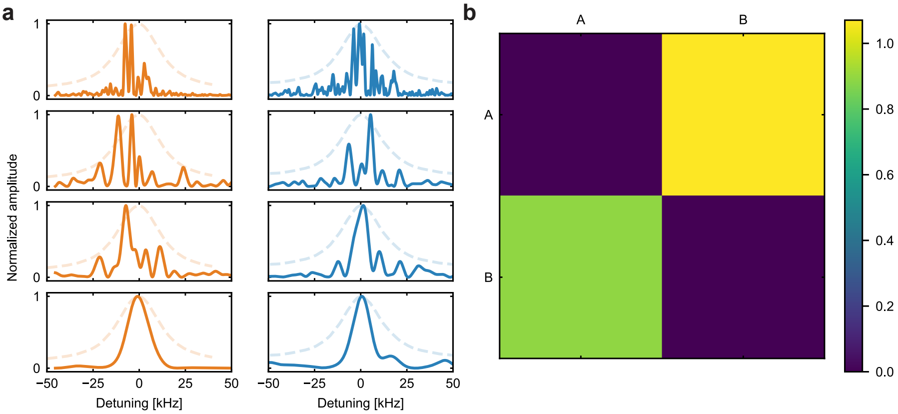

Figure 5.6: a) Fast scans of the mechanical modes A (in orange) and b (in blue) around their central frequencies using a RBW of 1 kHz, 3 kHz, 5 kHz and 10 kHz from top to bottom. The bottom scans are the fastest and have a sweep time of ≈200 µs. It is visible that, most of the scans with finer RBW (and so slower sweep time) measure the mechanical peak several times in a single sweep. For the 10 kHz case, most of the scans show a single prominent peak. The dashed lines are the mechanical spectrum with 3000 averages. b) Correlation distance matrix between the modes A and B. The AA and BB correlations are very close to zero, showing a very strong autocorrelation, while the AB and BA are very close to unity, showing that are uncorrelated.

FAST SCANS ON THE RSA

To measure the correlations of the frequency positions of the two mechanical modes we can perform synchronized fast scans on the RSAs. Ideally, if the jitter is slower than the sweep time of the scan, only one peak should be visible. From this measurement, the positions of the peak can be measured and the spatial correlation can be calculated. As visible from Fig. 5.6a, we saw that for small Radio BandWidth (RBW, 1 kHz, 3 kHz and 5 kHz, from top to bottom, respectively), most of the times the spectrum shows multiple peaks, indicating that the scan sweeps are too long. For RBW of 10 kHz (bottom plot) we have a fast enough scan (with a sweep time of ≈ 200 µs) and enough resolution to distinguish single peaks inside the average envelope. With this last bandwidth we take 300 scans for each combination of peaks (AA, AB, BA and BB) and we post-select only the ones with a clear single peak. We obtain between 100 and 150 single peaks for each combination. We use the maximum values of the peaks for each pair of scans as positions of the mechanical frequencies, creating two vectors of positions. We then use the correlation distance between the vectors to asses if the mechanical frequencies are correlated. For two vectors $\vec{u}$ and $\vec{v}$ the correlation distance is defined as:

$$1-\frac{(\vec{u}-\bar{\vec{u}})\cdot(\vec{v}-\bar{\vec{v}})}{||\vec{u}-\bar{\vec{u}}||_2||\vec{v}-\bar{\vec{v}}||_2}$$

With this definition, two perfectly correlated (anti-correlated) vectors have a correlation distance of 0 (2), while two uncorrelated vectors have a correlation distance of 1. We report the results of the measure in Fig. 5.6b, where we show that the combination AA and BB are correlated while AB and BA are uncorrelated.

COMMON MODE JITTER

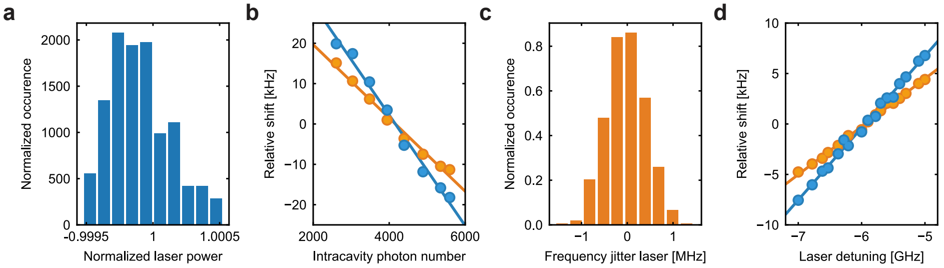

Figure 5.7: a) Normalized histogram of the normalized power of the laser. The standard deviation of the distribution is ≈ $2e-4$. The measure is taken with an integration time of 100 ms and lasted a minute, much longer than the time of a single measurement reported in the paper. b) Frequency shift of the mechanical peaks in function of the intracavity photon number (that scale linearly with the power of the laser), for mode A (in orange) and mode B (in blue). From the linear fit (solid line, same color as the datapoints) and the distribution of laser power reported in a), we can extract a maximum (common mode) frequency jitter given by the power fluctuation of the laser of ≈ 20 Hz, much smaller than the frequency jitter of the mechanical modes. c) Normalized histogram of the frequency jitter of the laser, The standard deviation of the distribution is ≈ 0.42 MHz. The measurement is taken 5 times per second and lasted 3 minutes, much longer than the time of the single measurements reported in the paper. d) Frequency shift of the mechanical frequencies of mode A (in orange) and B (in blue) as a function of the laser detuning from the optical resonance. From the linear fit (solid line, same color as the datapoints) and the distribution of laser frequencies reported in c), we can extract a maximum (common mode) frequency jitter given by the frequency fluctuations of ≈ 30 Hz, much smaller than the frequency jitter of the mechanical modes. In both b) and d) the differences in angular coefficient are given by the different g_0 of the two modes.

Both the laser power and detuning from the optical resonance cause a (common mode) frequency shift of the mechanical modes. We estimate this jitter using the distribution of laser power and frequencies. To do so we measure laser power and frequency in time and we report the normalized histogram of these two quantities in Fig. 5.7a and c. The standard deviations of the distributions are $\approx 2*10-4$ and ≈ 0.42 MHz, respectively. We also measure the mechanical frequencies as a function of the intracavity photon number (that scale linearly with the laser power) and as a function of the detuning of the laser from the optical resonance. We report the data in Fig. 5.7b and d, in orange for mode A and in blue for mode B. From the linear fit (solid line) we can extract a maximum (common mode) frequency jitter of the mechanical modes of $\approx 20\,\mathrm{Hz}$ given by the laser power fluctuations, and of $\approx 30\,\mathrm{Hz}$ given by the laser frequency fluctuations. These jitters are much smaller than the ones reported in the main text.

CALIBRATION OF RSA FILTER

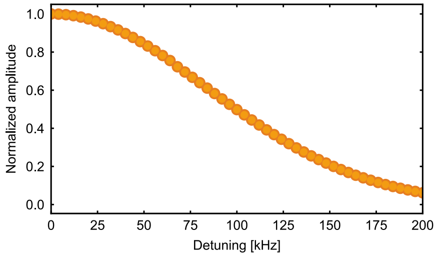

Figure 5.8: Average value of 1 ms traces with different detunings of the filter center with respect to a microwave source, for a RBW of 200 kHz. From the Gaussian fit, we measure a FWHM of ≈200 kHz for all the RSAs used.

To calibrate from amplitude to frequency to y-axis we need to know precisely the filter shape of the RSA. We use an external microwave source at a (fixed) frequency around 5 GHz. We then take time traces of 1 ms at several detunings from the microwave frequency. We average the traces and we plot them in the function of the detuning in Fig. 5.8. From the Gaussian fit, we find a $FWHM_{\mathrm{Filter}}$ of ≈200 kHz for all the RSAs used, for the RBW of 200 kHz.

AMPLITUDE FLUCTUATIONS

We found that the amplitude of the signals fluctuates in time, even in the case of the filter of the RSA at resonance with the mechanical modes. We report a time trace (for the same time as Fig. 5.2) in Fig. 5.9a, for the four configurations (AA, AB, BA, and BB) as measured from RSA2 and RSA4 with the filter at resonance. In this configuration, from the frequency jitter, we can expect a 0.7% change in amplitude for a frequency fluctuation of HWHM. We see that the amplitude variations are as big as an order of magnitude. Moreover, we note that these amplitude variations are not correlated between the two modes. This excludes common mode amplitude fluctuations which can come from changes in laser power or frequency, amplification of the EDFA, or losses in the optical path (from the vibration of the lensed fiber given by the pulse tube of the dilution refrigerator). Since the amplitude of the signal is directly proportional to the (thermal) population of the mode we see that in this regime there are considerable changes in the population in a time scale as short as μs. This could come from exchanges in population with the thermal bath and/or with the Two Level Systems (TLSs) hosted in the material. In Fig. 5.9b and c we report the histogram of the amplitude of the signal for the full 10 ms trace for the four cases: AA (in orange and light orange for RSA2 and RSA4, respectively),

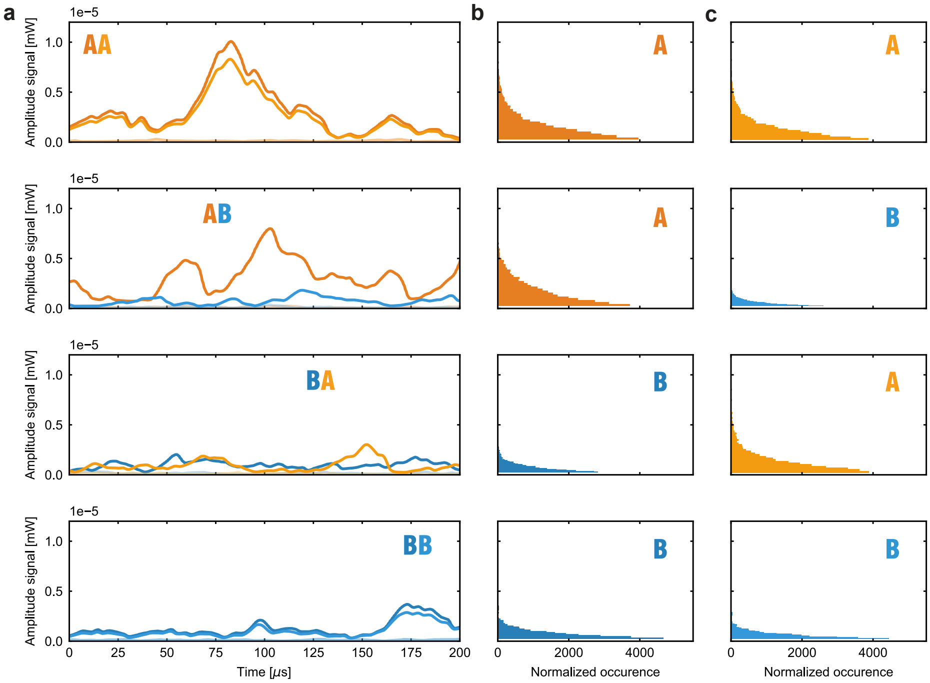

Figure 5.9: a) Time traces of the amplitude fluctuations of the signal for mode A (orange as measured from RSA2 and light orange as measured from RSA4) and B (blue as measured from RSA2 and light blue as measured from RSA4) with the filters on resonance with the mechanical modes. From top to bottom: the synchronized measurements are for the configurations AA, AB, BA, and BB measured from RSA2 and RSA4 respectively, and are for the same time as of Fig. 5.2. It's visible that AA and BB have (almost) identical time traces, while AB and BA show uncorrelated time traces even for the amplitude of the modes. The small difference in signal comes from different losses and splitting ratios of the RF power splitters and it's compensated in post-analysis to convert the y-axis in frequency in Fig. 5.2. The partially transparent traces are the background measurements taken 200 MHz from the mechanical modes of interest (at a frequency with no visible peaks). b) and c) Histogram of the amplitude fluctuations as measured from RSA2 and RSA4 for the modes AA, AB, BA, BB (from top to bottom) for a trace with 10 ms length.

AB (in orange and light blue for RSA2 and RSA4, respectively), BA (in blue and light orange for RSA2 and RSA4, respectively) and BB (in blue and light blue for RSA2 and RSA4, respectively). The histogram clearly shows that the amplitude is not peaked around one value (higher than the noise floor), instead is an exponential distribution in frequencies. We find that more than 98% of the time the amplitude is smaller than half of the maximum amplitude of the full trace. A study for lower intracavity photon numbers could give more information on the nature of these amplitude fluctuations.

FREQUENCY FLUCTUATIONS AT 800 mK

To understand better the behavior of the frequency jitter we perform the same measurement reported in Fig.5.2 with a temperature of the mixing chamber plate (where the sample holder is located) of 800 mK. We report the measurement of the frequency shift

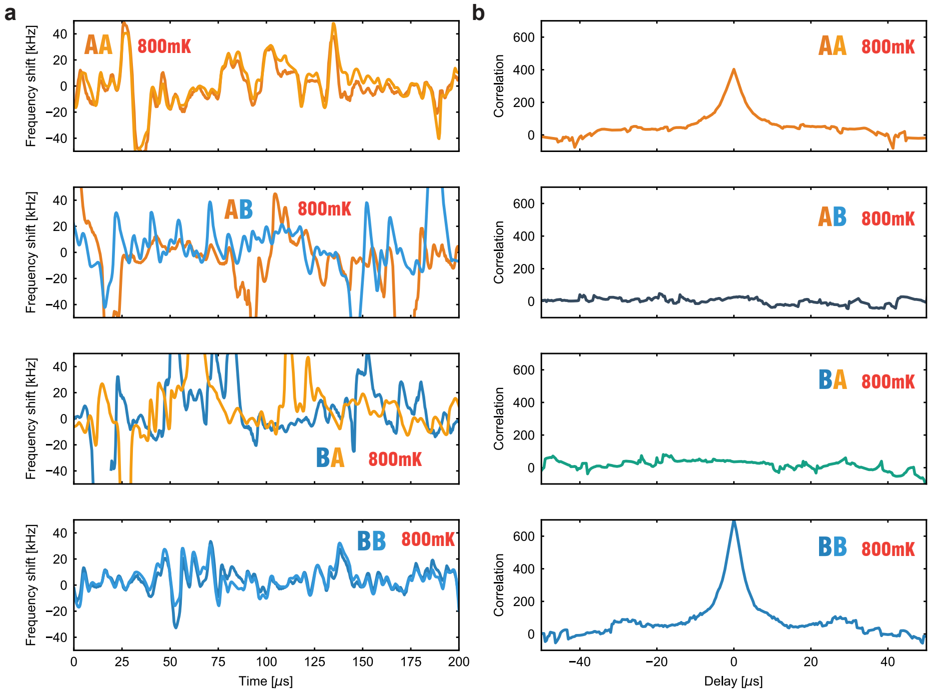

Figure 5.10: a) Time traces of the frequency jitter for mode A (orange as measured from RSA1 and light orange as measured from RSA3) and B (blue as measured from RSA1 and light blue as measured from RSA3) with the temperature of the mixing chamber plate of the dilution refrigerator at 800 mK. From top to bottom: the synchronized measurements are for the configurations AA, AB, BA, and BB measured from RSA1 and RSA3 respectively (using RSA2 and RSA4 for the amplitude normalization). The qualitative behavior does not change compared to the measure at 50 mK reported in Fig.5.2. b) Correlation function for the configuration AA (orange line), AB (dark grey line), BA (green line), and BB (blue line) as measured with RSA1 and RSA3 for the full traces of Fig. 5.10a with 10 ms length. As reported in Fig. 5.3, the AA and BB case shows a strong correlation at zero delays and exponential decay to zero (uncorrelated), with a decay constant identical to the data of Fig. 5.3, while the AB and BA case only shows uncorrelated values for all delays.

in time in Fig.5.10a for mode A (in orange and light orange for RSA1 and RSA3, respectively) and mode B (in blue and light blue for RSA1 and RSA3, respectively). We report an identical trend between the measure at 50 mK and the one presented here performed at 800 mK. This is because the high power of the CW laser used cause high heating of the device, and makes its effective temperature on the order of 1 K. For completeness we also show in Fig. 5.10b the correlation in time of the full trace of length 10 ms, calculated as done in Fig. 5.3. We saw that even in this case only the AA and BB configuration shows a strong correlation at zero delays, while AB and BA have always uncorrelated (value always close to zero).

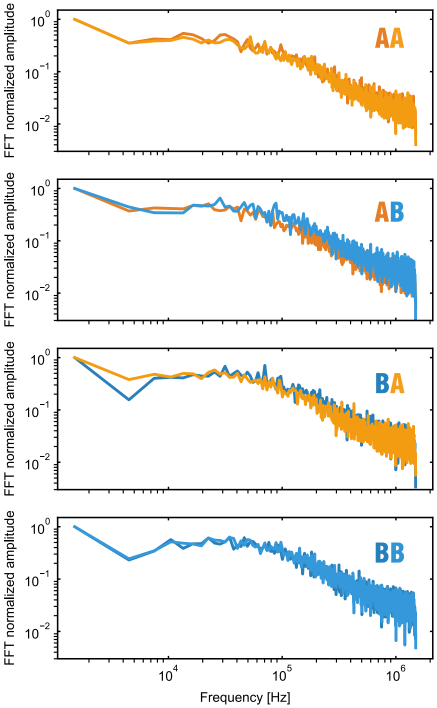

Figure 5.11: From top to bottom: Fast Fourier Transform of the frequency shift in time for the configurations AA, AB, BA, and BB measured from RSA1 and RSA3 respectively. In this figure, we used the full trace of Fig. 5.2 with 10 ms length. The spectra of the frequency jitter are white until a cutoff frequency of ≈ 100 kHz, at which they decay exponentially. We report that for the measurement taken at 800 mk the spectra have the same trend and cutoff frequencies.

FFT OF THE JITTER

To see if the jitter in time has some dominant frequency components, we perform the Fast Fourier Transform (FFT) of the frequency shift in time. We use the full trace (length 10 ms) of the dataset shown in Fig. 5.2 for the configurations AA, AB, BA, and BB. The dataset has non-physical values given by the calibration of the y-axis (when the amplitude signal measured from RSAs is comparable with the background noise). We divide the traces into segments, each defined by consequent data points with physical values. We use ≈ 2/3 of the total data points. We calculate the FFT from each segment of the traces, and we average the FFTs for each frequency value. We report the result in Fig. 5.11 for the configurations AA, AB, BA, and BB (orange and light orange for mode A and blue and light blue for mode B, measured by RSA1 and RSA3, respectively). We note that the spectra of the frequency jitter are white until a cutoff frequency of ≈ 100 kHz for all modes. This is the trend also of each FFT of the segments, indicating that even in the short timescale there are no preferred frequencies (up to the cutoff) of the jitter. We report that also for the measurement at 800 mK the spectra have the same trend and cutoff frequencies.

REFERENCES

[1] S. M. Meenehan, J. D. Cohen, S. Gröblacher, J. T. Hill, A. H. Safavi-Naeini, M. Aspelmeyer, and O. Painter, Silicon optomechanical crystal resonator at millikelvin temperatures, Phys. Rev. A **90**, 011803 (2014).

[2] A. Wallucks, I. Marinković, B. Hensen, R. Stockill, and S. Gröblacher, A quantum memory at telecom wavelengths, Nat. Phys. **16**, 772 (2020).

[3] G. S. MacCabe, H. Ren, J. Luo, J. D. Cohen, H. Zhou, A. Sipahigil, M. Mirhosseini, and O. Painter, Nano-acoustic resonator with ultralong phonon lifetime, Science **370**, 840 (2020).

[4] A. Bienfait, K. J. Satzinger, Y. P. Zhong, H.-S. Chang, M.-H. Chou, C. R. Conner, E. Dumur, J. Grebel, G. A. Peairs, R. G. Povey, and A. N. Cleland, Phonon-mediated quantum state transfer and remote qubit entanglement, Science **364**, 368 (2019).

[5] H. Qiao, E. Dumur, G. Andersson, H. Yan, M.-H. Chou, J. Grebel, C. R. Conner, Y. J. Joshi, J. M. Miller, R. G. Povey, X. Wu, and A. N. Cleland, Developing a platform for linear mechanical quantum computing, (2023), arXiv:2302.07791 [quant-ph] .

[6] L. Shao, D. Zhu, M. Colangelo, D. Lee, N. Sinclair, Y. Hu, P. T. Rakich, K. Lai, K. K. Berggren, and M. Lončar, Electrical control of surface acoustic waves, Nature Electronics **5**, 348 (2022), arXiv:2101.01626 .

[7] A. Zivari, R. Stockill, N. Fiaschi, and S. Gröblacher, Non-classical mechanical states guided in a phononic waveguide, Nature Phys. **18**, 789 (2022).

[8] A. Zivari, N. Fiaschi, R. Burgwal, E. Verhagen, R. Stockill, and S. Gröblacher, On-chip distribution of quantum information using traveling phonons, Science Advances **8**, eadd2811 (2022), https://www.science.org/doi/pdf/10.1126/sciadv.add2811 .

[9] R. Kubo, A stochastic theory of line shape, in *Advances in Chemical Physics* (John Wiley and Sons, Ltd, 1969) pp. 101–127, https://onlinelibrary.wiley.com/doi/pdf/10.1002/9780470143605.ch6 .

[10] R. Riedinger, A. Wallucks, I. Marinković, C. Löschnauer, M. Aspelmeyer, S. Hong, and S. Gröblacher, Remote quantum entanglement between two micromechanical oscillators, Nature **556**, 473 (2018).

[11] N. Fiaschi, B. Hensen, A. Wallucks, R. Benevides, J. Li, T. P. M. Alegre, and S. Gröblacher, Optomechanical quantum teleportation, Nature Photon. **15**, 817 (2021).

[12] M. Aspelmeyer, T. J. Kippenberg, and F. Marquardt, Cavity optomechanics, Rev. Mod. Phys. **86**, 1391 (2014).

[13] K. Cui, Z. Huang, N. Wu, Q. Xu, F. Pan, J. Xiong, X. Feng, F. Liu, W. Zhang, and Y. Huang, Phonon lasing in a hetero optomechanical crystal cavity, Photon. Res. **9**, 937 (2021).

6

CONCLUSION

In this thesis, we presented the work done towards the realization of a quantum network using high-frequency mechanical oscillators ($\nu \sim 5\,\mathrm{GHz}$).

These types of devices are attractive since they can be passively cooled down to the ground state using a commercially available dilution refrigerator. Moreover, mechanical modes can be coupled efficiently to several heterogeneous systems, like photons [1], defect centers [2], quantum dots [3] and superconducting qubits [4, 5], making them perfect candidates to connect quantum systems. The small mode volume (as small as $\sim 1\,\mu^3$), and the possibility to be fabricated in a plethora of materials (from silicon [6] and silicon nitride [7], to diamond [8]) makes them easy to be scaled and integrated into several types of architectures. Their low group velocity compared to microwave or optical photons also allows for small footprint delay lines, that could be useful for quantum computation [9]. Finally, the extremely long lifetimes (up to second [10, 11]), make them perfect candidates for long-storage quantum memories.

In this thesis, we presented a optomechanical quantum teleportation in chapter 2. In this chapter, we experimentally proved that we can teleport a polarization encoded flying qubit (telecom photon) onto a dual rail mechanical registry. The quantum memory is made by two single mode optomechanical cavities, and it is used to violate the classical bound on the fidelity by almost 5 standard deviations. This result is a fundamental first step towards the realization of quantum repeaters (using a DLCZ scheme, for example) that will allow for long-distance quantum communication [12].

In chapter 3, we showed that a non-classical phononic state can be generated, guided and retrieved on-chip. We used a multi-mode optomechanical device formed by a single mode optomechanical cavity coupled to a single-mode mechanical waveguide (ended with a phononic mirror). This proof of principle opened the way to the entanglement of two traveling phonons, reported in chapter 4. In this chapter, we showed that the traveling phonons can be used to distribute quantum entanglement on-chip, which is a first step towards connecting quantum devices on a short scale. Moreover, multimode mechanical devices could be used in DLCZ scheme with a time-bin encoding for long distance communication. A first step to demonstrate this could be the teleportation of a flying qubit (photon) into the multimode mechanical memory.

In chapter 5, we showed that the frequency jitter of two mechanical modes of the same device is not correlated in time. This will ultimately limit the coherence time (and so, length) of the information that travels in the mechanical waveguide. This result indicates that a detailed study of the decoherence mechanisms (and of ways to minimize them) is necessary to advance in this field.

While in these works we have been able to operate in the quantum regime (in chapter 2, 3 and 4), it has always been possible at the expense of the creation and retrieval rates (that set for example the teleportation or entanglement rates). In this thesis, the generation and read-out of the phonons were performed optically, and these processes are intrinsically probabilistic. The higher the pump power, the higher the scattering probability and the thermal background population. This then limits the scattering rates that can be achieved. A possible solution to this can be found in new types of optomechanical cavities (2D-like [13]), where the connection to the substrate should allow for a better thermalization of the cavity. Another possibility is to use metal near the cavity (distance of a few μm) to compensate for the low thermal conductivity of silicon at mK temperature. However, the choice of the metal is important to avoid catalytic effects [14]. A self-assembled superfluid helium thin film ($\sim nm$) could also help the thermalization. However, these films support "third sound" mechanical modes, which can shift the optical resonance and can limit the applications [15, 16]. If the thermal background is massively reduced and the scattering rates enhanced, we could perform single photon optomechanical induced transparency [17], deterministic reset of the memory, a (fully) mechanical Bell test [18] and long range entanglement swapping [12], to name a few. The thermal background limitation could be entirely avoided using a (transduced) excitation from a superconducting qubit [4]. In this way, the phonon that, for example, travels in the mechanical waveguide would be deterministically generated and would have a negligible thermal background. In this configuration, the waveguide can also be used as a long-storage memory for the qubit.

Routing quantum information on-chip is the first step towards full coherent control of traveling phonons. To complete the basic toolbox it's also needed a beam-splitter [19] and a phase shifter [20]. For the first one, we could envision two waveguides evanescently coupled via an array of mechanical shields. The splitting ratio can be adjusted deterministically (a priori) changing the number of shields connecting the waveguides. The phase shifter, instead, can be realized by applying an electric field on a piezo material. Using the shear stress of the piezo, a strain can be caused in the device membrane that changes the phase of the phonons. With these tools, all the fundamental experiments of quantum optics could in principle be done. For example, a (fully) phononic Hanbury Brown and Twiss interferometry [21], a Hong Ou Mandel [19] or even boson sampling [22, 23]. With these capabilities, the connections between heterogeneous and homogeneous systems on chip via phononic quantum buses could be also done in a reconfigurable way.

REFERENCES

[1] R. Riedinger, S. Hong, R. A. Norte, J. A. Slater, J. Shang, A. G. Krause, V. Anant, M. Aspelmeyer, and S. Gröblacher, Non-classical correlations between single photons and phonons from a mechanical oscillator, Nature **530**, 313 (2016).

[2] D. A. Golter, T. Oo, M. Amezcua, I. Lekavicius, K. A. Stewart, and H. Wang, Coupling a surface acoustic wave to an electron spin in diamond via a dark state, Phys. Rev. X **6**, 041060 (2016).

[3] R. P. G. McNeil, M. Kataoka, C. J. B. Ford, C. H. W. Barnes, D. Anderson, G. A. C. Jones, I. Farrer, and D. A. Ritchie, On-demand single-electron transfer between distant quantum dots, Nature **477**, 439 (2011).

[4] A. Bienfait, K. J. Satzinger, Y. P. Zhong, H.-S. Chang, M.-H. Chou, C. R. Conner, E. Dumur, J. Grebel, G. A. Peairs, R. G. Povey, and A. N. Cleland, Phonon-mediated quantum state transfer and remote qubit entanglement, Science **364**, 368 (2019).

[5] M. Mirhosseini, A. Sipahigil, M. Kalaee, and O. Painter, Superconducting qubit to optical photon transduction, Nature **588**, 599 (2020).

[6] M. Eichenfield, J. Chan, R. M. Camacho, K. J. Vahala, and O. Painter, Optomechanical crystals 10.1038/nature08524 (2009).

[7] J. Guo, J. Chang, X. Yao, and S. Gröblacher, Active-feedback quantum control of an integrated, low-frequency mechanical resonator (2023), arXiv:2304.02799 [quant-ph] .

[8] M. Koppenhöfer, C. Padgett, J. V. Cady, V. Dharod, H. Oh, A. C. Bleszynski Jayich, and A. A. Clerk, Single-Spin Readout and Quantum Sensing Using Optomechanically Induced Transparency, Physical Review Letters **130**, 10.1103/PhysRevLett.130.093603 (2023), arXiv:2212.01481 .

[9] H. Pichler, S. Choi, P. Zoller, and M. D. Lukin, Universal photonic quantum computation via time-delayed feedback, **114**, 11362 (2017).

[10] A. Wallucks, I. Marinković, B. Hensen, R. Stockill, and S. Gröblacher, A quantum memory at telecom wavelengths, Nat. Phys. **16**, 772 (2020).

[11] G. S. MacCabe, H. Ren, J. Luo, J. D. Cohen, H. Zhou, A. Sipahigil, M. Mirhosseini, and O. Painter, Nano-acoustic resonator with ultralong phonon lifetime, Science **370**, 840 (2020).

[12] L. M. Duan, M. D. Lukin, J. I. Cirac, and P. Zoller, Long-distance quantum communication with atomic ensembles and linear optics., Nature **414**, 413 (2001).

[13] H. Ren, M. H. Matheny, G. S. MacCabe, J. Luo, H. Pfeifer, M. Mirhosseini, and O. Painter, Two-dimensional optomechanical crystal cavity with high quantum cooperativity, Nature Communications 2020 11:1 **11**, 1 (2020), arXiv:1910.02873 .

[14] S. Yae, Y. Morii, N. Fukumuro, and H. Matsuda, Catalytic activity of noble metals for metal-assisted chemical etching of silicon, Nanoscale Research Letters **7**, 1 (2012).

[15] L. Zhang, W. Wen, J. Qian, al, Y. Wang, J. Wang, S. Forstner, Y. Sachkou, M. Woolley, G. I. Harris, X. He, W. P. Bowen, and C. G. Baker, Modelling of vorticity, sound and their interaction in two-dimensional superfluids, New Journal of Physics **21**, 053029 (2019).

[16] Y. L. Sfendla, C. G. Baker, G. I. Harris, L. Tian, R. A. Harrison, and W. P. Bowen, Extreme quantum nonlinearity in superfluid thin-film surface waves, npj Quantum Information 2021 7:1 **7**, 1 (2021).

[17] M. D. Eisaman, A. André, F. Massou, M. Fleischhauer, A. S. Zibrov, and M. D. Lukin, Electromagnetically induced transparency with tunable single-photon pulses, Nature 2005 438:7069 **438**, 837 (2005).

[18] I. Marinković, A. Wallucks, R. Riedinger, S. Hong, M. Aspelmeyer, and S. Gröblacher, An optomechanical Bell test, Phys. Rev. Lett. **121**, 220404 (2018).

[19] H. Qiao, E. Dumur, G. Andersson, H. Yan, M.-H. Chou, J. Grebel, C. R. Conner, Y. J. Joshi, J. M. Miller, R. G. Povey, X. Wu, and A. N. Cleland, Developing a platform for linear mechanical quantum computing (2023), arXiv:2302.07791 [quant-ph] .

[20] J. C. Taylor, E. Chatterjee, W. F. Kindel, D. Soh, and M. Eichenfield, Reconfigurable quantum phononic circuits via piezo-acoustomechanical interactions, npj Quantum Information **8**, 1 (2022), arXiv:2106.05406 .

[21] S. Hong, R. Riedinger, I. Marinković, A. Wallucks, S. G. Hofer, R. A. Norte, M. Aspelmeyer, and S. Gröblacher, Hanbury Brown and Twiss interferometry of single phonons from an optomechanical resonator, Science **358**, 203 (2017).

[22] J. B. Spring, B. J. Metcalf, P. C. Humphreys, W. S. Kolthammer, X. M. Jin, M. Barbieri, A. Datta, N. Thomas-Peter, N. K. Langford, D. Kundys, J. C. Gates, B. J. Smith, P. G. Smith, and I. A. Walmsley, Boson sampling on a photonic chip, Science **339**, 798 (2013), arXiv:1212.2622 .

[23] H. S. Zhong, H. Wang, Y. H. Deng, M. C. Chen, L. C. Peng, Y. H. Luo, J. Qin, D. Wu, X. Ding, Y. Hu, P. Hu, X. Y. Yang, W. J. Zhang, H. Li, Y. Li, X. Jiang, L. Gan, G. Yang, L. You, Z. Wang, L. Li, N. L. Liu, C. Y. Lu, and J. W. Pan, Quantum computational advantage using photons, Science **370**, 1460 (2020), arXiv:2012.01625 .

A

APPENDIX

A.1. NOTES ON LABORATORIES

IN this section we want to report some (small) suggestion and best practices in setting and working in a Lab.

- Temperature in the lab should be controlled in a max range of 0.5 Celsius, and the air conditioner should not give abrupt short pulses (each that last minutes) of air but a constant flow.
- Covering the optical tables with plastic sheets it is a, hopefully unnecessary, good measure to prevent damages of the equipment from water.
- Having two rooms is handy for having darkness is one, however makes the lab work more annoying. Having labs far away in the building is to avoid.
- Having the pumps in a separate room can be nice but it is often not necessary if sound isolation is done.
- A tap water switch for emergency supply of cooling water is a good practice. Also, having a cooling fan as emergency backup is good.
- Temperature and humidity sensors on the optical table are good for logging and checking the lab status.
- Voltage drops can damage equipment, a power surge protector can be very useful in the labs.
- Having on a proper rack a self maintained local LAN is very handy.
- Investing in extremely good lab PC is a good practice. Laptops should be avoided (especially with touch screens).

- Automatic checks of the logs file is important to get the status of equipment, both while running and for long term checks.
- Wide optical tables should be avoided to have a easier reach of the middle part.
- Clouds build with frame around the optical table and with a double level are essential.
- Dilution fridges have to be mounted with sound isolation from day zero.
- LAN ports and power supply should be in generous amount all over the lab. The more, the merrier.
- Having designed a proper space on the wall for tools and cable is handy.
- Reasonably cheap equipment (cables, USB converters, basic tools, ...) should be bought in large quantity.
- DACs should be preferred to arduinos and there should be plenty in the lab (and connected via LAN).
- Having instruments connected only via the local LAN and accessible to all computers is to be preferred to maximize flexibility.
- Guides for cables on the roof should not have holes, so that can be eventually moved easier.
- Having multiple stairs to reach the top of the cloud is handy.
- Using proper microscope and not home made ones is better.
- Motorized stages are always useful.
- Optical table with modular breadboard that can be used to make more levels are nice.
- Having design path (highway) for fibers in the optical table is good practice.
- Putting the fiber polarization controller and optical switches vertically is handy.
- Leaving empty spaces between blocks of the optical setup is handy for future expansions.
- Spending energy and time to have remote control over tools is always a good investment.
- In computers in the lab a common user is to be used for log in (in software, servers, ...).

CURRICULUM VITÆ

Niccolò FIASCHI

25-07-1993 Born in Florence, Italy.

EDUCATION

2007–2011	High School	
	Castelnuovo Gymnasium, Florence	
2012–2015	B.Sc. in Physics	
	Universitá degli studi di Firenze	
	Thesis:	Electron Spin resonance in NV centres in diamond.
	Promotor:	dr. Nicole Fabbri
	Promotor:	Prof. dr. Saverio Massimo Cataliotti
2016–2018	M.Sc. in Physics	
	Universitá degli studi di Firenze and Technische Universiteit Eindhoven	
	Thesis:	Optomechanical double-membrane photonic crystal sensor on a fiber tip.
	Promotor:	Prof. dr. Andrea Fiore
	Promotor:	Prof. dr. Massimo Gurioli
2019–2022	PhD. Physics	
	Delft University of Technology, the Netherlands	
	Thesis:	
	Promotor:	Prof. dr. Simon Gröblacher
	Promotor:	Prof. dr. Ewold Verhagen

LIST OF PUBLICATIONS

5. Amirparsa Zivari*, **Niccolò Fiaschi***, Roel Burgwal, Ewold Verhagen, Robert Stockill, and Simon Gröblacher, *On-chip distribution of quantum information using traveling phonons*, Science Advances Vol 8, Issue 46 (2022).
4. Amirparsa Zivari, Robert Stockill, **Niccolò Fiaschi** and Simon Gröblacher, *Non-classical mechanical states guided in a phononic waveguide*, Nat. Phys. 18, 789–793 (2022).
3. **Niccolò Fiaschi***, Bas Hensen*, Andreas Wallucks, Rodrigo Benevides, Jie Li, Thiago P. Mayer Alegre and Simon Gröblacher, *Optomechanical quantum teleportation*, Nat. Photon. 15, 817–821 (2021).
2. Jie Li, Andreas Wallucks, Rodrigo Benevides, **Niccolo Fiaschi**, Bas Hensen, Thiago P. Mayer Alegre, and Simon Gröblacher, *Proposal for optomechanical quantum teleportation*, Phys. Rev. A 102, 032402 (2020).
1. Luca Picelli, Anne van Klinken, Gustav Lindgren, Kaylee D. Hakkel, Francesco Pagliano, **Niccoló Fiaschi**, Ivana Sersic - Vollenbroek, P.J. (René) van Veldhoven, Rob W. van der Heijden, Andrea Fiore, *Scalable wafer-to-fiber transfer method for lab-on-fiber sensing*, Appl. Phys. Lett. 117, 151101 (2020).

* Indicates equal contribution

ACKNOWLEDGEMENTS

What a blast!

I never wrote an acknowledgment. I always tried to show my gratitude to the people around me daily (I hope I always succeed). This time I felt that I wanted to put it on paper, for future reference. And also to make the thesis less thin.

While writing I realize the enormous amount of people that I met and that have shaped my life in these last years. Looking back at all the nice events and moments we shared made me feel ’saudade’ and lucky that they happened. Thank you all.

First I want to thank my supervisor **Simon**. Feels like ages ago when I came to visit the group. I remember that you told me that we would have done ’fun physics’. I was quite skeptical, but over these years I always felt grateful that you showed me that yes, physics can be very fun. I am extremely happy with our interactions. Even if we don’t always agree I always felt that you value my opinion, and I am grateful that you gave me a lot of freedom and that we explored and did research in our way.

I also want to thank my co-supervisor **Ewold**. I enjoyed the collaboration with your group and all the discussions we had over these years. I valued your inputs and your interesting and sharp questions.

Then, the GLab group!

I want to start with my cleanroom mentor **Igor**. I had so much fun learning from you about nanofabrication, wine in Serbia, how fruit is the best, anime, and your vision about research in quantum physics. I hope you appreciate that I’m still using your chair and I hope that you are happy in Australia (and with a more comfortable chair).

Then my first lab mentor, **Andreas**. Thank you so much for all the time you invested in me (and even more, for your patience). It was very nice and inspiring working side by side with you in the lab, doing bouldering sessions, and appreciating the beauty of Schwarzwald (and nature in general).

And my other lab mentor, **Bas**. Among all the nice things we shared in the full year we worked together, the one that I am most grateful for is that I shift from calling you ’mentor’ to ’friend’. You showed me consistently how an (extremely) good experimental physics should think and act, and you set a lot of the good practices that I still strive to maintain. You also made me feel welcome in your family, showing me how much of a loving father you are.

I am grateful to **Moritz** for the immense help and fun times inside and outside the cleanroom (despite your love for tight cleanroom suits). I was always impressed by your readiness to help when needed, your unlimited energy and happiness, and for how much you value aesthetically appealing solutions.

To **Rob** for always being sharp on physics and with quick and easy explanations. I valued a lot your input in the research direction of the group, for being the first one that welcomed me in the lab, and for your music passion and knowledge.

Claus for the nice dinners in your apartment and for showing me with easiness your feelings. **Matthijs** for all his stories and his incredible energy and passion, and to **Jinkgun** for showing how hard work, consistency, and being a one-man army can make some cool experiments work. **Fred** for always be ready to talk about climbing, **Ulderico** for his big heart, **Pieter** for showing me his art side and **Sezer** for the fun nights in Rdam. **Max** for being the first to believe that I could answer questions about physics, for sharing some nice dinners at home, lunch outside in the sun, knowledge about airplanes, and for teaching me how to shoot a proper 'Howdy Folks'. **Barbara** for the very nice months we worked together, in all the challenges you showed to be a hard-working scientist and a fun colleague.

Parsa-jan. We started this path almost together and I am happy that we shared most of it very closely. We spent as many hours in the lab as in dinners and drinks and in this, I learned how to appreciate your wonderful personality. You definitively have a big personal and scientific thank you from my side.

Nina, we started as housemates and then continued as drinking/singing friends. Very much loved it. I am very grateful that we are also cleanroom colleagues, and that you always show your passion for nanofabrication and Miley Cyrus karaoke (unfortunately, not so often at the same time). **Alex** for his massive patience, amazing memory, and dedication. I am grateful we spent a lot of time together designing experiments, thinking about physics, biking around the Netherlands, beating me at badminton, and eating lasagne (and dim sun, and much more). **Liu**, I am very happy for your meditation sessions in the cleanroom, and for your passion about nature, bird watching, moon discussions, Chinese culture and food. I am also grateful that you showed me how a person can have a theoretical background and become quickly a great experimental physicist. And for giving me the badminton racket. **Gaia** for always being ready to laugh and learn, **Xiong** for his inputs in the group meetings, **Yong** for showing the dangers of home-made haircuts and **Emanuele** for showing some impressive tennis skills and how a turtleneck sweater can fit in every occasion. **Jin** for his big smiles and positive energy, for his help and mentorship in the cleanroom, and for showing me how to shoot a triple king double ace with a poker face. **Jana** for being patient with me even when I am a messy mentor and for the hard work you are putting into the project. **Lorenzo** for being a work machine fueled by curiosity and strong will, I am grateful you joined the lab. I'm also happy for the nice moments spent climbing together, can't wait to have more.

I also want to thank **Matthew** for the nice chats and **Pim** for the incredible help in the cleanroom.

One person that I am really grateful I have in my life is **Rodrigo**. I am very glad we shared so many wonderful moments (dinners, beach days, pride marches, parties, ...) and had so many discussions (about life, mental health, being a physicist, Brazilian music, and food ...). While spending hours in the lab, in the cleanroom, in bars, at dinner tables, and on zoom, we developed a precious friendship. I saw you changing in these past years thanks to your admirable effort in becoming the best version of yourself. I hope I had a positive influence on that, and that I will keep doing it. PS please bring me to a beach in Brazil I need it.

I also want to share my gratitude towards **Alex**. You welcomed me into your life and very soon started treating me as an old friend. I always felt that, despite our differences, we immediately got comfortable with each other.

One of the reasons that made me start the Ph.D. was the atmosphere in the Applied Science building. I immediately felt at ease, thanks to the wonderful people working there (and despite the poor architecture of the structure). For these reasons, I want to thank all the people in the Quantum nanoscience department and QuTech.

In particular, I want to thank **Sonia** for her energetic aura and for bringing happiness in all the rooms she passes, **Abel** for being a wonderful office mate, for the discussions about skydiving and sports, aesthetics in graphs and plots, food and much more, **Sabrya** for the lunches in the department and **Christos** for the energy and good questions about nanofabrication. **Yashoda** for the nice time spent together. Last but not least, **Luigi**. Thanks for the (numerous) time we chatted with a beer in our hands, your unexpected burst in with a question, your bad pun and laugh on it, your passion for combat sports and for sharing some drums sessions.

Lukas for the impeccable style, **Rasa** for the expansiveness, wonderful laughs and for singing so loudly and proudly in your office (I think it was you that I could hear from my office), **Laetitia** for always showing me a picture of your cat, **Hester** for the nice vibes and **Robbie** for being a very nice lab neighbor.

I also want to thank **Gary** for the work and energy he puts into the department (also together with the **QN C&C**, whom I also thank) and for his pungent questions. **Jasper** for being a wonderful companion of the consortium always ready to help and discuss, **Jean-Paul** for your nice jokes and energy, **Byoung-moo** for sharing very calmly the office space, **Marios** for always being so curious about our work and for the excellent questions and **Ines** for the amazing time spent at conferences and for how sweet and gentle you are.

Toeno, **Yufan** for the nice lunches together, **Iacopo** (aka Lacopo or Yacopo) for one of the best graduation party ever, **Annik** for the nice talks about climbing, **Michael** and our discussions about relationships and plants and **Brecht** for filling always the room with happiness.

Maria and **Karin** and all the administrative staff for the amazing support over these past years.

A special thank goes to **Ronald**. I arrived at your door countless times (generally in a rush) with some extremely badly done sketches and you always gave me back magnificent objects in an extremely short time.

I am also very grateful to have met **Richard** along the hallways and in conferences, and **Andrea** with his kind heart and very nice discussions about life and relationships.

I am also super grateful that I had the opportunity to bond with some amazing people from QuTech. **Tim** for the nice time spent at conferences, **Matvey**, **Martijn** and **Christos** for the wonderful support and help in the cleanroom, **Raymond** for always helping and being patient even when I prove that I have the knowledge of a zucchini in electronics and **Olaf** for helping to design experimental setups.

Hans for his acute observations, **Luka** for the bouldering sessions, **Julia** for the fun in the cleanroom and for the concerts, **Pablo** for the Katan games, **Nicolas** for the energy and for making Veldhoven a lot less horrible, **Davide** for meeting me always in the changing room of the cleanroom every time. And also **Vicky** for the nice moments spent together, **Julius** and **Colin** for teaching me the modern German pop music that allows me to stay 'abbronzato', **Sjoerd** for the big smiles and the discussion about being a goalkeeper, **Nandini** for the nice time spent together, **Matteo** for the Italian passion, discussion about music and life, **Stephan** for the dinners at your place, **Oriol** for the nights out, **Lukas** for the cleanroom times (hardcore resetting ebeam) and discussing bike trips, **Arian** for the immense party energy and strong opinions, **Hanifa** for the bike trips around the Netherlands, **Florian** for the climbing sessions, **Niv** for her wonderful effort in the Delft community and **Elvis** for the nice time discussing cleanroom procedure and climbing (and how probably doing them together is not a good idea). And also **Laurens**, **Kian**, **Scarlett**, **Mariagrazia**, **Christina**, **Margriet** and **Brennan**.

An enormous thank goes to all the cleanroom staff, with your wonderful work you allow us to pursue our (quite crazy sometimes) device fabrication. In particular **Bas** for your unwavering spirit and happiness (and singing), **Charles** for all the jokes and support, **Ewan** for making the cleanroom a much less sad place, **Roald** for your dedication and passion, **Eugene** for keeping the wet bench area operational despite all odds and **Marc** for managing all forces (staff, TNO, university, ...) extremely smoothly.

I want to thank also my ex-colleagues and friends of Eindhoven, **Andrea** for supervising the project and creating a wonderful group, **Maurangelo** for the help and support, **Claudiu** for the kindness and **Daniele** for the moral and psychological help. Last but not least, **Edoardo** who made my stay in that city much better and tried to teach me how to play Fortnite and make a better risotto.

Another big thanks go to the people I met in Dresden. **Viktor** for supervising the project while giving me enough flexibility to sleep until mid-day after being out with my housemate **Ada** (whom I thank for her energy and spirit and for making my stay in Dresden full of happiness). **Sundary** for the nice moments spent together and the affection that you gave me.

I want also to show my gratitude to all the wonderful people of Delft Bleau. In particular to **Yavuz** for being such a warm person with a giant heart, a great climber, cook, father of Varis, raver, and DJ, to **Hannah** for being one of the most tenacious and determined person I ever met, and still be a soft hugger, to **Thomas** whose cooking skills are beaten only by his kindness and by his being thoughtful, **Sara** for never be scared of a big jump and for convincing me to poo in the forest, **Elise** for her candor and openness, **Satya** for his house party and his tall betas and **Eva** for the nice moments spent together and your adorable cuteness.

I definitely owe a lot to Prof. **Parigi**, thanks to your teaching abilities you started my passion for physics. I also want to thank prof. **Massimo** that gave me the possibility of going to Dresden and Eindhoven, for his great lessons at uni and his kindness over the years.

Over my years at the University of Florence, I met a considerable amount of people. I would like to thank all of you, especially the members of the **Studenti di Sinistra** collective and all the people who called the **polo di Sesto** home for a few years. In particular **Enny** for the nice moments spent together and for creating the environment that allowed me to become a better person, **Sara** and **Fungi** for being just two adorable sweet potatoes. Also **Selmi** for the nice parties for Xmas and for being very 7, **Viola** for learning how to chew at 22 years old, for the lunches at grandma and the climbing, **Gnani** for the pane a maiale and for keeping the teenager spirit alive in me, **Tof** for the wonderful moment in the olive fields together, the nights out, the immense energy and will to laugh, **Lugo** for the horrible jokes, time skiing and climbing together, and for showing how a little competition in everything is possible, **Ale** for the dinners at your place and bike ride to the uni, **Ire** for dinner with the best stone falafel ever, rides in the panda and games. And also, **Andreucci**, **Bene**, **Tommi**, **Virgi**, **Rudy** and **Andrea**.

To all **Smaug** for the incredible psychological support over the years and the hundreds of messages per day (and for the cacciucco in Livorno and much more). **Pula** for his determination and patience and for being one of the sweetest person I have ever met, **Save** for being very close and supporting in some moments during the years and for showing how much you can achieve with a good mind and a lot of work, **Wuka** for being able to share with you everything (from deep feelings to entire watermelons), **Virgi** for the nice time spent together, for your directness, for your readiness to discuss and for keeping everyone grounded and sharp, **Mailo** for showing that you can always go through everything and still have the will to try more, **Binda** for the music together, the nights out and for always saying what you think, **Poldo** for showing that you can follow the path that you want any time and **Simo** for your enthusiasm and will to explore.

I want to especially showing my gratitude to **Tecla** for all the amazing time we spent in Florence. Between nights out and crying over textbooks you understood me as few people did, and it felt not only comforting but also necessary (and still does).

One (almost) last thanks goes to the high school friends, classmates, collective companions, and editors of the DeGeneratione, without which my adolescent years would have been much worse. In particular, **Cosimo** for being an unstoppable force of nature, **Pippo** ..., **Matte** for the games at worms, **Claudio** for the numerous discussions about life, and **Pezza** for the nice afternoons at your place and travels (and because you like 'pallone').

Lastly, I want to show my gratitude to my partner and my family.

Cami, since we started our relationship, there is no day passing that I am not thinking about how lucky I feel on having you in my life. I am very grateful that we are always able to shape our relationship to be in the happier place possible, and I am so happy for the affection and support we gave to each other. I love our direct communication, all the nice times we spend together, your bubbling energy and enthusiasm, the fun and laugh together and your careful thinking on a lot of stuff. And I hope you will continue to share all of this and much more with me for a long time.

I can't express how grateful I am to my family for all the love they gave me over the years. It was hard deciding to spend numerous years abroad, far from all of you, and you always support my decisions unconditionally. I remembered when I called to say that I was staying and I heard my father say 'Franci, non torna', with a lot of mixed feelings in the voice. I still miss you all continuously. **Mamus** and **Babbone** you create a united and loving family, and I am very thankful for that. Through a lot of work during all the amazing times at home and the vacations together, you made our connections strong. **Beba**, **Cocco** and **Cate** you are the best siblings I could hope for. Nonna **Anna**, thanks for always being close to us and for all the effort you put in unite the family.

Love you all very much.